Title	Shape Optimization of Adhesive Layer and Plastic Formability of Multi-materials Bonded by Adhesives
Author(s)	薛, 陽
Citation	大阪大学, 2024, 博士論文
Version Type	VoR
URL	https://doi.org/10.18910/96422
rights	
Note	

Doctoral Dissertation

Shape Optimization of Adhesive Layer and Plastic Formability of Multi-materials Bonded by Adhesives

Yang Xue

January 2024

Graduate School of Engineering
Osaka University

博士学位論文

接着接合されたマルチマテリアルの接合面形状最適化と塑性加工性

薛　陽

2024 年 1 月

大阪大学大学院工学研究科

Abstract

To address the pressing need for reducing CO2 emissions and energy consumption, the weight reduction of transportation equipment has become a pivotal objective. This necessitates the adoption of multi-material structures, with bonding dissimilar materials emerging as a crucial aspect of this endeavor. Adhesion, as a versatile method for joining various dissimilar materials, holds promise for constructing multi-material structures. Moreover, there is a noticeable trend towards the substantial utilization of metal laminates in body construction. This not only facilitates diverse designs for automobile frames but also opens the door to significant weight reduction through the incorporation of bonded metal laminates made of multiple materials.

In the initial phase of this study, a co-design process was delved, optimizing the shapes of adhesive-bonded structures based on a failure criterion derived from experiments using pipe specimens with inclining surface realizing multi-axial stress states by only uniaxial stress states that considered both material and structural factors. The optimized shapes achieved a significant reduction in applied stress levels, emphasizing a notable enhancement in the mechanical integrity of the adhesive layer. The initial shape of adhesive layer was proved as a valuable indicator, shedding light on the suitability of the initial model for multi-material design endeavors.

In the latter segment of this study, a pioneering approach involving multi-layered laminates bonded by adhesive, coupled with specialized conical cup testing experiments and FEM simulation, was implemented encompassing unitary and single/multi-layered configurations of different materials. The comparative analysis as well as the further analysis of the stress states in adhesive layer provided robust evidence of the adhesive's impact in amplifying the formability of bonded laminates offering promise for weight reduction across diverse applications without compromising structural integrity.

Content

1. Introduction

1.1. Research background

In recent years, the imperative of reducing CO_2 emissions has evolved into an increasingly prominent international concern. This shift is exemplified by the momentous adoption of the Paris Agreement during the 2015 Conference of Parties (COP) 21, aimed at addressing global warming on a global scale [1]. An illustration of the prevailing challenge is gleaned from the International Energy Agency's (IEA) analysis of CO_2 emissions in 2022. It reveals a disconcerting growth of 0.9%, equivalent to 321 million tons, in global energy-related CO_2 emissions, reaching an unprecedented pinnacle of over 36.8 gigatons (see Fig. 1.1) [2]. This escalation is in stark contrast to the objectives outlined in the Paris Agreement.

Against this backdrop, Japan has committed itself to a substantial target, pledging to reduce greenhouse gas emissions by 26% relative to 2013 levels by 2030, as stipulated in the Paris Agreement. Of particular relevance, the Ministry of Land, Infrastructure, Transport, and Tourism has reported that Japan's total CO_2 emissions for Fiscal Year 2021 amounted to 1.064 billion tons. A notable proportion, specifically 185 million tons, or 17.4%, is attributed to the transportation sector, encompassing various modes of conveyance such as automobiles and ships [3]. Delving further into the context, the automotive segment stands out as a major contributor, accounting for a substantial 86.8% of emissions within the transportation sector. This translates to a noteworthy 15.1% of Japan's overall CO_2 emissions, as illustrated in Fig. 1.2.

This intensified focus on emissions reduction stems from the progressively stringent regulations governing CO_2 emissions from automobiles worldwide [4]. Consequently, automobile manufacturers find themselves obliged to navigate these evolving regulations, necessitating the development and design of vehicles with significantly reduced CO_2 emissions.

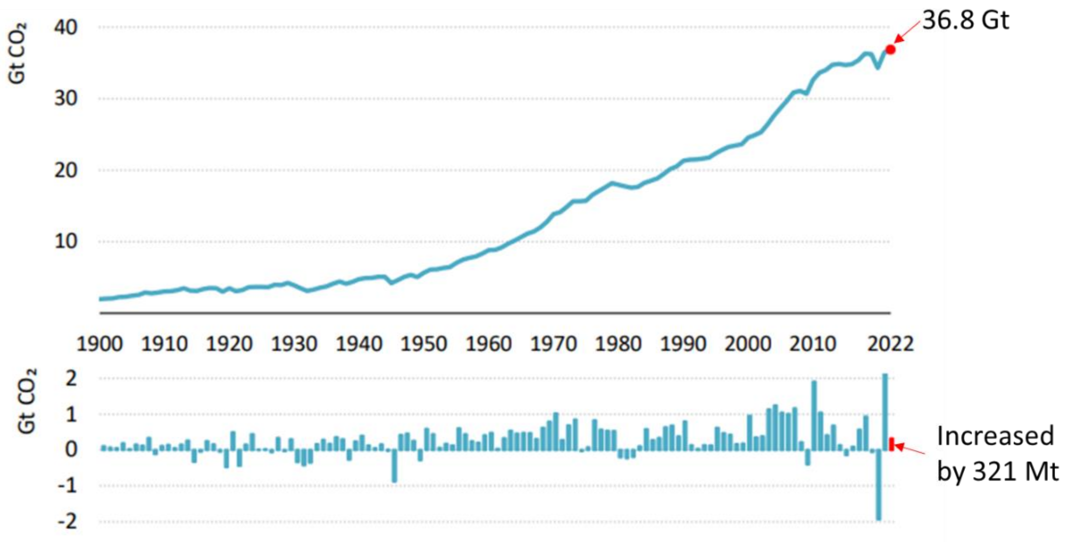

Fig. 1.1 Global CO2 emissions from energy combustion and industrial processes and their annual change, 1900-2022. [2]

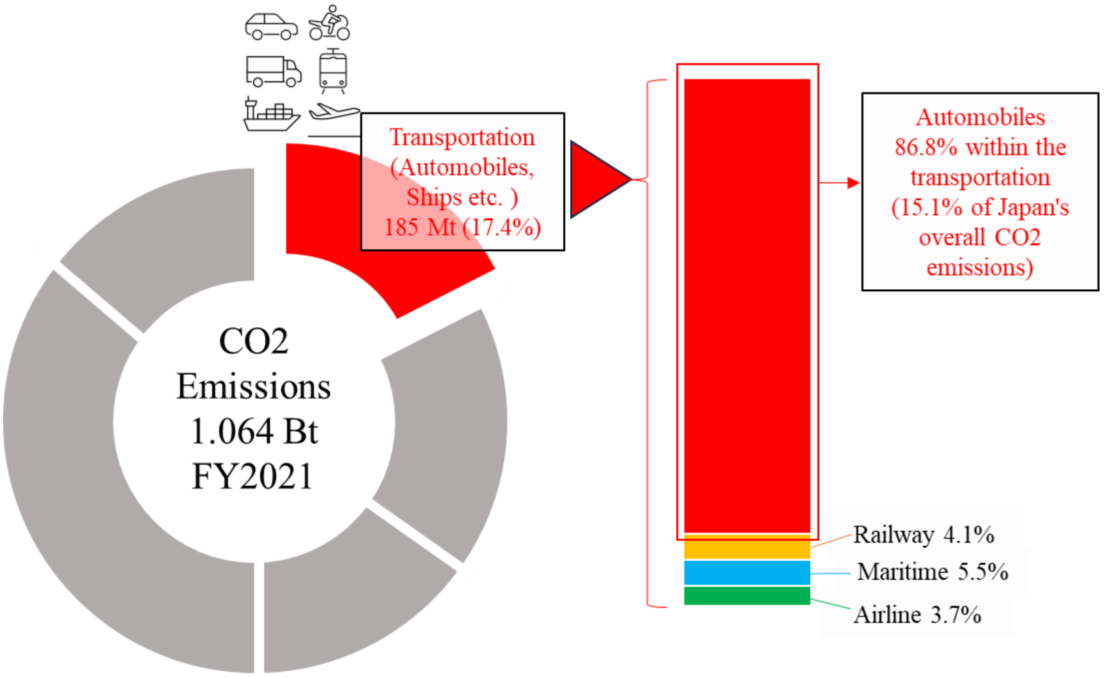

Fig. 1.2 The portion of CO2 emission from automotive in Japan. [3]

1.1.1. Multi-material design

As elucidated in "Fuel Economy and CO_2 Emissions of Passenger Cars" [5], a comprehensive publication from the Ministry of Land, Infrastructure, Transport, and Tourism, it is evident that an automobile's weight exerts a direct influence on both its CO_2 emissions and fuel efficiency. The fundamental principle underlying this relationship posits that the reduction of an automobile's weight contributes to a concurrent decrease in CO_2 emissions and an enhancement in fuel economy. As a result, one strategic avenue for achieving weight reduction in automotive structures involves the adoption of a multi-material design approach. This innovative paradigm involves the judicious combination of diverse materials, each possessing specific attributes of strength and stiffness, and has been the focal point of extensive research efforts [6]-[9].

Multi-material structures, marked by their amalgamation of materials boasting diverse attributes, necessitate the adept technique of joining dissimilar materials. The realm of research has explored various methods aimed at facilitating the fusion of these dissimilar materials [10] [11]. As depicted in Fig. 1.3, these methods can be broadly classified into three overarching categories: welding, chemical bonding, and mechanical fastening [10], [12].

The realm of welding techniques spans a diverse array of methods, each tailored to specific applications and materials. These methods include laser welding [13]-[16], resistance spot welding (RSW) [17], [18], friction stir spot welding (FSSW) [19]-[22], friction stir welding (FSW) [23], [24], friction element welding (FEW), Friction Stir Welding (FSSW) [23], [24], Friction Element Welding (FEW) [25], and Resistance Element Welding (REW) [26], as well as Laser Brazing [27],[28], among others. Notably, friction stir welding (FSSW, FSW) has found prominence in the welding of steel and aluminum materials [29]. However, it is essential to recognize that welding processes are not without their drawbacks. Traditional welding procedures have the potential to compromise the material's strength, both at the micro and macro levels, thereby impacting structural integrity [30]. Furthermore, manual welding techniques, particularly in small-scale industries, often yield suboptimal surface finishes and a diminished quality in the welded components [31]. An additional limitation of conventional welding practices is their restriction to materials with similar properties, rendering them unsuitable for applications requiring the joining of dissimilar materials. This constraint impedes their feasibility in the context of multi-material design, a crucial consideration in contemporary engineering and manufacturing.

The domain of mechanical fastening encompasses a wide spectrum of methodologies, each meticulously tailored to meet the demands of specific applications and materials. These methodologies include Self-Pierce Riveting (SPR) [32],[33], traditional bolting [34], mechanical clinching [35],[36], Flow Drill Screws (FDS) [37], Impulse Accelerated Tacking (ImpAcT) [38], blind rivets [39], [40], and hemming techniques [41], among others. Self-Pierce Riveting (SPR) finds its forte in fastening steel and aluminum materials, while blind rivets are particularly well-suited for joining composite materials and metals [29]. Nevertheless, it is imperative to recognize a salient drawback associated with mechanical fastening methodologies. The act of drilling holes for bolts or rivets, an inherent necessity in mechanical fastening, has the potential to yield stress concentrations and inflict damage upon composite materials. This concern is compounded by the fact that drilling these holes may inadvertently sever fibers or other reinforcement elements, thereby creating pronounced stress concentrations at each discrete fastener location [42]. Additionally, the introduction of such fasteners results in an incremental increase in the overall weight of the structures. This counteracts the overarching objective of weight reduction, which stands as a pivotal consideration in contemporary engineering and design paradigms.

The domain of chemical joining encompasses various methodologies, including adhesion [42]-[46], gas adsorption joining (GAJ) [47], and surface-activated joining [48]. Additionally, it encompasses hybrid techniques like weld bonding [49], which combines elements of both welding and bonding, and the fusion of Self-Pierce Riveting (SPR) with adhesive bonding [50]. Within this spectrum, adhesive bonding stands out due to its array of merits. Notably, it exhibits the following advantages:

(a) Versatility in material compatibility: Adhesive bonding is adaptable to a wide range of dissimilar materials.

(b) Galvanic corrosion prevention: It effectively mitigates the risk of galvanic corrosion.

(c) Inherent lightweight nature: Adhesives themselves are lightweight, contributing to overall structural weight reduction.

(d) Enhanced surface-to-surface bonding: It facilitates surface-to-surface bonding, resulting in joints with superior strength when compared to point bonding achieved through welding or mechanical fastening.

These attributes position adhesive bonding as a highly promising technique within the realm of multi-material structure joining [51].

1.1.2. Epoxy and acrylic adhesives

There are many kinds of adhesives while two major groups are most widely used in many industries; epoxy and acrylic adhesives. The former is a typical and major one of structural adhesive, which can provide a high-performance for bonding large areas of sheet materials and produce a better finished appearance than the other joint methods such as welding or screws [52]. Epoxy adhesives are widely used in various industries especially for large size products such as wind energy blade structures [53], aviation fuel resistant joints, and bonding parts of wind turbine blades, marine vessels, or civil engineering structures [54] where higher strength is required and epoxy adhesives are also extensively used in structural bonding, particularly in aerospace, electronics, and medical devices, due to their versatility and ability to meet specific mechanical and environmental requirements [55]. While Acrylic adhesive used in the construction sector is an adhesive bond that comprises a denatured acrylic-based structural adhesive of 2-component type and is commonly used in the production of flexible laminates [55]. As the molecular structures of these two adhesives are different, so too are their physical and mechanical properties [56], [57].

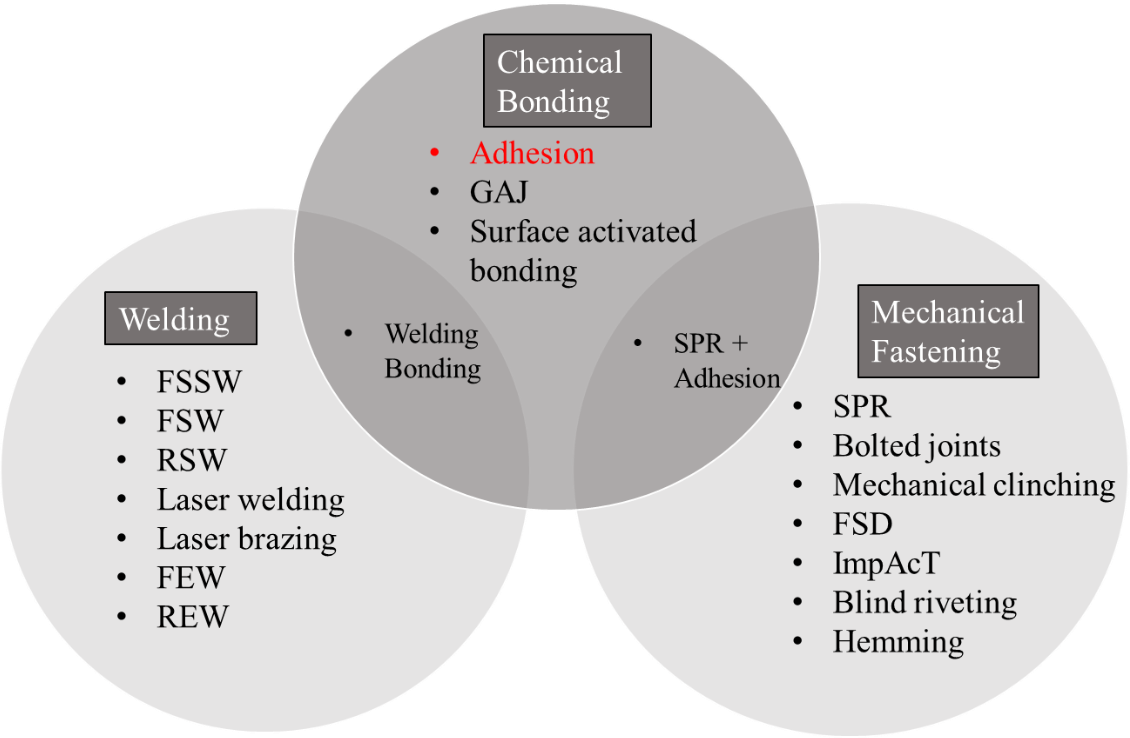

Fig. 1.3 Three distinct categories encompass the gamut of methodologies employed for joining dissimilar materials: welding, chemical bonding, and mechanical fastening.

1.2. Failure Criterion and shape optimization of different adhesives

1.2.1. Strength evaluation of adhesive joints

In the design of multi-material structures utilizing adhesion, a crucial initial step entails the development of a methodology for assessing the strength of adhesive joints. Traditional approaches for evaluating adhesive strength have relied on tensile shear tests [58]-[61] (Fig. 1.4(a)) and debonding tests [62]-[64] (Fig. 1.4(b)) of overlapped joints. These methods have conventionally served to gauge the robustness of adhesion. However, they come with inherent limitations, as highlighted below. In Fig. 1.5, we can observe the average critical shear stress τ_c obtained from tensile shear tests conducted on representative market adhesives, alongside the critical load F_c per unit length of the adhesive layer derived from peel tests. This approach yields a relative evaluation marked by considerable variation, making it challenging to directly incorporate the limit load F_c garnered from debonding tests into the design process.

Tensile shear tests on overlapped joints engender not only shear forces but also bending moments at the adhesive joints. Therefore, for a more precise determination of the tensile shear strength of adhesives, innovative methods have been introduced. This includes tensile shear tests [65] and the Thick Adherend Shear Test (TAST) [66], specifically devised for double-overlap joints. Moreover, an array of peel test methodologies has been developed, encompassing the 90° peel test [67], the 180° peel test [68][69], and the T-shaped peel test [69][70]. These advancements offer a comprehensive toolkit for evaluating adhesive joint performance in a variety of scenarios, ensuring a more robust and accurate assessment of adhesion strength in multi-material structures. Nevertheless, it's important to note that these test methods are primarily designed to assess adhesive bond strength under specific loading conditions. While they offer a convenient benchmark for selecting adhesives and making strength comparisons, they may not directly translate to evaluating the adhesive joint strength within the multiaxial stress field experienced in real-world equipment applications.

Hence, the design of multi-material structures necessitates the establishment of a methodology to assess adhesive strength within the context of a multiaxial stress field. Currently, there exist strength evaluation methods grounded in the stress components within the adhesive layer. These methods encompass the Quadratic stress criterion [71], which leverages vertical and shear stresses at the interface, the Tsai-Wu rule [72], the utilization of Mises' condition involving stress invariants, and Drucker-Prager's condition [73]. Additionally, there's the evaluation method reliant on a failure criterion [74] that incorporates these criteria. However, these strength evaluation criteria involve material-specific parameters closely linked to the adhesive in use. The identification of these parameters necessitates experimental determination before the evaluation function can be effectively employed for strength prediction.

To assess material properties, it is reasonable to identify the material parameters of the strength evaluation criterion using a test method that does not cause stress concentration in the adhesive. An alternative approach involves the utilization of a napkin-ring specimen [75]-[78] along with a modified tensile/torque test method employing a napkin-ring specimen to mitigate stress concentration effects [74],[79]-[81]. However, this technique necessitates a precise biaxial testing apparatus, which is available only in a limited number of research institutions. An adapted Arcan test methodology has been devised to probe the strength of bonded assemblies subjected to multiaxial stress states [82]-[84]. Therefore, a simplified evaluation approach permits the application of varied multiaxial ratios of tensile and shear stresses solely through only uniaxial tensile testing on bonded pipe specimens and the parameters for the acrylic adhesive have been experimentally determined using pipe specimens which can tune the ratio of applied mean stress and shear stress to realize multiaxial stress state in the previous research [85]. While parameters for other kinds of adhesives have been established, there remains an unaddressed gap in understanding how variations in these parameters impact the failure criterion.

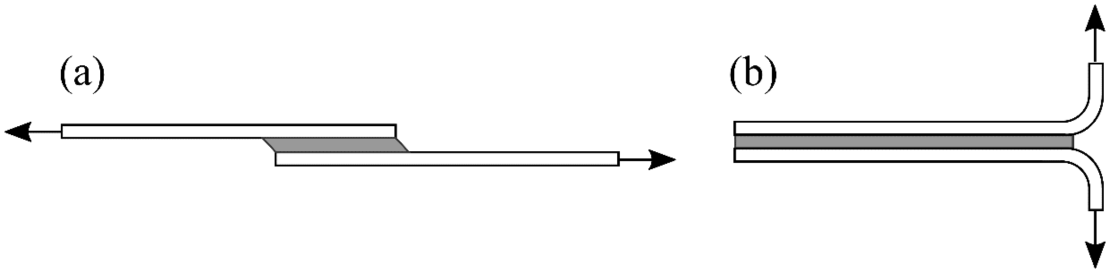

Fig. 1.4 Test methods of adhesive strength: (a) Single lap shear test, (b) T-peel test.

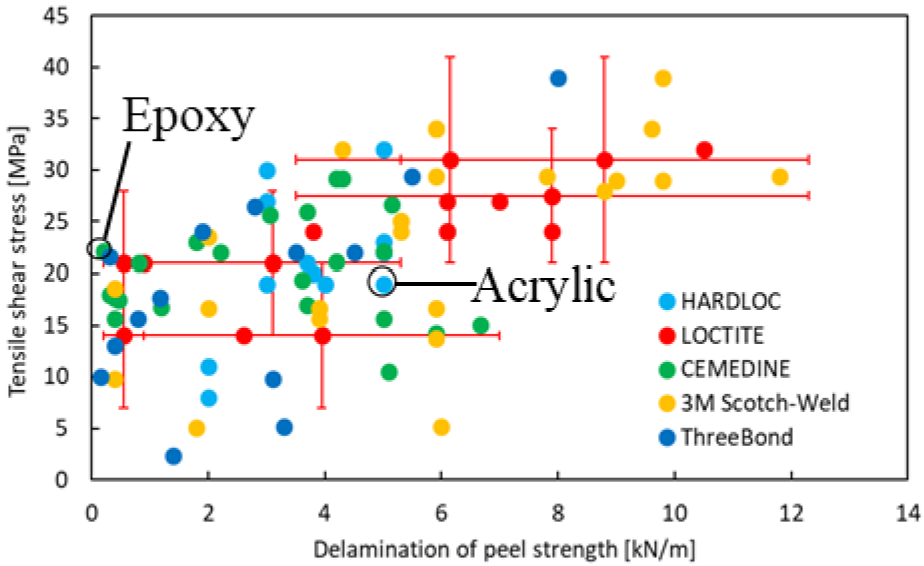

Fig. 1.5 Tensile shear strength and peel strength of commercial adhesives.

1.2.2. Shape optimization based on the failure criterion

As elaborated in Sec. 1.2.1, the evaluation of adhesive joint strength can be conducted through failure criteria, with material parameters identified via simplified assessments using pipe specimens. However, the strength of adhesive structures is not solely contingent upon material properties; it is significantly influenced by various other factors, including adhesive thickness and the properties of the parent materials to which the adhesive adheres. These intricate and interdependent variables underscore the need for a comprehensive assessment of the mechanical integrity of bonded structures.

Structural optimization, a powerful technique for designing structures, relies on a specified evaluation function. This methodology falls into two primary categories: dimensional optimization [86], which is a parametric optimization approach, and nonparametric optimization methods, including shape optimization [87], [88] and topology optimization [89]. In parametric optimization, the number of design variables determines the degrees of freedom for shape modifications. In contrast, nonparametric optimization is executed in a functional space, where the shape is represented by a region

Ω, facilitating a nearly infinite range of degrees of freedom due to the absence of discretization. Consequently, nonparametric optimization methods provide greater flexibility in altering the initial structure shape and enhancing structural strength compared to parametric optimization. In a prior study, an optimization method was proposed for the adhesive interface, seeking to enhance the strength of bonded structures based on the established failure criteria [90]. However, this previous work focused solely on shape optimizations of acrylic adhesive layers, and the disparities in optimization outcomes have yet to be explored.

Hence, the present research extends the prior findings by applying and refining the failure criteria and optimization techniques to assess the strength of adhesive structures bonded with epoxy adhesives. The outcomes are compared with those obtained using acrylic adhesives to scrutinize distinctions in failure behaviors within multiaxial stress states and to assess the influence of adhesive layer shapes on structural strength enhancement.

1.3. Bonded metal laminates and proper formability test method

1.3.1. Plastic formability of metal laminates bonded by adhesives

Multi-material design is generally applied to the frame of structures where the strength of the bonded parts is crucial. In the automotive sector, a substantial utilization of metal laminates in body construction is evident [91]-[93]. This practice not only facilitates diverse designs of automobile frames but also introduces the potential for significant weight reduction through the incorporation of metal laminates. To ascertain the viability of implementing multi-layered configurations and to facilitate their integration into industrial production processes, a comprehensive evaluation of the plastic formability of bonded multi-layered metal sheets is imperative. This evaluation necessitates a comparative analysis with unitary sheet, thereby contributing to a judicious assessment of the feasibility of adopting the adhered sheet within a multi-layered paradigm.

The assessments discussed in Sec. 1.2.1 have predominantly focused on the failure criterion of adhesive's material. However, for an exhaustive evaluation of adhesive laminates, it becomes imperative to consider their plastic formability. Several testing and simulation have also been introduced to exam the deformation characteristics of the adhesive bonded metal sheet and the multi-material specimens by V-bending testing [94],[95]. Nevertheless, previous research primarily concentrated on bending deformation for evaluation of delamination strength, not mainly focusing on the practical deformation such as shrinkage and elongation which are crucial in real manufacturing process. Consequently, the integrated formability of adhesively bonded sheets under a variety of deformations remains unexplored. Additionally, the application of adhesive bonding introduces complexity, with the overall structural strength being influenced not only by adhesive properties but also by the combined structural factors and the plastic formability will also be influenced by structural factors such as thickness of adhered materials and the adhesive layer [96]. Consequently, a testing methodology capable of gauging the integrated plastic formability of multi-layered metal sheets has to encompass both material and structural factors.

1.3.2. Proper test method to evaluate plastic formability.

The primary objective of the plastic formability test lies in the estimation and comparison of forming force and forming limits. Given that even the slightest distinctions in forming limits hold significant implications for operational efficacy, a meticulous comparison of material forming limits becomes imperative. Commonly employed formability tests predominantly serve the purpose of estimating or comparing these forming limits. Furthermore, in press forming, materials are classified based on the interplay between primary deformation and the controlling factors governing forming limits. This classification gives rise to distinct categories of press forming, deep drawing, stretching, elongation flange, and bending. As a result, direct formability assessments must be conducted considering combinations of deformations, as illustrated in Table 1.1

[97]. However, it's noteworthy that, beyond the discrete categories of deep drawing, stretching, elongation flange, and bending, practical applications often involve intricate combinations of these forming methods. Particularly, bending deformation stands as a fundamental element intrinsic to all press forming processes. In order to conduct a precise assessment of laminate formability, it becomes essential to select a testing methodology that aptly captures the complexities of plastic formability.

Several existing testing methods have been developed to assess fundamental forming behaviors and formability characteristics [98]. Noteworthy among these are the Erichsen Deep Drawing Cup Test [99], Sweden Deep Drawing Test [100], and Swift Cup-forming Test [101], all tailored to gauge deep drawing capabilities. Additionally, the Erichsen Cupping Test [99], Olsen Cup Test [102], and Erichsen Bore Expanding Test [103] have been formulated to measure stretchability and elongation flange performance, respectively. Nevertheless, these testing methodologies are not devoid of specific challenges that necessitate resolution. For instance, the Erichsen Deep Drawing Cup Test faces practicality concerns related to determining the increment in plate diameter for establishing deep drawing limits and the number of plates of identical diameter to be concurrently drawn to ascertain these limits. Furthermore, these existing testing techniques primarily focus on evaluating individual basic formability aspects, often overlooking the complexities inherent in plastic formability evaluation.

In light of these limitations, the Conical cup testing method, introduced by Fukui [104], has garnered attention. This approach constitutes a direct and plastic formability testing method that employs a tapered die to provoke shrinkage flange deformation, elongation flange deformation, and punch bottom rupture. Unlike its predecessors, the Conical cup testing method holds promise in providing a more comprehensive evaluation of material behavior by considering an amalgamation of deformation modes. This methodology has been selected to assess the forming force and forming limits of metal laminates in this research.

Table 1.1 Complex plastic formability of the press deformation and deformation limit factors.

Deformation Limit factors	Shrinkage flange	Elongation flange	Bending
α rupture (Lack of strength)	Deep drawability	Stretchability	-
β rupture (Lack of elongation)	-	Elongation frangibility	-
Bending rupture	-	-	Bendability

1.4. Purpose of the research

The primary objective of this research is twofold. Firstly, it aims to assess the strength of adhesive structures in a multi-material context under multiaxial stress conditions, considering various adhesives with diverse strength properties. Additionally, it endeavors to enhance the plastic formability of multi-layer metal laminates bonded by adhesives, with the overarching goal of bolstering the strength and expanding the utility of adhesives within the domain of multi-material design in real-world industrial applications.

In the initial phase of this study, the focus lies in discerning distinctions in failure criteria under multiaxial stress states, thereby shedding light on the material attributes of the adhesives in use. Furthermore, an investigation is conducted to unravel the disparities in shape optimization for different adhesives employing the failure criteria. This endeavor explores the structural dimension of the adhesive's impact.

In the latter segment of this research, the primary aim is to conduct a comprehensive evaluation of the plastic formability of multi-layered metal structures, referencing unitary metal sheets as a benchmark. The goal is to gauge the influence of adhesives in this context, ascertain the viability of implementing multi-layered configurations, and pave the way for their seamless integration into industrial production processes.

1.5. Organization of this paper

This paper comprises six chapters. In Chapter 1, the imperative need for weight reduction in transportation equipment, with a specific emphasis on multi-material structures in automobiles, is elucidated. Adhesion is introduced as a vital joining technology for diverse materials, crucial in the design of multi-material structures. A comparative analysis of two adhesive materials, epoxy, and acrylic, is presented, encompassing their properties and applications. The co-design process of adhesive-bonded structures, inclusive of testing methods for adhesive strength evaluation and the methodology for shape optimization of bonded interfaces, is comprehensively reviewed. Additionally, the advantages of bonded metal laminates and the significance of evaluating the plastic formability of such laminates are discussed. The chapter delves into the limitations of conventional testing methods and outlines the requisites for establishing proper testing methodologies. Finally, the chapter elucidates the objectives and purposes of the study.

Chapter 2 introduces a method for evaluating the strength of adhesive materials under multi-axial stress states and applies it to establish the failure criterion of epoxy adhesives based on mean stress and octahedral shear stress. The results are meticulously discussed and compared with those of acrylic adhesives from ref. [85], considering failure behavior and thickness dependencies.

In Chapter 3, the derived failure criterion of epoxy adhesive is applied to shape optimization methods. The methodology, encompassing the theory of shape optimization and the construction of FEM models with boundary conditions, is presented. Results from the optimization process are compared with those of acrylic adhesive from reference [90], exploring the influence of material properties and initial conditions on the shape optimization of bonded structures.

Chapter 4 introduces the conical cup testing method for evaluating the plastic formability of bonded metal laminates, covering the design of the testing machine and the manufacturing process of specimens. Testing results for various specimen types are discussed based on load-displacement relations. Further exploration involves post-testing and on-testing specimens through the conical cup value (C.C.V.) and observation from the see-through aperture. A comprehensive comparison of different specimen types is conducted to verify the adhesive's effect in enhancing the formability of metal laminates.

In Chapter 5, FEM simulation of conical cup testing using bonded metal laminates is performed to unveil features unobservable in real testing. FEM models are constructed based on real testing parameters, including material properties obtained from tensile testing using specimens identical to those used in real conical cup testing. The results are discussed and compared with real testing outcomes. A specific focused discussion on the stress states of the adhesive layer concerning mean stress and octahedral shear stress is conducted to identify the adhesive's effects established from testing.

Chapter 6 serves as the concluding chapter, summarizing the results obtained in each preceding chapter and providing a comprehensive conclusion to the paper.

2. Evaluation of Adhesive Strength in Multiaxial Stress Fields

For the design of multi-material adhesive structures, it is necessary to consider designs that improve strength in the multiaxial stress field that occurs in the actual operation of the structures. For this purpose, it is essential to properly evaluate the adhesive strength in multiaxial stress fields. In previous research, the failure criterion based on the first invariant of stress tensor I_1 and the second invariant of deviatoric stress tensor J_2 was established and the parameters for the acrylic adhesive have been experimentally determined using pipe specimens which can tune the ratio of applied mean stress and shear stress to realize multiaxial stress state [85].

In this chapter, the failure criterion was reconstructed with mean stress $\sigma_m(=\frac{1}{3}I_1)$ and octahedral shear stress $\tau_{\mathrm{oct}}(=\sqrt{\frac{2}{3}J_2})$ instead of I_1 and J_2 for the practical usage because both scalar stress parameters are the representative values in the principal stress space (called Haigh-Westergard space). The parameters of the failure criterion for epoxy adhesives were determined using the same methods proposed in ref. [85] and the result was discussed and compared with that of acrylic adhesives. The thickness dependence of adhesive layer was then discussed and the failure criterion for adhesive layers with different thickness were also obtained.

2.1. Failure criterion of adhesives under multiaxial stress state

In the present section, two cylindrical coordinate systems are established with two kinds of loadings, uniaxial tension and torque, but only the former is applied for the experiments to get the failure function and the obtained criteria are extended to the shape optimization of adhesives under the two kinds of loadings, which will be discussed in Chapter 3.. The cylindrical coordinate system (r, θ, z) are transformed into (r', θ', z') in terms of the angle φ between the horizontal plane $r\theta$ and the inclined plane $r'\theta'$ parallel to the adhesive surface as shown in Fig. 2.1.

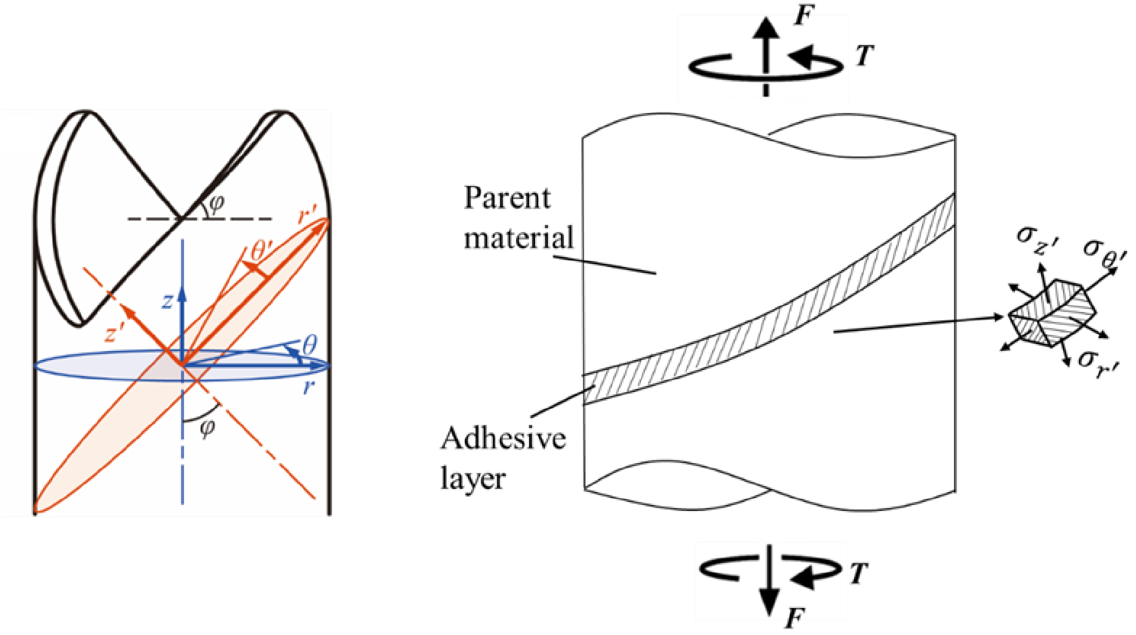

Fig. 2.1 Coordinate transformation of the cylindrical coordinate system from (r, θ, z) to (r', θ', z') in terms of angle φ.

Because the thickness of adhesive layer is small enough and the stiffness of adhesive is much smaller than that of the parent material, the deformation of adhesive is assumed to be strongly restricted by the more rigid parent material. Then, the normal strains acting in the radial and circumferential directions along the cutting surface can be assumed that:

$$\frac{\varepsilon_{r'}}{\varepsilon'_z} \approx 0, \tag{2.1}$$

$$\frac{\varepsilon_{\theta'}}{\varepsilon'_z} \approx 0. \tag{2.2}$$

This assumption has been certified using finite element simulations for Poisson's ratio with a range from 0.2 to 0.4. Constitutive equations are then derived from Eqs. (2.1) and (2.2):

$$\sigma_{r'} = \sigma_{\theta'} = \frac{E\nu}{(1+\nu)(1-2\nu)}\varepsilon_{z'}, \qquad \sigma_{z'} = \frac{E(1-\nu)}{(1+\nu)(1-2\nu)}\varepsilon_{z'}. \tag{2.3}$$

where $\sigma_{r'}$, $\sigma_{\theta'}$ and $\sigma_{z'}$ are the normal stresses in radial, circumferential and direction along the cutting surface, and E is Young's modulus and ν is Poisson's ratio. According to Eq. (2.3), $\sigma_{r'}$ and $\sigma_{\theta'}$ are expressed as a function of $\sigma_{z'}$.

$$\sigma_{r'} = \sigma_{\theta'} = \frac{\nu}{1-\nu}\sigma_{z'}. \tag{2.4}$$

The first invariant of stress tensor I_1 and the second invariant of deviatoric stress tensor J_2 can be calculated as:

$$I_1 = \sigma_{r'} + \sigma_{\theta'} + \sigma_{z'} = \frac{1+\nu}{1-\nu}\sigma_{z'}, \tag{2.5}$$

$$\begin{aligned} J_2 &= \frac{1}{2}\left\{\left(\sigma_{r'}^2 + \sigma_{\theta'}^2 + \sigma_{z'}^2 + 2\tau_{r'\theta'}^2 + 2\tau_{\theta'z'}^2 + 2\tau_{z'r'}^2\right) - \frac{1}{3}I_1^2\right\} \\ &= \frac{1}{3}\left(\frac{1-2\nu}{1-\nu}\right)^2 \sigma_{z'}^2 + \tau_{\theta'z'}^2. \end{aligned} \tag{2.6}$$

Here, in Eq. (2.6), $\tau_{r'\theta'}$ and $\tau_{z'r'}$ are assumed to be infinitesimally small compared with $\tau_{\theta'z'}$ and $\sigma_{z'}$.

According to the coordinate transformation in Fig. 2.1, the normal stress $\sigma_{z'}$ and shear stress $\tau_{\theta'z'}$ acting in the adhesive layer can be expressed by the tensor transformation as:

$$\sigma_{z'} = \frac{\sigma_z}{2} + \frac{\sigma_z}{2}\cos 2\varphi - \tau \sin 2\varphi\,, \tag{2.7}$$

$$\tau_{\theta' z'} = -\frac{\sigma_z}{2}\sin 2\varphi - \tau \cos 2\varphi\,. \tag{2.8}$$

For a uniaxial tensile test mentioned in the following section 2.2, only the tensile stress σ_z exists. Thus, according to Eqs. (2.7) and (2.8), $\sigma_{z'}$ and $\tau_{\theta' z'}$ can be calculated as:

$$\sigma_{z'} = \sigma_z \cos^2 \varphi\,, \tag{2.9}$$

$$\tau_{\theta' z'} = \sigma_z \sin\varphi \cos\varphi\,. \tag{2.10}$$

From Eqs. (2.5) and (2.6), I_1 and J_2 are reduced to be the following linear relation:

$$\sqrt{J_2} = \left\{\frac{1-\nu}{1+\nu}\sqrt{\frac{1}{3}\left(\frac{1-2\nu}{1-\nu}\right)^2 + \tan^2\varphi}\right\} I_1 = k(\varphi,\nu) I_1, \tag{2.11}$$

where $k(\varphi,\nu)$ is the coefficient which can be calculated from angle φ and Poisson's ratio ν. In the following results, mean stress $\sigma_m(=\frac{1}{3}I_1)$ and octahedral shear stress $\tau_{\mathrm{oct}}(=\sqrt{\frac{2}{3}J_2})$ are employed instead of I_1 and J_2 for the practical usage in the following sections.

The failure function proposed by Mahnken and Schlimmer [74] is

$$f = C_0 J_2 + \frac{1}{3}C_1 I_1 + \frac{1}{3}C_2 {I_1}^2 + C_3. \tag{2.12}$$

If the parameters are taken as $C_1 = 0$ and $C_2 \neq 0$, the obtained failure criterion is the same as the one proposed by Green [105] which can be considered as equivalent to the quadratic delamination criterion proposed by Brewer and Lagace [71]. If $C_1 = C_2 = 0$, the failure function is equivalent to the conventional von Mises failure criteria.

From Eqs. (2.5) and (2.6), it is clearly shown that the failure function can be estimated with three parameters of ν, φ and σ_z, which are determined by the results of tensile tests using the pipe specimens bonded by different adhesives. Poisson's ratios ν of the adhesives are taken into the present research as 0.35 for epoxy adhesive and 0.4 for acrylic adhesive, respectively. As the failure criterion differs only by the parameters, the numbers of 1/3 before the coefficients of C_1 and C_2 in Eq. (2.12) do not have any meaning. As a result, the failure criterion can be simplified as:

$$f = c_0 J_2 + c_1 I_1 + c_2 {I_1}^2 + c_3. \tag{2.13}$$

where $c_0 = C_0$, $c_1 = \frac{1}{3} C_1$, $c_2 = \frac{1}{3} C_2$ and $c_3 = C_3$.

2.2. Experiments using pipe specimens

2.2.1. Specimens using in the experiments

As depicted in Fig. 2.1, a cylindrical aluminium specimen was meticulously crafted using a laser cutting machine, 3D FABRI GEAR 220 II, boasting a rated output of 4 kW, manufactured by Yamazaki Mazak Corporation. The specimen's preparation was orchestrated to induce both vertical stress and shear stress within the adhesive layer, contingent upon the chosen inclination angle φ, all under the influence of uniaxial tension.

To delve deeper, Fig. 2.2(a) provides an insight into the specimen's formation through the use of a laser beam machine. These specimens were meticulously crafted at varying inclination angles (φ = 0°, 20°, 45°, and 75°). Figure 2.2(b) reveals the circumferential development of the cut surface, where the inclination angle exhibits two cycles, and the curvature bend (convexity) associated with the inclination possesses a radius of curvature measuring 2 units.

For the subsequent step in the experimentation, cylindrical specimens, each sharing the same inclination angle, were bonded together employing epoxy adhesive (EP-171, CEMEDINE Co., Ltd.), following a rigorous curing regimen at 120°C for a duration of 20 minutes.

In an effort to provide precise data, the thickness of the adhesive layer was meticulously measured at eight distinct points, duly indicated by the red circles in Fig. 2.2(b), employing microscopic imagery. Subsequently, the average adhesive layer thickness (h_0) was diligently computed for each individual specimen. The recorded measurements of adhesive layer thickness are cataloged in Tables 2.1 and 2.2. To ensure the accuracy of the calculated average thickness, measures were taken to exclude data points where adhesive removal by sandpaper was incomplete. This process involved computing the standard deviation (σ), and data points deviating more than 2σ from h_0 were eliminated. Subsequently, the average thickness of the adhesive layer (h) was recalculated using the refined dataset.

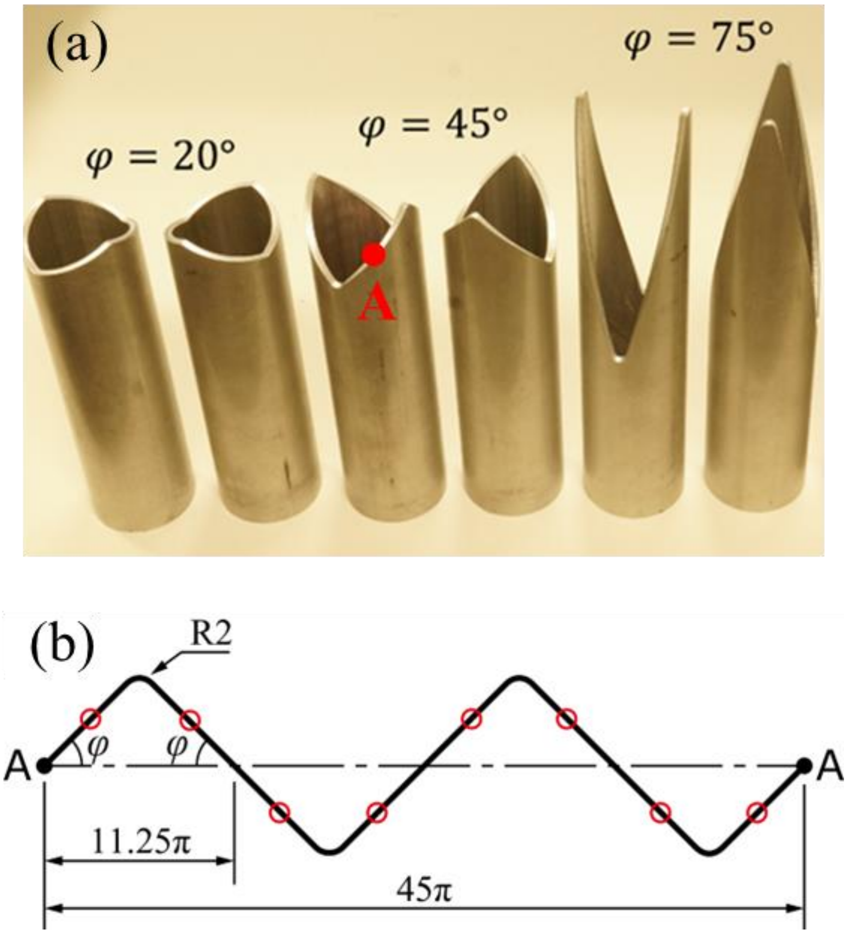

Fig. 2.2 (a) Example of a test specimen before adhesive bonding; the tilted cutting surface have inclination angles φ of 20°, 45° and 75°. (b) Development of the cutting surface. Red circles represent measurement points of the adhesive thickness.

Table 2.1 Thicknesses of the epoxy adhesive layers of (a) 0° and (b) 20° pipe specimens

(a)

0° pipe specimen No.		1	2	3	4	5
Thickness [µm]	1	368.1	523.7	133.8	240.4	524.0
	2	267.8	365.4	86.6	210.9	482.7
	3	305.3	208.6	129.9	732.2	506.6
	4	456.6	300.9	167.3	775.8	485.9
	5	240.0	297.2	250.0	486.1	364.2
	6	420.6	429.5	116.1	492.2	387.7
	7	254.9	250.0	69.1	537.4	456.8
	8	359.2	283.4	165.4	559.5	435.0
Mean value h_0 [µm]		334	332	140	504	455
Standard deviation σ [µm]		79.8	102.7	56.2	202.1	56.5
Mean thickness h [µm] ($h_0 - 2\sigma$ to $h_0 + 2\sigma$)		334	332	140	504	455

(b)

20° pipe specimen No.		1	2	3	4	5	6
Thickness [µm]	1	587.6	162.3	362.6	769.8	290.0	411.4
	2	452.2	366.7	433.1	798.0	304.3	419.8
	3	379.9	194.2	343.4	765.5	114.5	502.3
	4	274.1	145.8	144.7	776.1	71.6	520.4
	5	468.3	200.5	353.1	592.1	287.7	508.2
	6	358.6	156.3	423.6	558.9	285.1	499.3
	7	290.3	186.4	150.6	727.4	108.3	493.7
	8	554.6	342.6	358.7	739.5	128.3	489.7
Mean value h_0 [µm]		421	219	321	716	199	481
Standard deviation σ [µm]		115.3	85.9	112.1	89.8	100.9	41.2
Mean thickness h [µm] ($h_0 - 2\sigma$ to $h_0 + 2\sigma$)		421	219	321	716	199	481

Table 2.2 Thicknesses of the epoxy adhesive layers of (a) 20° and (b) 75° pipe specimens. Bold numbers are outliers that are more than 2σ from h_0.

(a)

45° pipe specimen No.		1	2	3	4	5	6
Thickness [μm]	1	293.3	386.5	1700.0	478.8	1179.0	671.3
	2	167.0	281.6	1033.0	499.0	1233.0	662.1
	3	214.3	474.5	461.9	276.2	600.2	697.1
	4	484.7	203.9	353.3	249.2	569.7	726.7
	5	300.5	286.7	915.4	311.9	488.5	431.4
	6	205.9	352.3	**2963.0**	300.6	419.4	341.1
	7	145.3	410.9	310.6	283.9	393.8	784.4
	8	473.6	345.9	244.0	266.5	424.7	798.8
Mean value h_0 [μm]		286	343	998	333	664	639
Standard deviation σ [μm]		131.2	84.7	934.0	98.1	342.9	165.3
Mean thickness h [μm] ($h_0 - 2\sigma$ to $h_0 + 2\sigma$)		286	343	717	333	664	639

(b)

75° pipe specimen No.		1	2	3	4	5
Thickness [μm]	1	750.0	596.8	1253.0	292.2	366.1
	2	450.1	410.8	327.3	262.8	343.5
	3	601.9	910.2	481.1	620.0	236.8
	4	312.3	727.5	156.7	618.9	255.8
	5	612.8	906.3	172.4	266.9	215.8
	6	331.0	796.5	318.6	305.2	199.2
	7	429.3	482.0	469.3	339.0	478.8
	8	312.3	608.5	887.1	342.3	473.7
Mean value h_0 [μm]		475	680	508	381	321
Standard deviation σ [μm]		163.5	186.6	379.0	150.0	112.1
Mean thickness h [μm] ($h_0 - 2\sigma$ to $h_0 + 2\sigma$)		475	680	508	381	321

2.2.2. Tensile testing and test results

Tensile tests were meticulously carried out utilizing a precision tensile testing machine, specifically AG-50kNX (Shimadzu Co., Ltd.), as shown in Fig. 2.3(a). The tests were conducted under ambient temperature conditions, maintaining a room temperature of 296.1 ± 5.7 K, while employing a crosshead speed (V_z) of 0.1 mm/min.

To further investigate the behavior of the cylindrical specimens during the tensile tests, strain gauges were thoughtfully affixed to the specimen's surface, as illustrated in Fig. 2.3(b). The test protocol dictated that the experiment be concluded when the applied load had subsided to a satisfactory degree. Notably, the number of specimens employed in this phase of the study amounted to 3, 6, 6, and 4 for inclination angles of φ = 0°, 20°, 45°, and 75°, respectively.

The ensuing load-displacement curves stemming from each tensile test are presented in Fig. 2.4. The horizontal axis quantifies the crosshead displacement of the tensile testing machine, while the legend identifier 'h' designates the average adhesive layer thickness for each specimen. Notably, for φ = 0°, 20°, and 45° (Fig. 2.4 (a), (b), and (c), respectively), a discernible and abrupt decline in load transpires once the proportional limit is exceeded. Conversely, for φ = 75° (Fig. 2.4 (d)), a non-linear deformation profile emerges beyond the proportional limit.

The failure of adhesive layers, in general, constitutes a multifaceted and nonlinear phenomenon profoundly influenced by the adhesive's viscoelastic and plastic properties, which are contingent upon hydrostatic pressure. This is attributed to the formation and expansion of vacancies within the adhesive layer. In this study, the evaluation protocol defines the proportional limit, which signifies the demarcation point between the linear elastic and nonlinear regions, as the pivotal point of adhesive failure strength, rather than the tensile strength at which adhesive failure occurs.

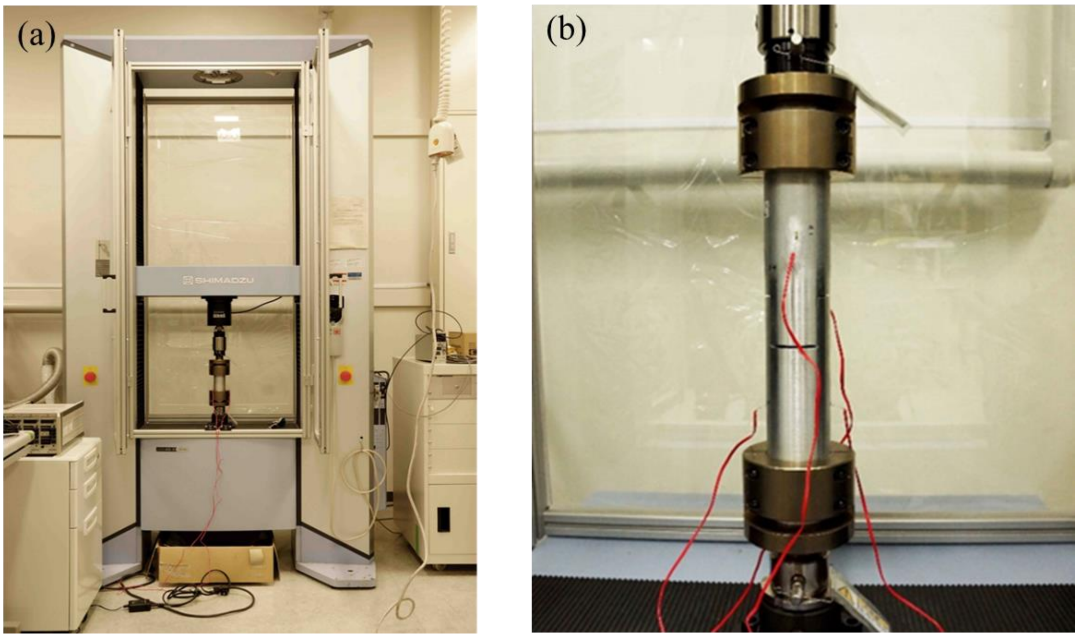

Fig. 2.3 (a) Tensile tests machine produced by Shimadzu Co., Ltd. (b) Specimens with strain gage attached

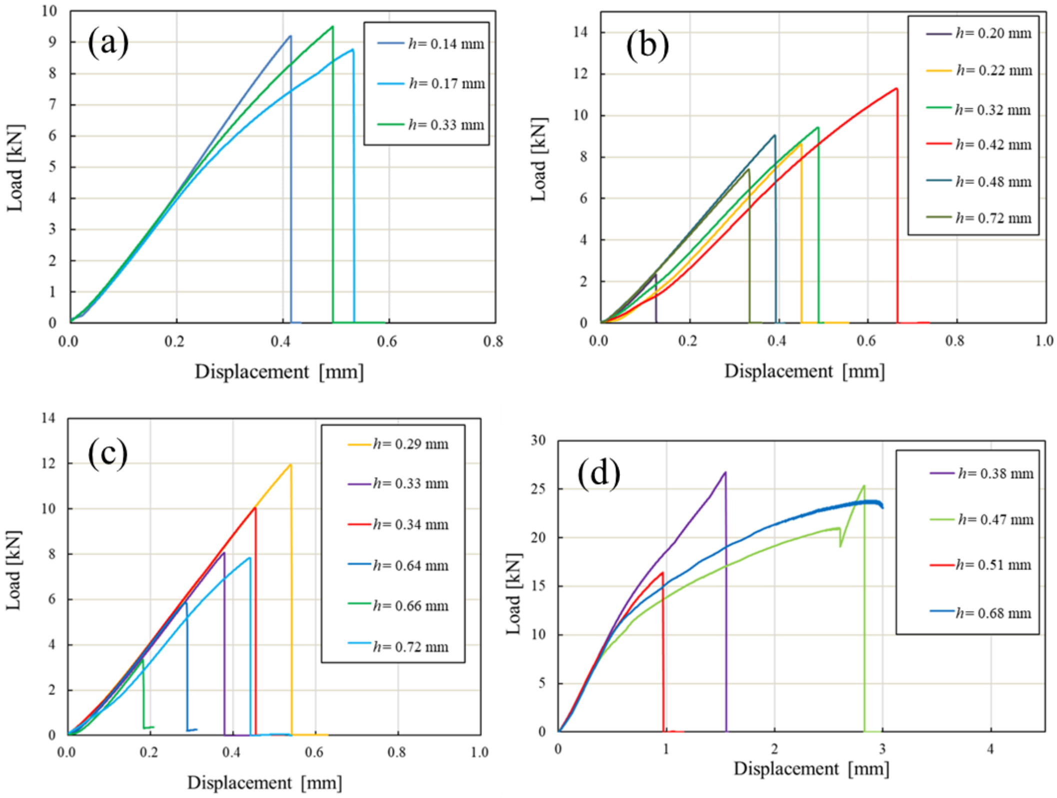

Fig 2.4 Load-displacement curves obtained from experiments; (a) $\varphi = 0°$, (b) $\varphi = 20°$, (c) $\varphi = 45°$, (d) $\varphi = 75°$.

2.3. Identification and comparison of failure criterion

I_1 and J_2 are calculated by the results of experiments according to Eqs. (2.5), (2.6), (2.7) and (2.8). The parameters c_1, c_2, and c_3 are estimated by the least squares fit as it is a quadratic function. According to the fitting, the parameters for the epoxy adhesive are newly obtained; c_1 is -9.03 [MPa], c_2 is 0.199 and c_3 is -11.5 [MPa^2] under c_0=1.00. The failure curve is obtained by $f = 0$, as shown in Fig. 2.5(a) with Poisson's ratio ν of 0.35 and the reference thickness because each sample has a different thickness in the manufacturing process. The previous result for acrylic adhesive with $\nu = 0.4$ [85] is drawn in Fig. 2.5(b) as a reference with $c_1 = -0.200$ [MPa], $c_2 = 0.0590$ and $c_3 = -14.0$ [MPa^2] under $c_0 = 1.00$. The failure criteria were established only from the experimental data collected from single-material pipes. In present research, the failure function is also established from multi-material pipe specimens and compared with the previous results to check if the failure function established from single-material pipes is also applicable. Fig. 2.5 is denoted using σ_m and τ_{oct} instead of I_1 and J_2 due to easier understanding of their magnitudes. The relationships between both quantities are expressed as $\sigma_m = \frac{1}{3} I_1$ and $\tau_{\mathrm{oct}} = \sqrt{\frac{2}{3} J_2}$.

Then, the comparison of adhesive materials between acrylic and epoxy adhesive materials is performed to identify the difference on the failure behaviors in multiaxial stress states. The overall strength of epoxy adhesive is larger than that of acrylic. More specifically, when σ_m is small, in other words, the degree of the adhesive surface of the pipe specimen is large, which means that the stress applied to the adhesive layer is almost shear only in acrylic adhesive and epoxy adhesive don't have much difference, while when σ_m increases, which means the stress applied to the adhesive layer changes from pure shear to the combination of shear force and the hydrostatic pressure acting on the adhesive layer getting large, the difference between τ_{oct} of acrylic adhesive and epoxy adhesive also increases. As a result, the strength against shear stress for both epoxy and acrylic adhesives are similar but the strength to hydrostatic pressure of epoxy adhesive is much higher than that of acrylic adhesive. Considering the reason for the difference in the hydrostatic pressure strength, the void nucleation and growth behaviors should be discussed. The void nucleation and growth behaviors in the adhesive layer are an important reason of the mean pressure dependence. During the tensile testing, the changes of adhesive layer are observed. For acrylic adhesive layer, the voids growth is obvious. While for epoxy adhesives, the change of adhesive layer is so minor that almost no voids appear in the adhesive layer. As a result, the effect of void nucleation and growth behaviors is major for acrylic adhesive but minor for epoxy adhesive. As hydrostatic pressure has similar meaning with mean pressure, it can deduce that the strength to hydrostatic pressure of epoxy adhesive is higher than that of acrylic adhesive. As a result, the failure function can be rewritten as:

$$f = c_0' \tau_{\mathrm{oct}}^2 + c_2' (\sigma_m - c_1')^2 + c_3', \tag{2.14}$$

Where $c_0' = \frac{3}{2} c_0$, $c_1' = -\frac{c_1}{6c_2}$, $c_2' = 9c_2$ and $c_3' = c_3 - \frac{c_1^2}{4c_2}$. The new parameters are $c_1' = 7.56$ [MPa], $c_2' = 1.79$ and $c_3' = -114$ [MPa^2] under $c_0' = 1.5$ for the epoxy, while on the other hand, $c_1' = 0.56$ [MPa], $c_2' = 0.531$ and $c_3' = -14.2$ [MPa^2] under $c_0' = 1.5$ for the acrylic using the data obtained in ref. [85]. c_1' suggests how large the hydrostatic pressure (mean stress) affects the maximum distorsional strength of adhesive material. The former is much larger than the latter and thus the epoxy adhesive can provide the maximum strength under dilatation circumstance of around 7.6 [MPa]. Recall that some linear dashed lines in Fig. 2.5 show the relationship of Eq. (2.11). Each slope equals to $\sqrt{6}k$, where $k(\varphi, v)$ is in Eq. (2.11) and determined only by the different angle φ for the same Poisson's ratio.

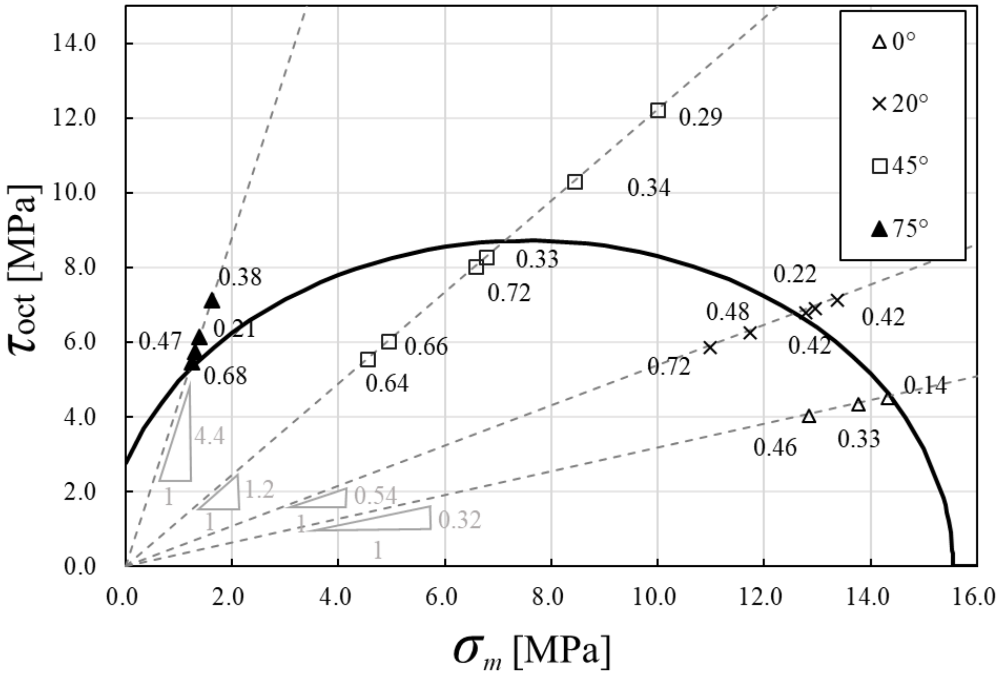

(a) Epoxy adhesive

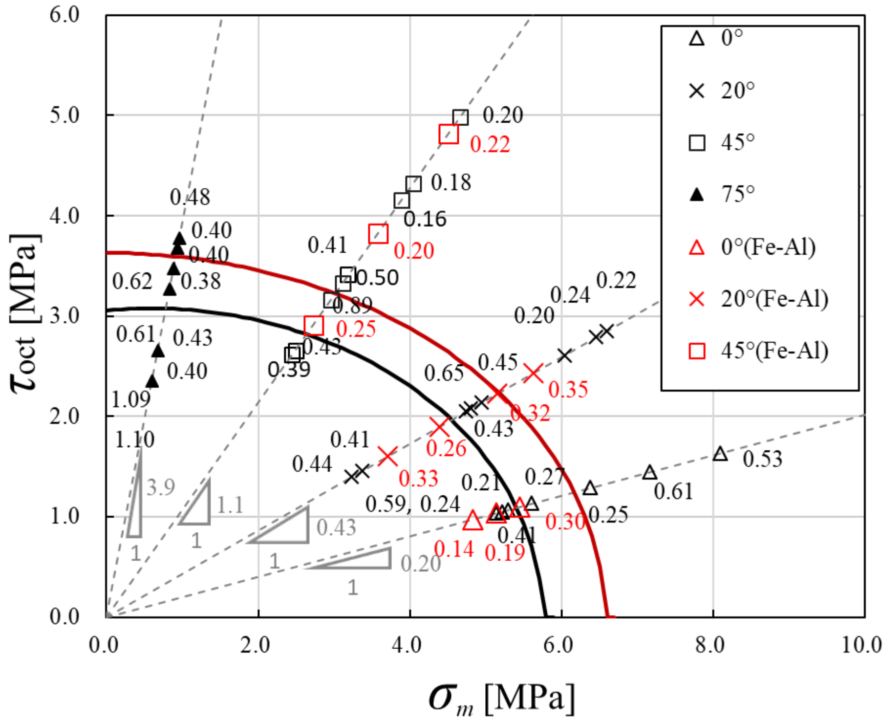

(b) Acrylic adhesive

Fig. 2.5 Failure criterion estimated from experiment results. The number beside the data point shows the average thickness of the adhesive layer of the pipe specimen. (a) Epoxy adhesive (EP-171) (b) Acrylic adhesive (M-600-08), the red data points indicate the experience data collected from pipes with different materials.

2.4. Thickness dependence of the adhesive layer

Whenever the failure of materials is discussed, it is usually determined only by the intrinsic strength of materials such as yield stress. However, in the adhesive problem, the factors affecting the strength are not only properties of adhesive materials but also the other geometric factors of structure. Among those factors, thickness of adhesive layer has the most significant effect. As a result, the failure function should be reconsidered as it is not applicable to adhesive layers with different thickness [106]. A scale function, δ, which extends the failure criterion of Eq. (2.13) to different adhesive layer thickness, has been formulated based on the reference thickness h^*[107]:

$$\delta = \frac{(\sigma_m - x_0)^2}{a^2} + \frac{{\tau_{\text{oct}}}^2}{b^2},$$
$$\text{where } |a| = \frac{1}{3}\sqrt{\frac{c_1^2}{4c_2^2} - \frac{c_3}{c_2}}, |b| = \sqrt{\frac{c_1^2}{36c_2^2} - c_3} \text{ and } x_0 = -\frac{c_1}{6c_2}. \tag{2.15}$$

δ was set to 1 when a point (σ_m, τ_{oct}) is located on the curve of failure function. All the failure magnitude (σ_m, τ_{oct}) of pipe specimen with different thicknesses h have been substituted into Eq. (2.15) to get the δ. And then, the power law of $\delta \propto h^{-0.20}$ for the epoxy adhesive is obtained in reference to $\delta \propto h^{-0.60}$ for the acrylic adhesive [85], as shown in Fig. 2.6, by a least square fitting between log δ and log h. The reference thickness was found when log δ = 0 because the parameters in Eq. (2.13) are fitted under f = 0. The reference thickness h^* is 0.3 mm for epoxy and 0.4 mm for acrylic. The absolute value of the power exponent of epoxy adhesive is much smaller than that of acrylic adhesive. This result suggests that thickness dependence to the failure of epoxy adhesive is much weaker than that of acrylic adhesive. A new coefficient c_3^* of the failure function which indicates the dependence to the thickness was finally calculated according to Eq. (2.15) as:

$$c_3^* = b^2 \left\{ \frac{x_0^2}{a^2} - \left(\frac{h}{h^*} \right)^p \right\}. \tag{2.16}$$

where p is the power exponent which is -0.20 with $h^* = 0.30$ [mm] for epoxy and -0.60 with $h^* = 0.40$ [mm] for acrylic. By modifying the new coefficient c_3^*, the failure function could be applied to adhesive layer with various thicknesses as shown in Fig. 2.7. Comparing the results here, for epoxy adhesive, the curves separate in a relatively small range. While for acrylic adhesive, the curves changed rapidly and separate in a relatively large range. Considering the reason of the difference on the thickness dependence of two adhesives, like mentioned before, the strength against the hydro static pressure of epoxy adhesive is much higher than that of acrylic adhesive, as mentioned before. Also, as hydrostatic pressure was the main factor which caused the voids occurred in the adhesive layer, it is easier for the void to occur for acrylic adhesive layer. If the thickness of layer differ a lot, the effect of the voids will also be obvious, as a result for acrylic adhesive, the strength will differ a lot according to the differences on thickness, in other words. The thickness dependence of acrylic is stronger than that of epoxy adhesive.

While the thickness dependence is one of the most important structural factors, the material properties of adhered materials are also the other important factor which affects the strength of the adhesive structure. The red curve shown in Fig. 2.5 (b) is established from the experimental data of multi-material pipes jointed by acrylic adhesive, which consist of SS400 steel pipe and A5052 aluminum pipe with the outer radius of 45 mm and the thickness of 3 mm. As the numbers of samples are limited, c_1 is set to 0 in the least square fit because the previous result for the single-material pipes [85] gives us the c_1 close to 0. The parameters are finally obtained as $c_1 = 0$ [MPa], $c_2 = 0.0515$ and $c_3 = -19.8$ [MPa^2] under $c_0 = 1.00$ for the multi-material curve and as $c_1 = -0.200$ [MPa], $c_2 = 0.0590$ and $c_3 = -14.0$ [MPa^2] under $c_0 = 1.00$ for the single-material.

Comparing the quantities of the parameters, c_1s for both is almost zero and c_2s for both also has similar value with the difference for just 10%. This result shows that the overall shapes of the single-material failure function and the multi-material failure function are almost the same and the only difference is the coefficient c_3. In other words, this difference can be treated as the failure function for adhesive layer with different thickness. As a result, the function can be modified to make them applicable to each other just by changing a new coefficient c_3^* which is modified by h^* according to Eq. (2.16). If the appropriate h^* is chosen, the multi-material failure curve can be transferred to keep identical with the single-material one which means they have the same property.

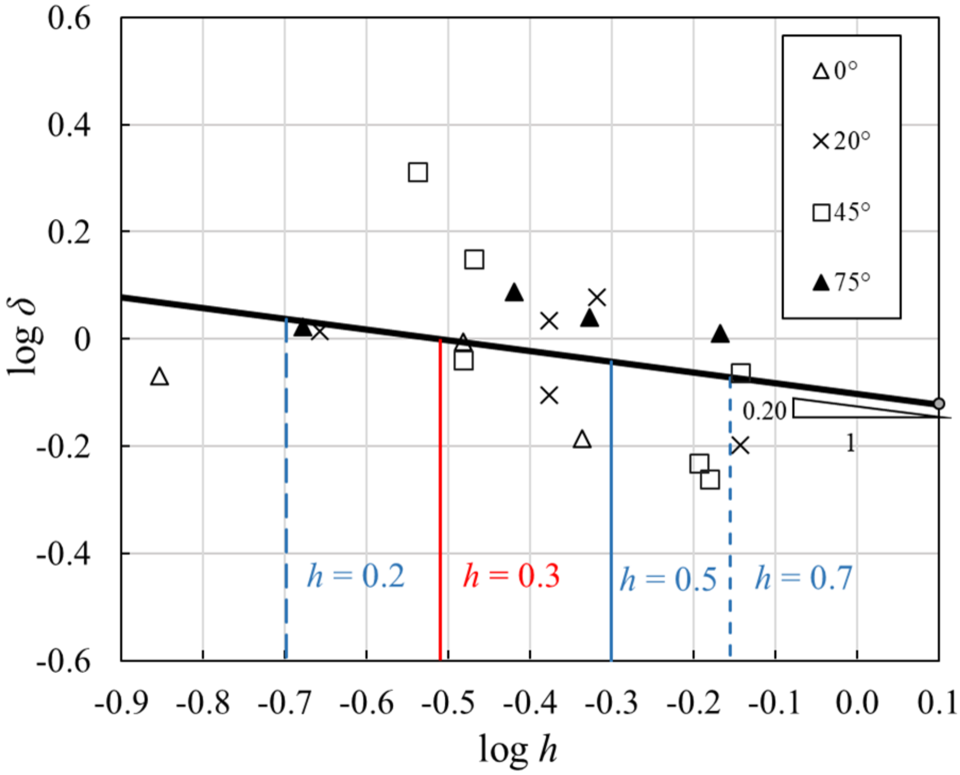

(a)

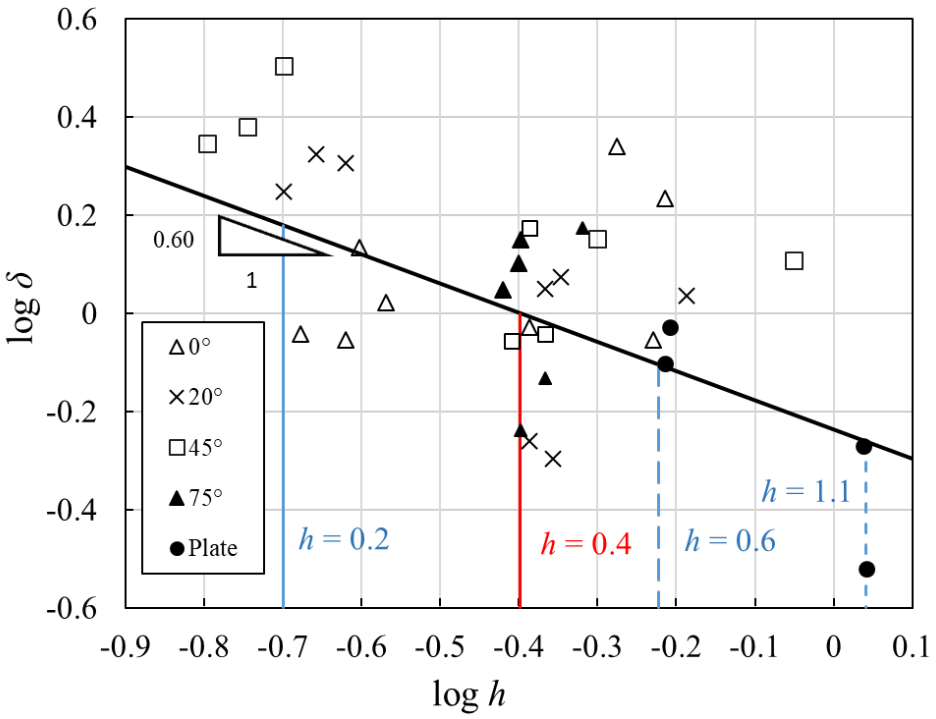

(b)

Fig. 2.6 Power law of the relation between the scale function δ and thickness h. (a) Epoxy adhesive and (b) acrylic adhesive.

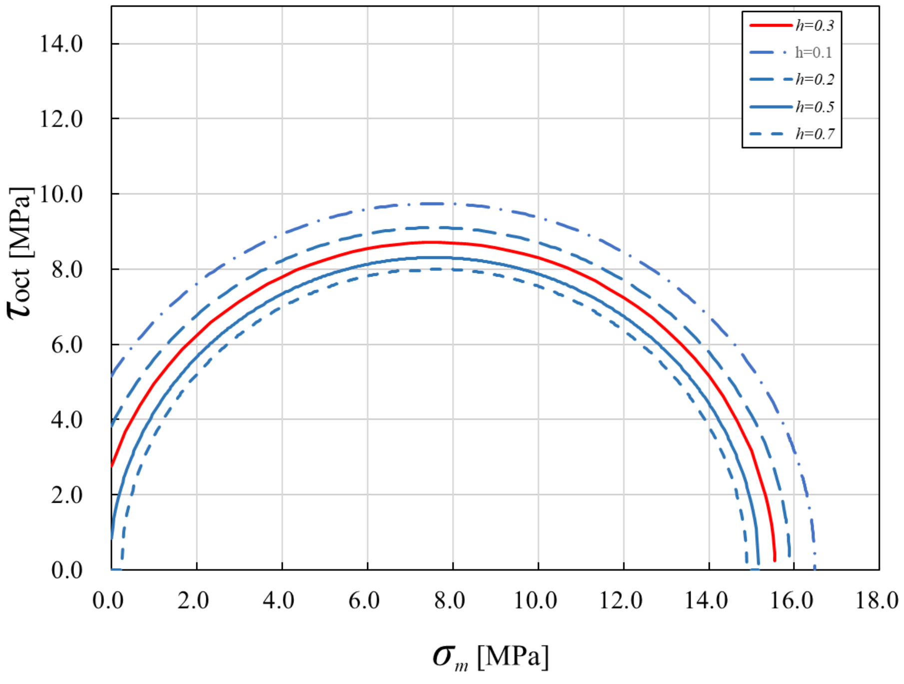

(a)

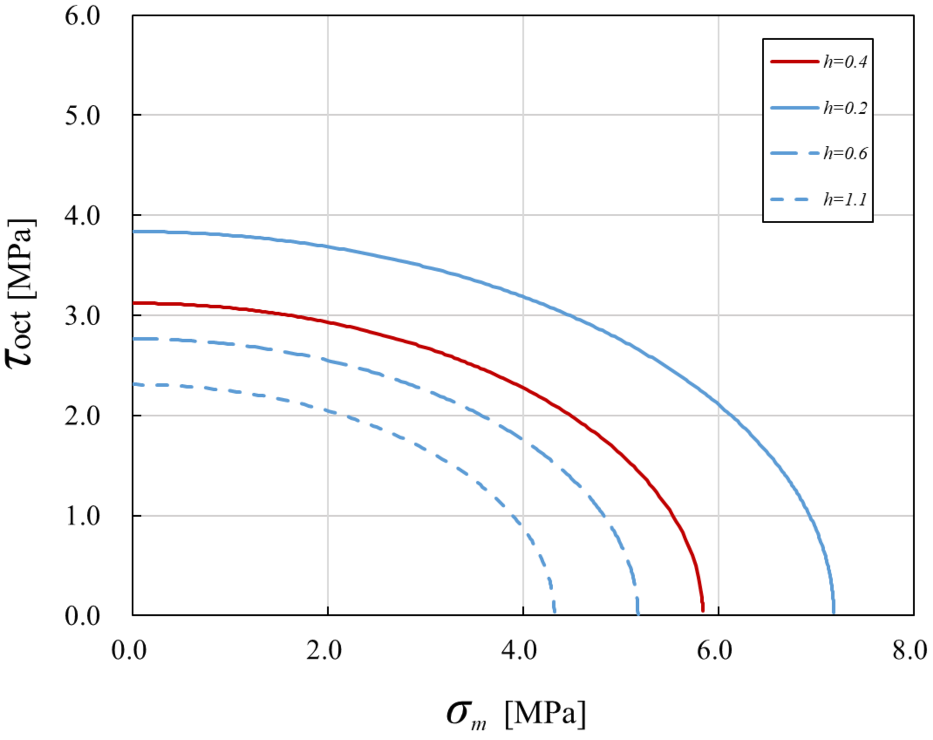

(b)

Fig. 2.7 The failure criterion dependent to the various thickness *h*. (a) epoxy adhesive, (b) acrylic adhesive [85]

2.5. Conclusion

The failure function of the epoxy adhesive was obtained from the tensile testing using pipe specimens with inclined cutting surface as there exists a multiaxial stress state at the adhesive interface.

The obtained failure function of epoxy adhesive was compared with the failure function of acrylic adhesives obtained in ref. [85]. Both adhesives have a strong mean stress dependence. The epoxy adhesive has relatively larger strength and the strength to hydrostatic pressure is much larger than epoxy adhesive. As there is a non-zero peak points for epoxy adhesive, the failure function was rewritten as Eq. (2.14) suggesting the place where the hydrostatic pressure affects the maximum distortional strength of adhesive material.

The power law for epoxy adhesive was obtained and compared with that for acrylic adhesive to exam the thickness dependence of the adhesives and the failure criterion for different mean thickness h were obtained that . According to the comparison, Thickness dependence is weaker in the epoxy adhesive layer than that in the acrylic adhesive layer. According to the thickness dependence and the results of multi-material specimens shown in Fig. 2.5 (b), the function can be modified to make them applicable to each other just by changing a new coefficient c_3^* which is modified by h^* according to Eq. (2.16). If the appropriate h^* is chosen, the multi-material failure curve can be transferred to keep identical with the single-material one which means they have the same property.

3. Shape Optimization of Adhesive Layer

To successfully engineer a multi-material bonded structure, it is imperative to conduct a comprehensive assessment of the structural integrity of the bonded components under multi-axial stress conditions. Equally critical thing is the provision of clear design guidelines that delineate the appropriate structural configurations to be employed based on the outcomes of strength evaluations.

As elaborated in Ch. 2, the strength evaluation methodologies for multi-axial stress conditions encompasses failure functions, quadratic stress criteria, and various other relevant approaches. In the pursuit of identifying the material parameters necessary for these evaluations, several test methodologies are at our disposal. These include the Napkin ring test method, wherein both tensile loads and torque are applied to test specimens, as well as the Arcan and Arcan tests, all of which are elaborated upon in Chapter 2. Furthermore, the innovative approach of subjecting cylindrical specimens with inclined adhesive layers to tensile tests, as expounded in Ch. 2, offers a valuable avenue for material parameter identification. The insights garnered through these testing methods enable the evaluation of the structural strength of multi-material adhesive structures, ultimately facilitating informed and effective design decisions.

As highlighted in the preceding section, it is evident that structural factors exert a substantial influence on the strength of adhesive structures. Consequently, to enhance the strength of adhesive structures, it is imperative to consider not only the inherent material properties of the adhesive but also to delve into the realm of optimal structural design. This chapter embarks on the journey of shape optimization for the bonding interface, a pivotal undertaking aimed at fortifying bond strength, grounded in the failure function gleaned from the experimental outcomes presented in Chapter 2. To obviate stress concentration vulnerabilities at the open ends, a thin-walled cylindrical butt-bonded structure is employed as the analytical model for the shape optimization exercise. This analytical model is subjected to a combined load consisting of tensile stress and torque applied at the terminal end. To impart a comparative dimension to the study, two distinct adhesive materials, namely epoxy and acrylic, are deployed and juxtaposed against each other. This comparative approach seeks to elucidate how the optimal design configurations may vary concomitantly upon the specific adhesive material utilized.

3.1. Shape optimization problem for multi-material bonding interface

In order to perform the shape optimal design of adhesive structures which is induced to minimize the stress operated in the adhesive layer under the multiaxial stress state, the objective function should be formulated [90]. The multi-material region with the adhesive layer is shown in Fig. 3.1.

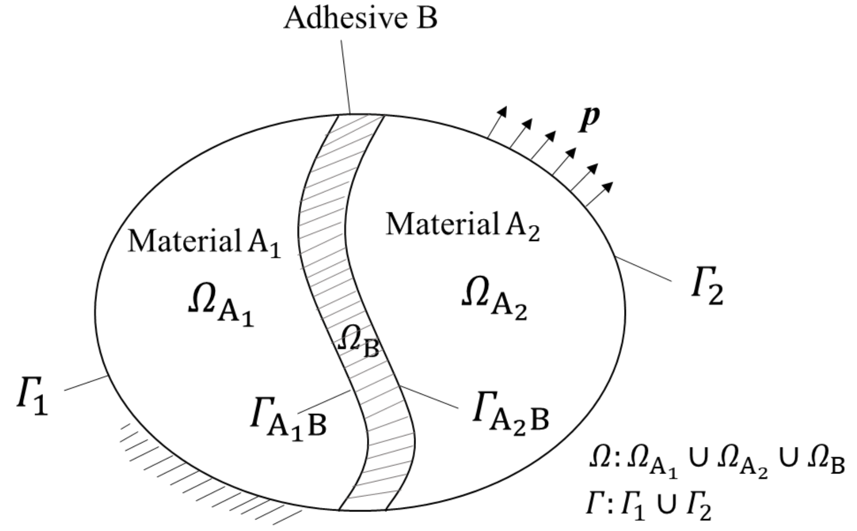

Fig. 3.1 Multi-material model consisting of two materials of A_1 and A_2 bonded by adhesion of *B*; suppose that traction *p* is applied at boundary Γ_2 and body force *f* acts in Ω. The region is kinematically supported at boundary Γ_1.

The following governing equations including equilibrium equation, boundary conditions and continuity conditions at the interface hold in the region $\Omega_m (m = \mathrm{A}_1, \mathrm{A}_2, \mathrm{B})$ with the boundary region of Γ_1, Γ_2 and $\Gamma_{m\mathrm{B}}$ $(m = \mathrm{A}_1, \mathrm{A}_2)$ in Fig. 3.4.

$$\sigma^m_{ij,j} + f_i = 0 \text{ in } \Omega_m \ (m = \mathrm{A}_1, \mathrm{A}_2, \mathrm{B}), \tag{3.1}$$

$$u_i = 0 \text{ on } \Gamma_1, \tag{3.2}$$

$$\sigma_{ij} n_j = p_i \text{ on } \Gamma_2, \tag{2.3}$$

$$\sigma^m_{ij} n^m_j = -\sigma^B_{ij} n^B_j \text{ on } \Gamma_{m\mathrm{B}} \ (m = \mathrm{A}_1, \mathrm{A}_2). \tag{3.4}$$

Here, $\boldsymbol{p}$ is the surface traction vector, $\boldsymbol{f}$ is the body force vector and $\boldsymbol{n}$ is the normal vector of the boundary. The linear and bilinear functions are defined as following:

$$a_m(\boldsymbol{u},\boldsymbol{v}) = \int_{\Omega_m} \sigma_{ij}^m(\boldsymbol{u})\varepsilon_{ij}^m(\boldsymbol{v})d\Omega \;(m = \mathrm{A}_1, \mathrm{A}_2, \mathrm{B}), \tag{3.5}$$

$$l(\boldsymbol{v}) = \int_{\Gamma_2} p_i v_i d\Gamma + \int_{\Omega} f_i v_i \, d\Omega, \tag{3.6}$$

$$h_{1m}(\boldsymbol{u},\boldsymbol{v}) = \int_{\Gamma_{A_1B}} \sigma_{ij}^m(\boldsymbol{u}) n_j^m v_i d\Gamma \;\; (m = \mathrm{A}_1, \mathrm{B}), \tag{3.7}$$

$$h_{2m}(\boldsymbol{u},\boldsymbol{v}) = \int_{\Gamma_{A_2B}} \sigma_{ij}^m(\boldsymbol{u}) n_j^m v_i d\Gamma \;\; (m = \mathrm{A}_2, \mathrm{B}), \tag{3.8}$$

where $\boldsymbol{v}$ is an adjoint variable of the function space $\boldsymbol{\mathcal{U}}$ expressed by the following equation:

$$\boldsymbol{\mathcal{U}} = \{\boldsymbol{v} \in H^1(\Omega;\, \mathcal{R}^3) | \boldsymbol{v} = 0 \text{ on } \Gamma_1 \}. \tag{3.9}$$

The governing Eqs. (3.1) to (3.3) can be expressed using Eqs. (3.5) to (3.8) based on the principal of virtual work.

$$\begin{gathered} a_{A_1}(\boldsymbol{u},\boldsymbol{v}) - h_{1\mathrm{A}_1}(\boldsymbol{u},\boldsymbol{v}) + a_{\mathrm{A}_2}(\boldsymbol{u},\boldsymbol{v}) - h_{2\mathrm{A}_2}(\boldsymbol{u},\boldsymbol{v}) + \\ a_B(\boldsymbol{u},\boldsymbol{v}) - h_{1\mathrm{B}}(\boldsymbol{u},\boldsymbol{v}) - h_{2\mathrm{B}}(\boldsymbol{u},\boldsymbol{v}) - l(\boldsymbol{v}) = 0, \forall \boldsymbol{v} \in \boldsymbol{\mathcal{U}}. \end{gathered} \tag{3.10}$$

The displacement $\boldsymbol{u}$ required to calculate the objective function must always satisfy the above governing Eq. (3.10).

It is assumed that $\boldsymbol{v}$ is a continuous function on the interface $\Gamma_{\mathrm{A}_1\mathrm{B}}$ and $\Gamma_{\mathrm{A}_2\mathrm{B}}$ as follows:

$$v^m = v^B \text{ on } \Gamma_{m\mathrm{B}} \;(m = \mathrm{A}_1, \mathrm{A}_2). \tag{3.11}$$

Then, according to Eqs. (3.4) and (3.11), governing Eq. (3.10) can be simplified as:

$$a_{\mathrm{A}_1}(\boldsymbol{u},\boldsymbol{v}) + a_{\mathrm{A}_2}(\boldsymbol{u},\boldsymbol{v}) + a_{\mathrm{B}}(\boldsymbol{u},\boldsymbol{v}) - l(\boldsymbol{v}) = 0, \forall \boldsymbol{v} \in \boldsymbol{\mathcal{U}}. \tag{3.12}$$

The failure function f based on Eq. (2.13) has a different value dependent to the stresses occurring in the adhesive layer and the failure happens when $f = 0$. In order to enhance the strength of the adhesive structure, the values of failure function f are supposed to become uniform throughout the adhesive layer for the applied stress to be minimized as much as possible. Therefore, the object function is to minimize it in the adhesive layer region Ω_B as the sum of squares of failure function f occurring in the whole adhesive layer as follows [90].

$$\text{Find } \Omega_{\mathrm{B}} : \min_{\Omega_{\mathrm{B}}} F \text{, where } F = \frac{\int_{\Omega_{\mathrm{B}}} (f - c_3)^2 d\Omega}{\int_{\Omega_{\mathrm{B}}} d\Omega}. \tag{3.13}$$

In order to avoid diminishment and disappearance of the adhesive layer region Ω_B, the constant volume constraint on Ω_B is imposed. As a result, the shape optimization problem of the adhesive interface for the multi-material region becomes the following formulas.

$$\min_{\Omega_{\mathrm{B}}} F(I_1, J_2),$$

$$\text{subject to Boundary} - \text{value problem and} \tag{3.14}$$

$$V_{\mathrm{B}} = \bar{V}_{\mathrm{B}} \text{ where } V_{\mathrm{B}} = \int_{\Omega_{\mathrm{B}}} d\Omega.$$

where $\bar{V}_B$ is the initial volume of the adhesive layer.

The traction method [108] is used to calculate the adjoint velocity field $\boldsymbol{V}$. For this purpose, it is necessary to derive the shape gradient function that acts as an external force term in the traction method. According to the optimization problem set in Eq. (3.14), a Lagrange functional is defined as:

$$L = \frac{\int_{\Omega_{\mathrm{B}}} (f - c_3)^2 d\Omega}{\int_{\Omega_{\mathrm{B}}} d\Omega} - \begin{bmatrix} a_{\mathrm{A}_1}(\boldsymbol{u}, \boldsymbol{v}) - h_{1\mathrm{A}_1}(\boldsymbol{u}, \boldsymbol{v}) + a_{\mathrm{A}_2}(\boldsymbol{u}, \boldsymbol{v}) - h_{2\mathrm{A}_2}(\boldsymbol{u}, \boldsymbol{v}) \\ + a_B(\boldsymbol{u}, \boldsymbol{v}) - h_{1\mathrm{B}}(\boldsymbol{u}, \boldsymbol{v}) - h_{2\mathrm{B}}(\boldsymbol{u}, \boldsymbol{v}) - l(\boldsymbol{v}) \end{bmatrix}$$
$$+ \Lambda(V_{\mathrm{B}} - \bar{V}_{\mathrm{B}}). \tag{3.15}$$

Here, Λ is the undetermined multiplier of Lagrange. Then, the time derivative of the Lagrange functional $\dot{L}$ for the domain variation according to the velocity field $\boldsymbol{\mathcal{V}}$ becomes the following formula:

$$\dot{L} = -[a_{\mathrm{A}_1}(\boldsymbol{u},\boldsymbol{v}') + a_{\mathrm{A}_2}(\boldsymbol{u},\boldsymbol{v}') + a_{\mathrm{B}}(\boldsymbol{u},\boldsymbol{v}') - l(\boldsymbol{v}')]$$

$$-\left[a_{\mathrm{A}_1}(\boldsymbol{u}',\boldsymbol{v}) + a_{\mathrm{A}_2}(\boldsymbol{u}',\boldsymbol{v}) + a_{\mathrm{B}}(\boldsymbol{u}',\boldsymbol{v}) - \frac{2\int_{\Omega_{\mathrm{B}}} f'(f-c_3)^2 d\Omega}{\int_{\Omega_{\mathrm{B}}} d\Omega}\right]$$
$$+\Lambda'(V_{\mathrm{B}} - \bar{V}_{\mathrm{B}}) + l_G(\boldsymbol{\mathcal{V}}), \tag{3.16}$$

$$l_G(\boldsymbol{\mathcal{V}}) = \int_{\Gamma_{\mathrm{A_1B}}} G_{\mathrm{A_1B}}\,\boldsymbol{n}\cdot\boldsymbol{\mathcal{V}}\mathrm{d}\Gamma + \int_{\Gamma_{\mathrm{A_2B}}} G_{\mathrm{A_2B}}\,\boldsymbol{n}\cdot\boldsymbol{\mathcal{V}}\mathrm{d}\Gamma, \tag{3.17}$$

$$G_{m\mathrm{B}} = \frac{(f-c_3)^2}{\int_{\Omega_{\mathrm{B}}} d\Omega} - \frac{\int_{\Omega_{\mathrm{B}}}(f-c_3)^2 d\Omega}{\left(\int_{\Omega_{\mathrm{B}}} d\Omega\right)^2} - \left[\sigma_{ij}^{\mathrm{B}}(\boldsymbol{u})\varepsilon_{ij}^{\mathrm{B}}(\boldsymbol{v}) - \sigma_{ij}^{m}(\boldsymbol{u})\varepsilon_{ij}^{m}(\boldsymbol{v})\right]$$
$$+\sigma_{ij}^{\mathrm{B}} n_j^{\mathrm{B}}\left(v_{i,k}^{\mathrm{B}} - v_{i,k}^{m}\right)n_k^{\mathrm{B}} + \Lambda\ (m = \mathrm{A}_1, \mathrm{A}_2), \tag{3.18}$$

where it recalls that $(\cdot)'$ denotes the partial derivative for region variation. From Eq. (3.16), the term of the velocity field $\boldsymbol{\mathcal{V}}$ can be expressed by the shape gradient function $G_{\mathrm{A_1B}}$ and $G_{\mathrm{A_1B}}$ on the adhesive interface $\Gamma_{\mathrm{A_1B}}$ and $\Gamma_{\mathrm{A_2B}}$. According to Eq. (3.16), the optimal condition for $\boldsymbol{u}$, $\boldsymbol{v}$ and Λ of the Lagrange functional L is

$$a_{\mathrm{A}_1}(\boldsymbol{u},\boldsymbol{v}') + a_{\mathrm{A}_2}(\boldsymbol{u},\boldsymbol{v}') + a_{\mathrm{B}}(\boldsymbol{u},\boldsymbol{v}') - l(\boldsymbol{v}') = 0, \forall \boldsymbol{v}' \in \boldsymbol{\mathcal{U}}, \tag{3.19}$$

$$a_{\mathrm{A}_1}(\boldsymbol{u}',\boldsymbol{v}) + a_{\mathrm{A}_2}(\boldsymbol{u}',\boldsymbol{v}) + a_{\mathrm{B}}(\boldsymbol{u}',\boldsymbol{v}) - \frac{2\int_{\Omega_B} f'(f-c_3)^2 d\Omega}{\int_{\Omega_{\mathrm{B}}} d\Omega} = 0, \forall \boldsymbol{u}' \in \boldsymbol{\mathcal{U}}, \tag{3.20}$$

$$\Lambda'(V_{\mathrm{B}} - \bar{V}_{\mathrm{B}}) = 0. \tag{3.21}$$

Here Eq. (3.19) has the same meaning with the governing equation (3.12) calculating the displacement $\boldsymbol{u}$ by FEM analysis. Eq. (3.20) is the adjoint equation of the adjoint variable vector $\boldsymbol{v}$ and Eq. (3.21) is the constraint condition of the volume. According to the symmetry of a_m $(m = \mathrm{A}_1, \mathrm{A}_2)$ and the chain rule of partial derivative, Eq. (3.20) can be written as:

$$a_{\mathrm{A}_1}(\boldsymbol{v}, \boldsymbol{u}') + a_{\mathrm{A}_2}(\boldsymbol{v}, \boldsymbol{u}') + a_{\mathrm{B}}(\boldsymbol{v}, \boldsymbol{u}') - l_2(\boldsymbol{u}') = 0, \tag{3.22}$$

where $l_2(\boldsymbol{u}') = \int_{\Omega_B} \frac{2\int_{\Omega_{\mathrm{B}}} f'(f-c_3)^2 d\Omega}{\int_{\Omega_{\mathrm{B}}} d\Omega} \frac{\partial f}{\partial \sigma_{ij}} \frac{\partial \sigma_{ij}}{\partial u_k} \boldsymbol{u}'_k d\Omega, \forall \boldsymbol{u}' \in \boldsymbol{\mathcal{U}}$.

According to Eq. (3.22), the term of the external force *l* is replaced by l_2 and the adjoint variable vector $\boldsymbol{v}$ can be calculated by FEM analysis.

Finally, the velocity field $\boldsymbol{V}$ is calculated, which is used to update the shape of the adhesive layer according to the traction method as

$$a(\boldsymbol{V}, \boldsymbol{w}) = -l_G(w), \boldsymbol{V} \in C_{\Theta}, \forall \boldsymbol{w} \in C_{\Theta}. \tag{3.23}$$

Here, $a(\boldsymbol{V}, \boldsymbol{w})$ is the property value of adhesives, $l_G(\boldsymbol{w})$ is obtained according to Eq. (3.17) and C_{Θ} is the allowable function space that satisfies the constraint condition of region variation.

The flowchart of the numerical analysis for optimization is shown in Fig. 3.2 [85]. The displacement field $\boldsymbol{u}$ satisfying Eq. (3.19) is calculated by FEM analysis. The values of stress calculated from the FEM analysis are input into the failure function *f* of Eq. (2.13) and the objective function *F* is calculated. The result is then compared with the value of *F* in the previous step. If the difference of the values between the two steps is larger than 10^{-3}, the analysis keeps going. The vector field $\boldsymbol{v}$ which satisfies the adjoint equation (3.22) is calculated by FEM analysis. The obtained displacement field $\boldsymbol{u}$ and vector field $\boldsymbol{v}$ are used to calculate the shape gradient function according to Eq. (3.18). The velocity field $\boldsymbol{V}$ is then obtained from Eq. (3.23) by the traction method and is used to update the shape of the interface. The iteration keeps going until the change rate of objective function is less than 10^{-3}. Finally, the output result is the optimal design of the adhesive interface.

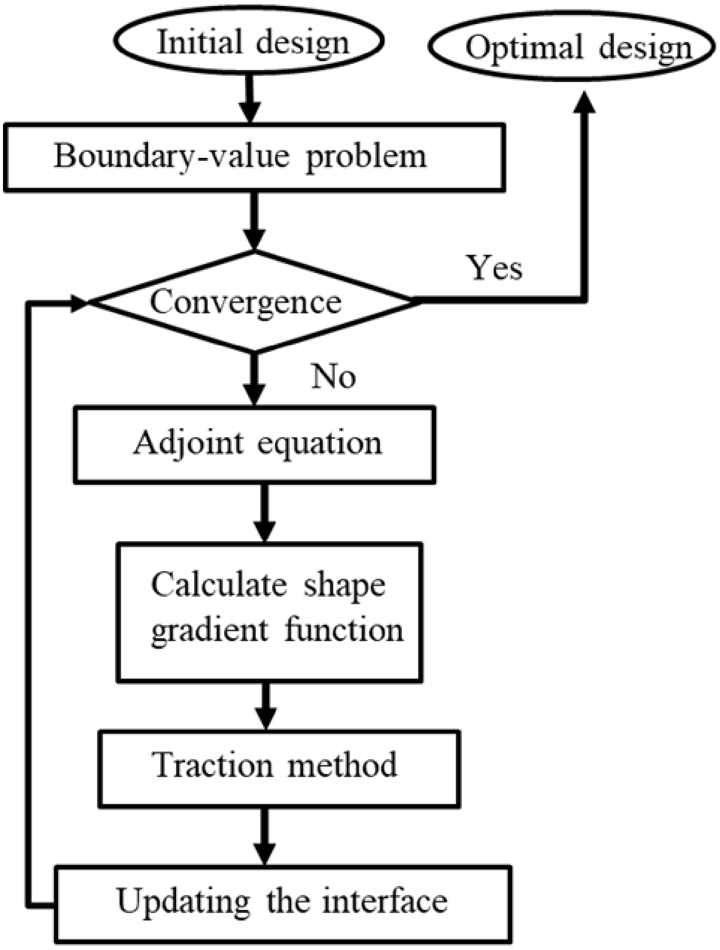

Fig. 3.2 The flowchart of the shape optimization process. The iteration will keep going on until the change rate of F is less than 10^{-3}

3.2. Model and conditions of optimization

A thin-wall pipe joint model which has the thickness of the adhesive with $0.13a$, where a is the diameter of pipe (a = 20 mm), is used in the optimization calculation as shown in Fig. 3.3. The elastic properties of adhered materials as well as adhesives are shown in Table 3.1 and the parameters of failure criterion are shown in Table 3.2. In order to simulate the stress state of the bonding between different materials, the upper (A_1 in Fig.

3.3) and lower (A_2 in Fig. 3.3) pipes are made of steel and aluminum, respectively. As mentioned in the previous section, there always exists a multiaxial stress state in the adhesive layer so that combined loading conditions should be considered in optimal design of the adhesive layer as shown in Fig. 3.4. Let α $(= \sigma/\tau)$ be a ratio of tensile stress σ by tension to shear stress τ by torsion, which are applied at both ends of the pipe far from the adhesive region. Three loading conditions are set as shown in Fig. 3.5. When α = 0, there is only torsion *T*. When α = 2, a combined loading with both torsion *T* and tension *F* applied. When $\alpha \to \infty$, there is only tension *F*.

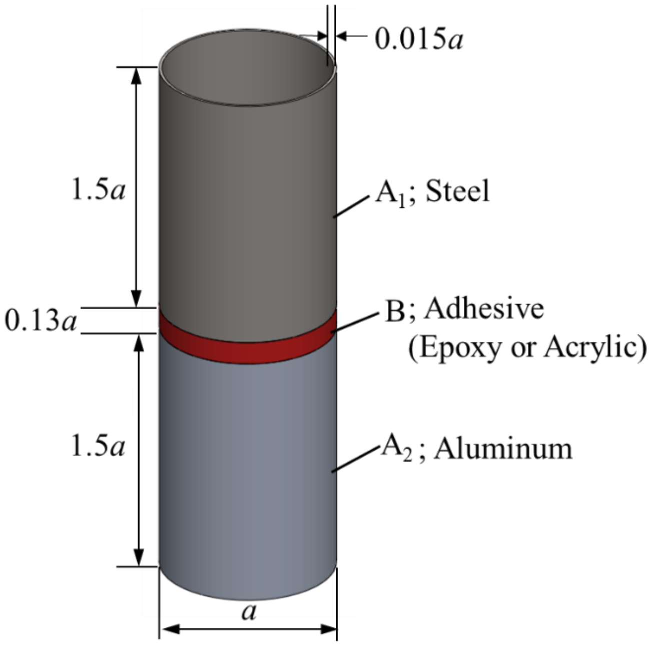

Fig. 3.3 Dimension of the thin-wall pipe model used in the optimization analysis. Two halves are made of different materials and bonded by the adhesives.

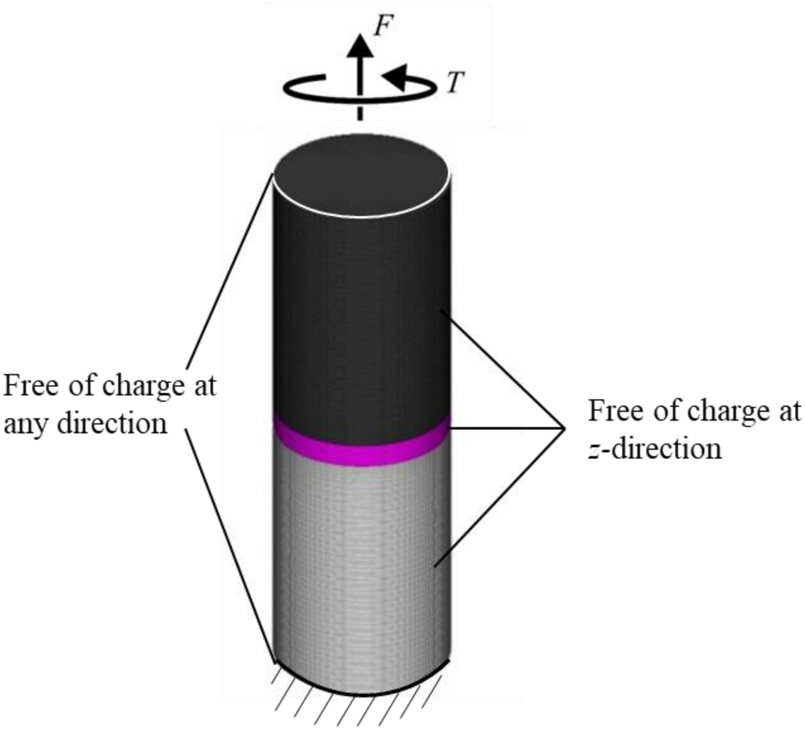

Fig. 3.4 Boundary condition and initial torsion-tension combined load of FEM model.

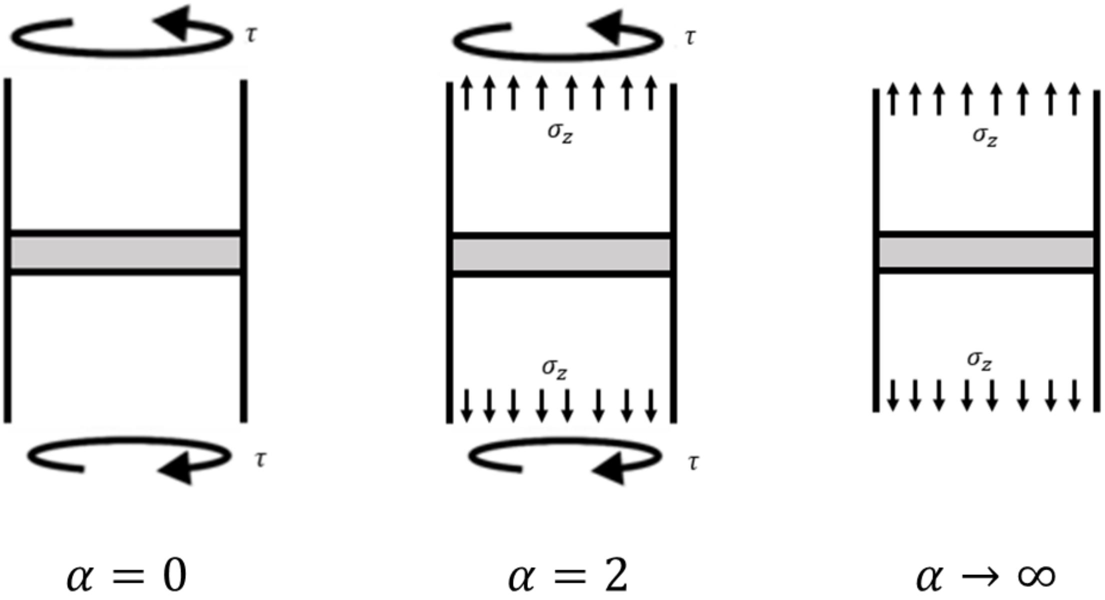

Fig. 3.5 Three different loading conditions of the optimization.

Table 3.1 Material properties of FEM model

Material	Young’s modulus [GPa]	Poisson’s ratio
Steel (A_1)	210	0.3
Aluminum (A_2)	70	0.3
Epoxy adhesive (B)	1.2	0.35
Acrylic adhesive (B)	0.35	0.4

Table 3.2 Material parameters of failure functions for adhesives (B)

Material	c_0	c_1	c_2	c_3
Epoxy adhesive	1.00	-9.03	0.199	-11.5
Acrylic adhesive	1.00	-0.200	0.0590	-14.0

3.3. Shape optimization results and comparison

The optimization calculations using epoxy adhesives are obtained under three different loading conditions. These results are compared with the optimization results of acrylic adhesive in ref. [85]. The objective function and volume curves under three loading conditions are shown in Fig. 3.6. These data are normalized by the initial values of objective function and the volume of the adhesive layer. In most situations, the values of objective functions decrease as the number of iterations increases, which implies the reasonable success of the minimization. For the cases of epoxy with $\alpha = 0$ and acrylic with $\alpha \rightarrow \infty$, the objective functions slightly increase or don’t change at all because the original shapes are optimal and thus the initial value of objective function is minimal.

(a) $\alpha = 0$

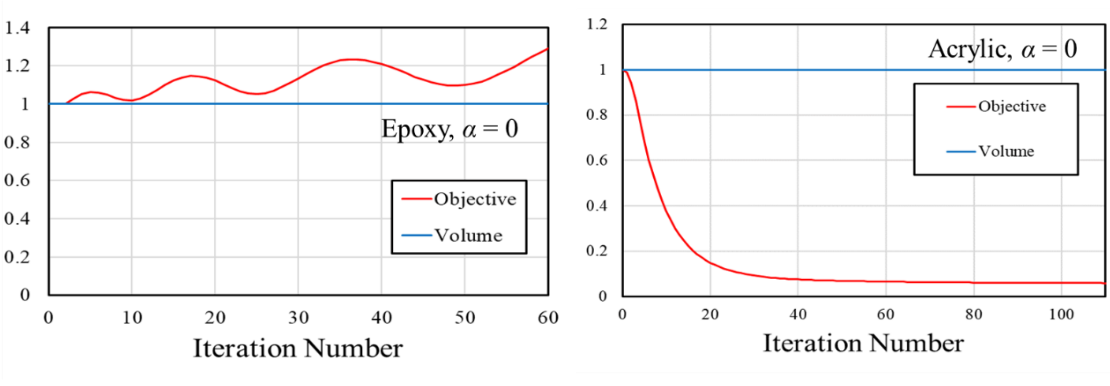

(b) $\alpha = 2$

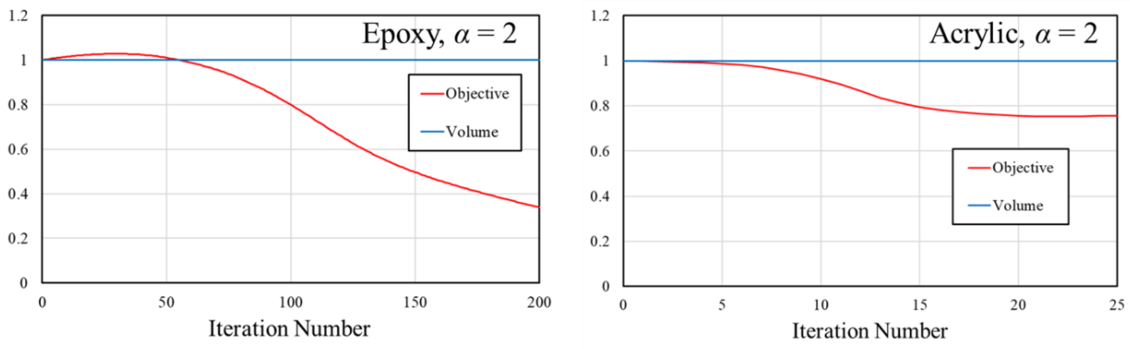

(c) $\alpha \to \infty$

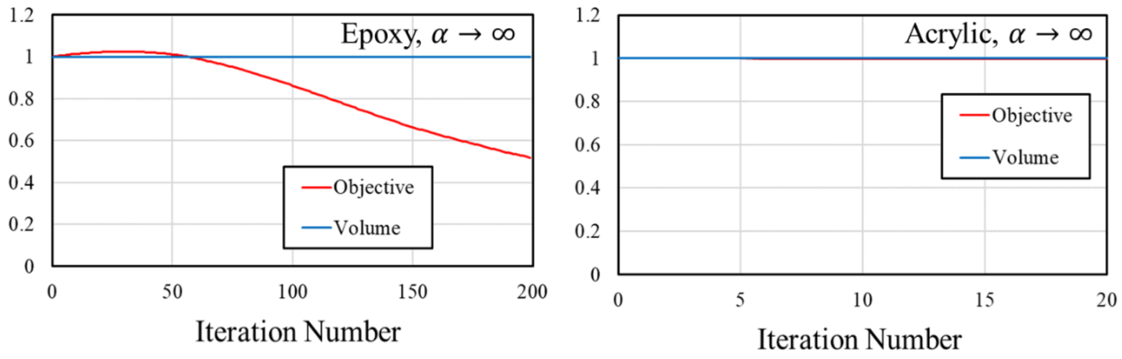

Fig 3.6 The objective functions according to the iteration number of optimizations under three different loading conditions. (a) $\alpha = 0$, (b) $\alpha = 2$ and (c) $\alpha \to \infty$.

The final shapes of the optimized interfaces of adhesive layers for epoxy and acrylic [85] adhesives are shown in Fig. 10 under the ratios of $\alpha = 0$ (only torsion), 2 and ∞

(only tension). The color map in Fig. 3.7 gives us equivalent stress (von Mises stress) distribution. From them, the averaged stress of 4.22 [MPa] is rather uniform in most parts of the adhesive layer and this value is much smaller than the averaged stress of 6.67 [MPa] in adhered material A_1 and 6.56 [MPa] in A_2. For different adhesives and different loading conditions, it is found that the optimization of adhesive structure has a strong dependence on the failure function of the employed adhesive material.

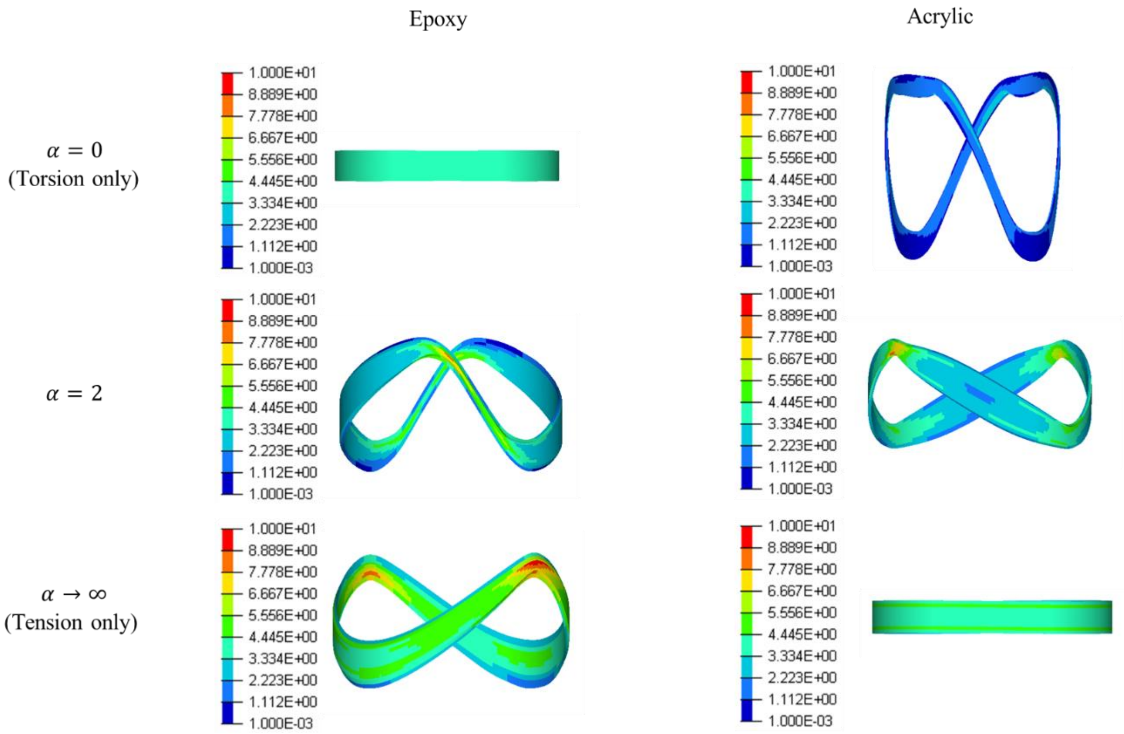

Fig. 3.7 Optimal design of the adhesive layer for epoxy and acrylic adhesives under three different loading conditions.

3.4. Discussion on the optimization process

3.4.1. Optimization process on the failure curve

In order to examine the optimization process in failure space, each step of the optimization is traced. According to Eq. (2.14), the failure happens when $f = 0$ and therefore any point $(\sigma_m, \tau_{\text{oct}})$ on the curve indicates the failure state of adhesive. In order to compare the results of optimization with those of experiments, the starting data points of the optimization could be scaled onto the failure curve obtained by experiment data because all the calculations were performed within the linear elasticity. As a result, the initial data points $(\sigma_m^0, \tau_{\mathrm{oct}}^0)$ can be transformed to the modified data points $(\sigma_m, \tau_{\mathrm{oct}})$ on the failure function curve by a multiplier *A* as follows:

$$\frac{\sigma_m}{\sigma_m^0} = \frac{\tau_{\mathrm{oct}}}{\tau_{\mathrm{oct}}^0} = A, \tag{3.24}$$

where *A* can be calculated by the initial value of $(\sigma_m^0, \tau_{\mathrm{oct}}^0)$ and the parameters of the failure function as follows:

$$A = \frac{-c_1'\sigma_m^0 + \sqrt{(c_1'\sigma_m^0)^2 - 4c_3'\left(c_0'\tau_{\mathrm{oct}}^0 + c_2'{\sigma_m^0}^2\right)}}{2\left(c_0'\tau_{\mathrm{oct}}^0 + c_2'{\sigma_m^0}^2\right)}, \tag{3.25}$$

On the second issue, optimization is to minimize the objective function in order to increase the strength of the adhesive structure to the failure. The distance of the design data point of the optimization from the origin in the failure space should be shortened so that the data points will get sufficiently inside from the failure curve. According to Fig. 2.5, the distance to the origin δ in the failure plane of σ_m and τ_{oct} can be calculated as follows because σ_m is orthogonal to τ_{oct} in Haigh–Westergard principal stress space.

$$\delta = \sqrt{\sigma_m^2 + \tau_{\mathrm{oct}}^2}\,. \tag{3.26}$$

The data points of optimization results were multiplied by *A* and transformed to put the initial point (*n*=0) onto the failure curve. The modified data points through the optimization processes under three different loading conditions are plotted in the failure space, as shown in Fig. 3.8. The enlarged views of the optimization processes, (I), (II) and (III), are shown in Fig. 3.9; (a) region (I) of α = 0, (b) region (II) of α = 2 and (c) region (III) of $\alpha \to \infty$. The data points for each 10 steps through the optimization iteration were all multiplied by *A* and the direction of the optimization is shown along arrows. In order to check whether the optimization process minimizes the object function, the distances δ normalized by the initial value of δ_0 are calculated as shown in Fig 3.10. It is obvious that δ is decreasing as the iteration number n and the process improves the structural integrity of the adhesive layer. The same results for acrylic adhesive in ref. [90] are shown in Fig 3.11, 3.12 and 3.13, respectively. From Figs. 3.10 and 3.13 the optimization can reduce the applied stress level for less than 30% from initial shape for the epoxy adhesive and up to 50% for the acrylic adhesive.

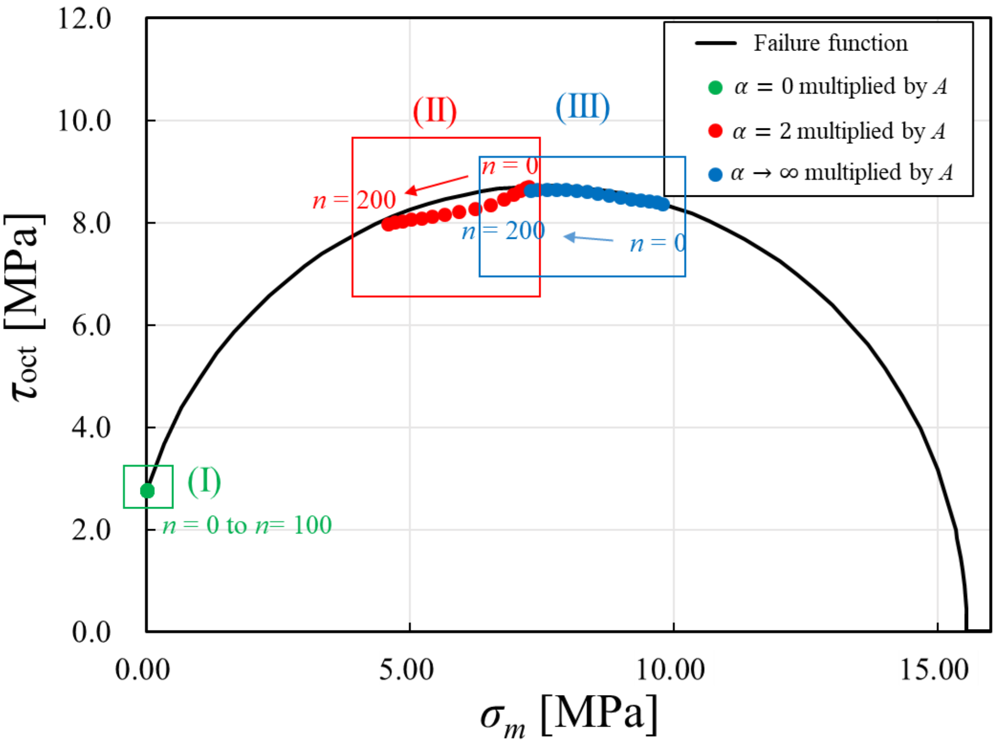

Fig. 3.8 The results of the optimization process on the failure function curve for the epoxy adhesive. The blue dots, red dots and green dots are the results for $\alpha = 0$, $\alpha = 2$ and $\alpha \to \infty$, respectively. n is the iteration number of the optimization.

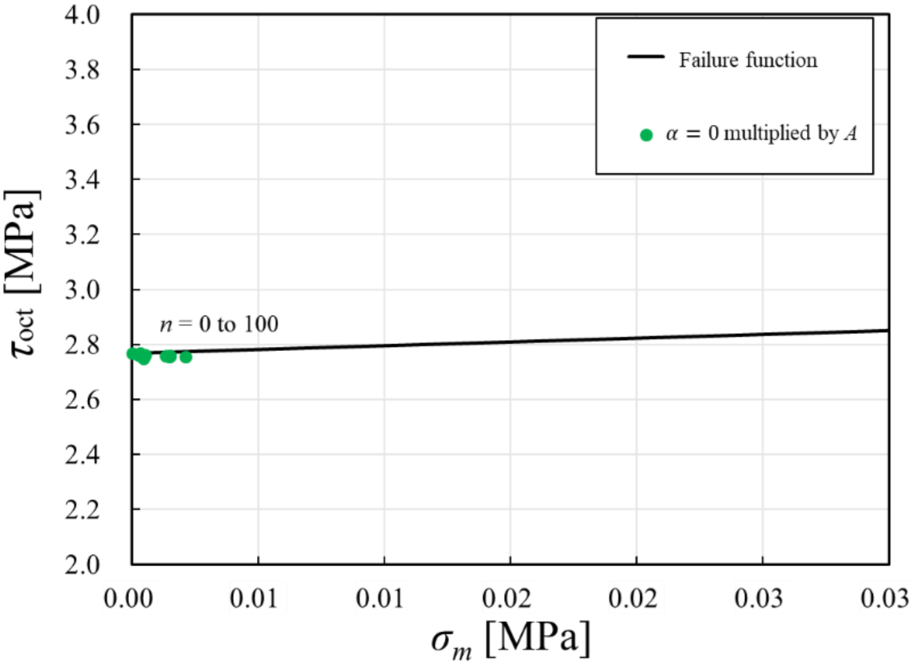

(a) Region (I) in Fig. 11

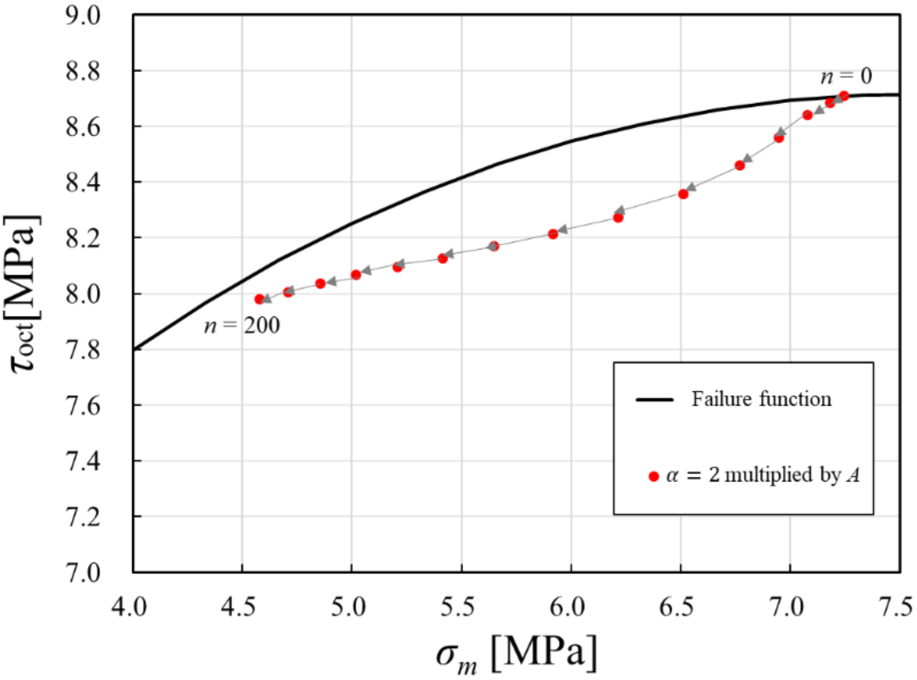

(b) Region (II) in Fig. 11

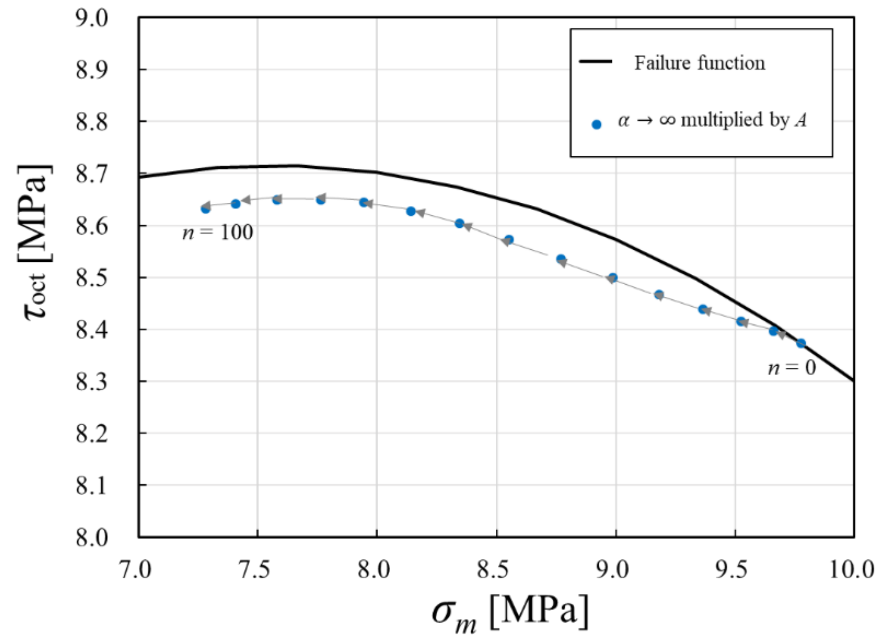

(c) Region (III) in Fig. 11

Fig. 3.9 The enlarged view of the optimization results of the epoxy adhesive multiplied by A. (a) Region (I) of $\alpha = 0$, (b) Region (II) of $\alpha = 2$ and (c) Region (III) of $\alpha \to \infty$.

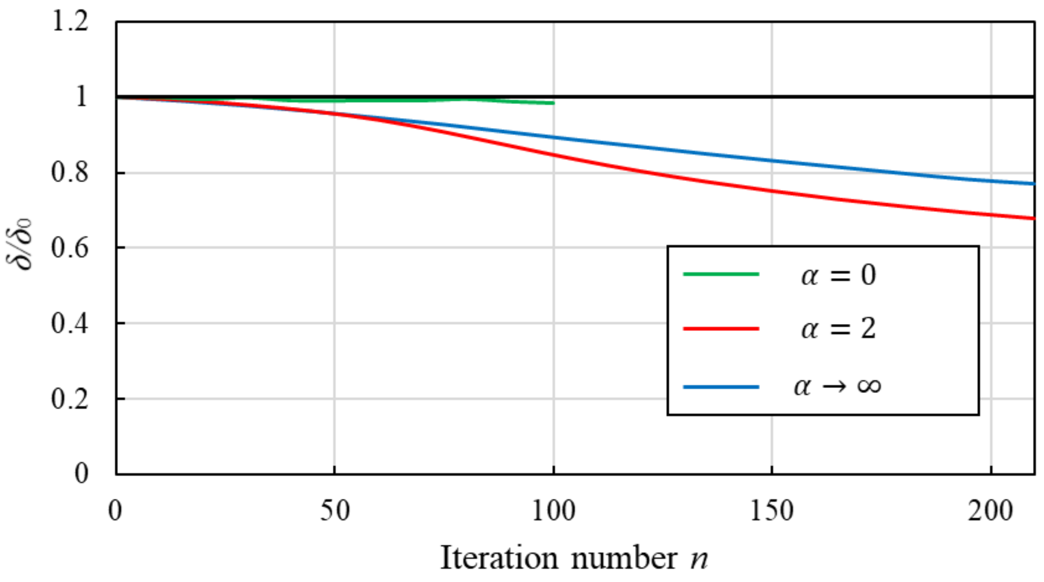

Fig. 3.10 The distance between the data points and the origin for the epoxy adhesive.

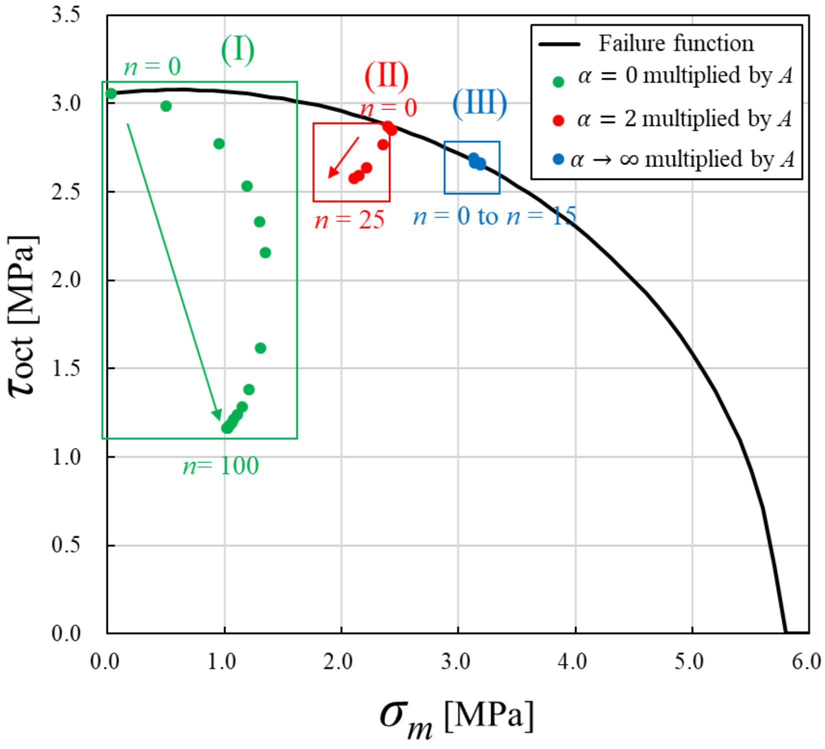

Fig. 3.11 The results of the optimization process on the failure function curve for the acrylic adhesive. The blue dots, red dots and green dots are the results for $\alpha = 0$, $\alpha = 2$ and $\alpha \to \infty$, respectively. n is the iteration number of the optimization.

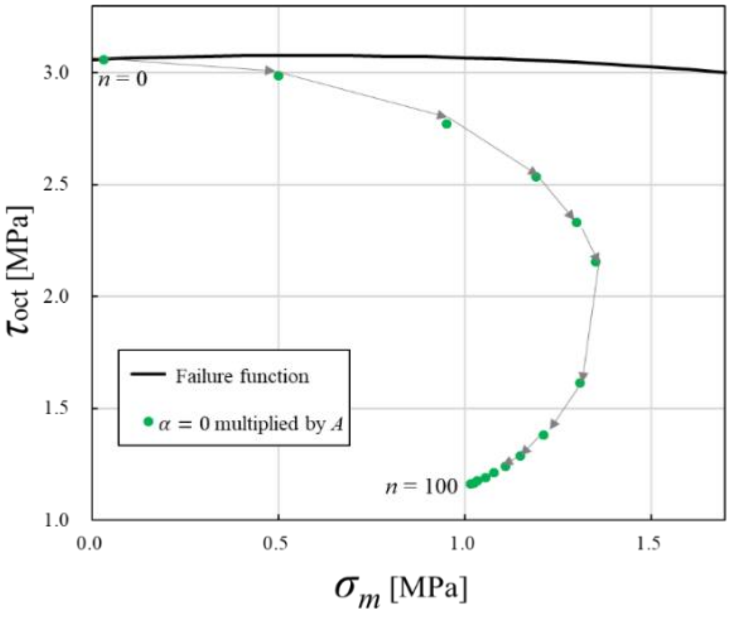

(a) Region (I) in Fig. 14

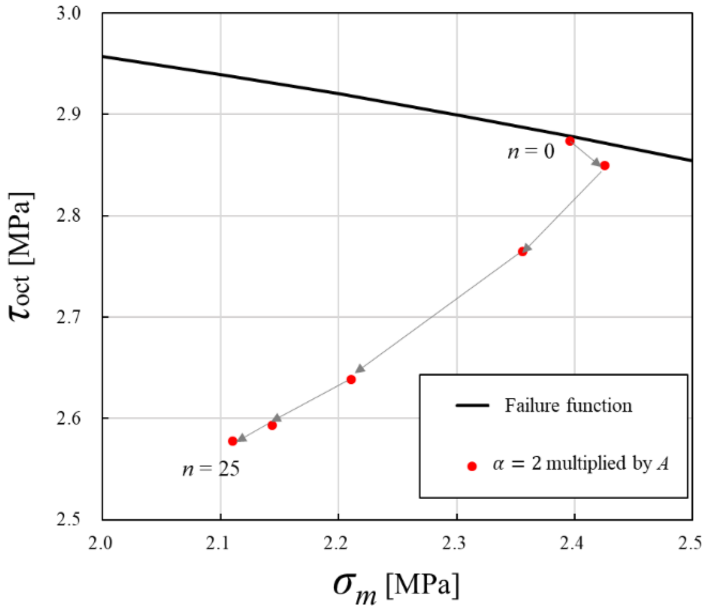

(b) Region (II) 9n Fig. 14

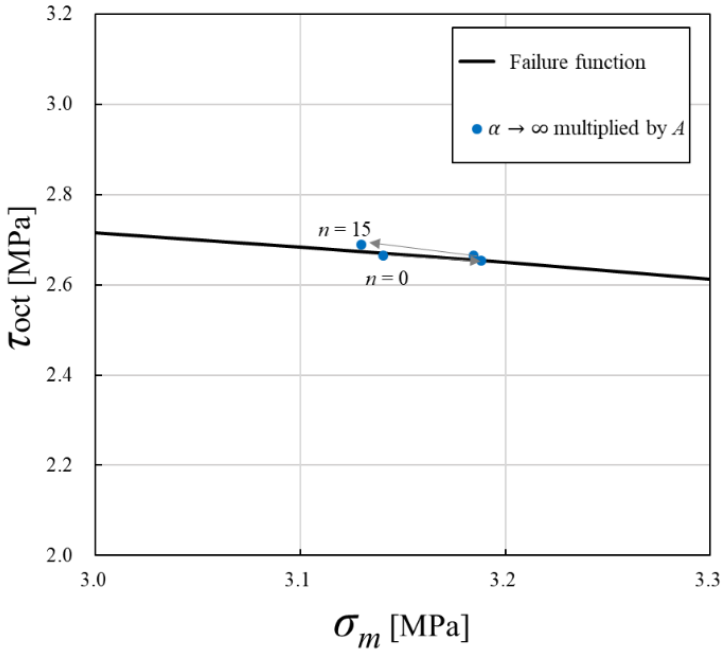

(c) Region (III) in Fig. 14

Fig. 3.12 The enlarged view of the optimization results of the acrylic adhesive multiplied by A. (I) $\alpha = 0$, (II) $\alpha = 2$ and (III) $\alpha \to \infty$.

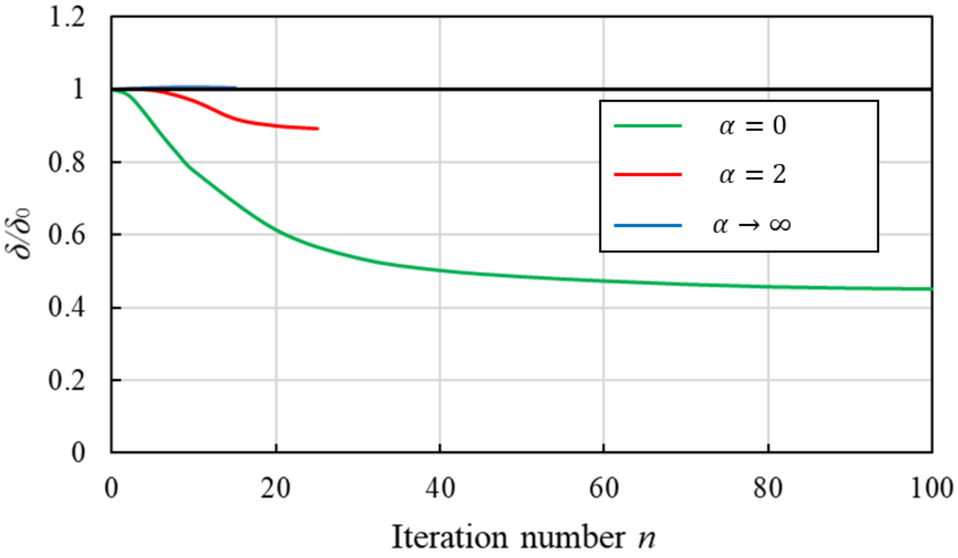

Fig. 3.13 The distance between the data points and the origin for the acrylic adhesive.

3.4.2. Shape gradient function and initial condition

Comparing the optimization process of epoxy and acrylic adhesives according to Figs. 3.9 and 3.12, the trends of the data points under loading conditions of $\alpha = 0$ and $\alpha \to \infty$ have the most obvious difference. Specifically, for $\alpha = 0$ (only torsion), the data points of epoxy adhesive stay at the original position while those of acrylic adhesive move through the optimization process. For $\alpha \to \infty$ (only tension), the results are totally opposite. The movement of the data points indicates the change of ratio between σ_m and τ_{oct} in the adhesive layer. As the loading applied to the model is kept constant, the ratio of σ_m to τ_{oct} observed in the adhesive layer can only be changed by the shape change of the adhesive layer. Looking back in Fig. 3.7, the shape of layer for the epoxy adhesive stays the original shape under $\alpha = 0$ and the shape of that for the acrylic adhesive keeps the original shape under $\alpha \to \infty$. Considering the reason for these optimized behaviors, the shape gradient function of Eq. (3.17), has been investigated. According to Eq. (3.17), l_G, which is calculated by the shape gradient function, indicates the change rate of the work done by the driving force on the adhesive interface which causes the shape change of the adhesive layer. The values of l_G through the first several steps of the optimization process for epoxy and acrylic adhesives are obtained, as shown in Fig. 3.14 for $\alpha = 0$ and Fig. 3.15 for $\alpha \to \infty$, respectively. The red line shows the result of epoxy adhesive and the blue line shows that of acrylic adhesive. For $\alpha = 0$, the value of shape gradient function for acrylic adhesive is positive so that the driving force causes the shape change along the positive direction and then the angle of the adhesive layer gets larger. However, for epoxy adhesive, the value of shape gradient function is negative so that this optimization is impossible. As a result, the shape of the adhesive layer only stays at the initial one. For $\alpha \to \infty$, the value of shape gradient function is positive for epoxy adhesive but negative for acrylic adhesive so that the shape change has an opposite pattern with that of $\alpha = 0$. This fact concludes that the initial shape for optimization is strongly affected to the final shape and the shape gradient function is the definite indicator wherever the present initial model is appropriate or not for the multi-material design.

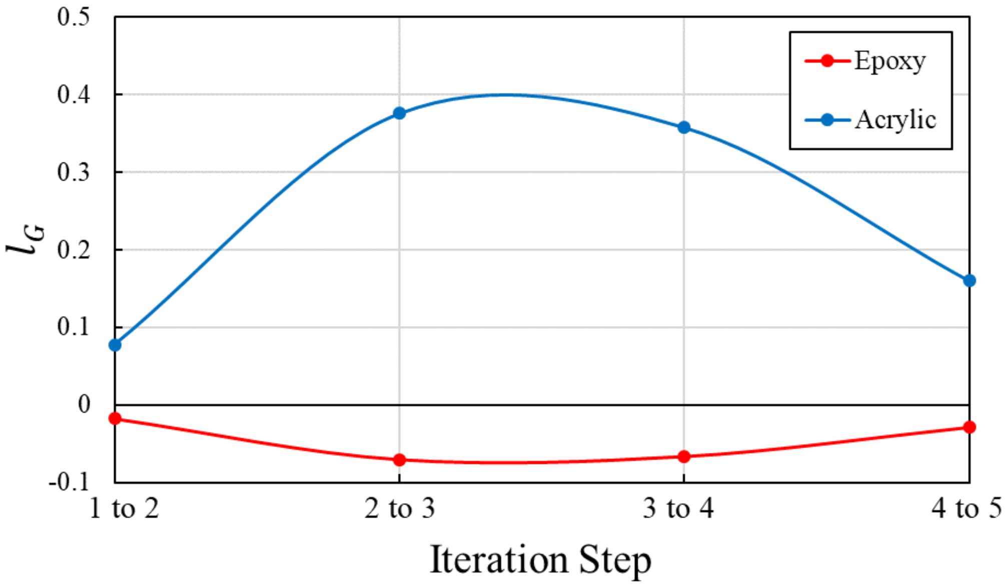

Fig 3.14 The shape gradient function of epoxy and acrylic adhesives for the first 5 steps of optimization under the loading condition $\alpha = 0$.

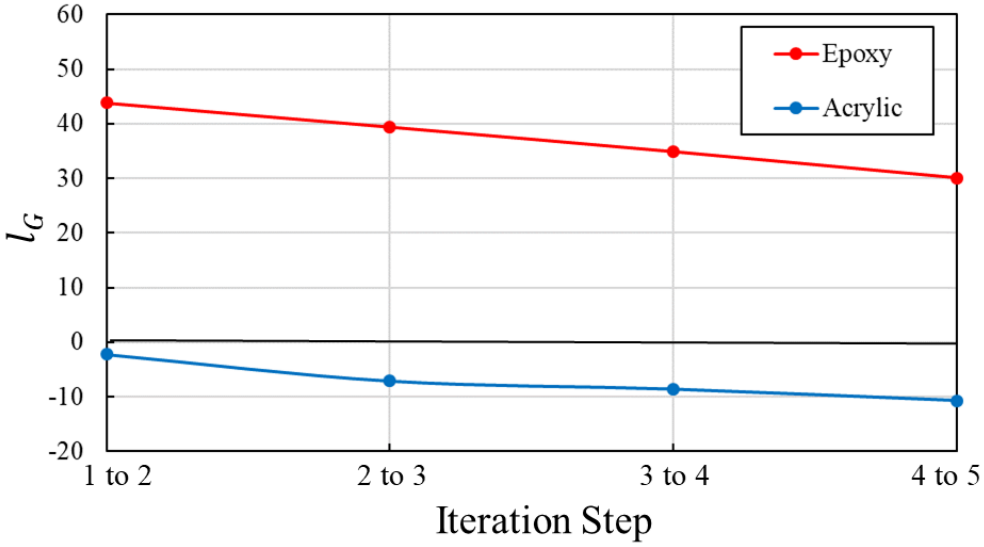

Fig. 3.15 The shape gradient function of epoxy and acrylic adhesives for the first 5 steps of optimization under the loading condition $\alpha \rightarrow \infty$.

3.5. Conclusion

To address the challenge of enhancing the strength of adhesive structures under multiaxial stress conditions, a shape optimization problem was formulated, taking into account the contrasting characteristics of failure functions for different adhesive materials. Throughout the optimization process for both adhesives, it is notable that the distances of the design data points from the origin within the failure plane defined by σ_m and τ_{oct} progressively diminish. This observation underscores the effectiveness of the optimization procedure in terms of objective function minimization.

Upon achieving optimal configurations, it was evident that the application of these refined shapes could lead to a notable reduction in applied stress levels. Specifically, for the epoxy adhesive, the optimized shape resulted in a stress reduction of approximately 30% compared to the initial configuration, while for acrylic, this reduction amounted to an impressive 50%. This outcome underscores the capacity of these final shapes to significantly enhance the mechanical integrity of the adhesive layer.

The driving force behind the geometric transformations of the adhesive layer is encapsulated by the shape gradient function. This function plays a pivotal role in governing the response of the adhesive layer under the influence of mean stress and shear stress. Notably, the shapes of the adhesive layers remain unaltered for the epoxy adhesive when $\alpha = 0$ and for the acrylic adhesive when α approaches infinity. This characteristic serves as a valuable indicator, shedding light on the suitability of the initial model for multi-material design endeavors.

4. Evaluation of Plastic Formability of Metal Laminates Bonded by Adhesives

The advantage of adhesive bonding lies in the lightweight nature of the adhesive materials, setting it apart from traditional mechanical fastenings. This attribute makes adhesive bonding an appealing choice for achieving cohesive bonds between dissimilar materials. Multi-material design is generally applied to the frame of structures where the strength of the bonded parts is crucial. In the automotive sector, a substantial utilization of metal laminates in body construction is evident. This practice not only facilitates diverse designs of automobile frames but also introduces the potential for significant weight reduction through the incorporation of metal laminates. To ascertain the viability of implementing multi-material configurations with laminates and to facilitate their integration into industrial production processes, a comprehensive evaluation of the plastic formability of bonded multi-material metal laminates is imperative.

Conical cup testing method, a comprehensive approach that amalgamates direct and composite assessment techniques to evaluate plastic formability, was employed in this research. The method employs a tapered die to induce a spectrum of deformations, including shrinkage flange deformation, elongation flange deformation, and rupture at the punch's base. This procedure serves to evaluate both the forming force and forming limits of metal laminates. The evaluation is carried out using a conical cup testing apparatus that has been developed based on the specifications outlined in JIS Z 2249, enhanced with upgraded observation features.

The investigation encompasses the evaluation of multi-layer specimens composed of aluminum and SPCC materials bonded by epoxy and acrylic adhesives. By comparing load-displacement relationships and post-testing specimen characteristics with those of single-layer specimens of varying thicknesses, fashioned from the same materials, the study assesses the formability of these multi-layer specimens. This comprehensive evaluation takes into account not only material properties but also the influence of structural factors, providing insights into the formability of multi-layer laminates.

4.1. Preparation of conical cup testing

4.1.1. Design of testing machine

A conical cup test apparatus was meticulously engineered in strict accordance with the specifications delineated in JIS Z 2249. The comprehensive design and assembly of this specialized equipment are visually presented in Fig. 4.1. The apparatus features a meticulously crafted spherical ball, boasting a diameter of 20.64 mm, which is diligently propelled by a cylindrical punch. The primary objective here is to apply precisely controlled axisymmetric pressure to the specimens, thereby inducing deformation within specially designed jigs. These specimens undergo the deformation process within conical dies, characterized by a 60-degree angle. Notably, the jigs are equipped with a central aperture at their base, measuring 24.4 mm in diameter.

In the initial design of the standard conical cup test, the examination of specimens was limited to post-testing observations, as the jig functioned as a self-contained system with the lower sections of the specimens remaining concealed. Recognizing the need for enhanced visibility, a novel see-through aperture was introduced. This enhanced design incorporates a mirror system within the lower section of the jig, as visually depicted in Figure 2. This ingenious addition facilitates a clear view of the lower aspects of the specimens, as exemplified in Fig. 4.2(a) and (b). To further augment the real-time observational capabilities, a camera, complemented by LED illumination, was integrated to capture dynamic alterations in the bottom view, as illustrated in Fig. 2(c).

Throughout the testing process, the punch was methodically set to operate at a controlled speed of 0.5 mm/min. Testing persisted until a noticeable reduction in the reaction load became evident, at which juncture the test was duly concluded.

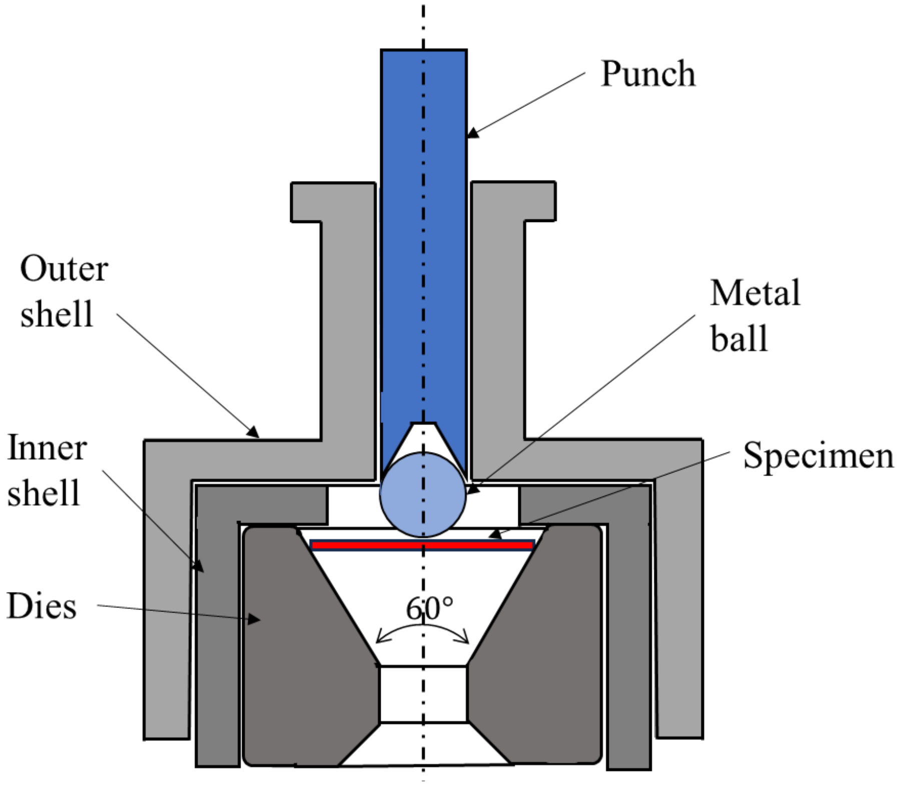

(a) Cross section of conical cup jigs

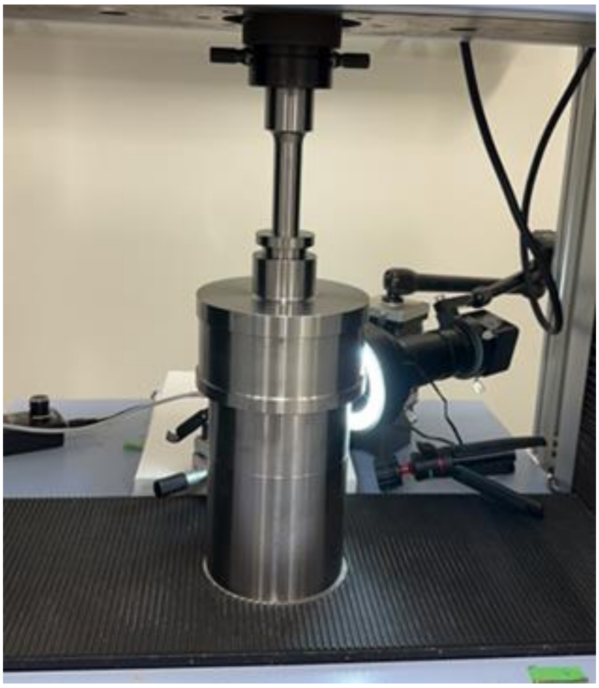

(b) All the parts equipped to tensile testing machine

Fig. 4.1 Conceptual diagram and assembled view of conical cup testing.

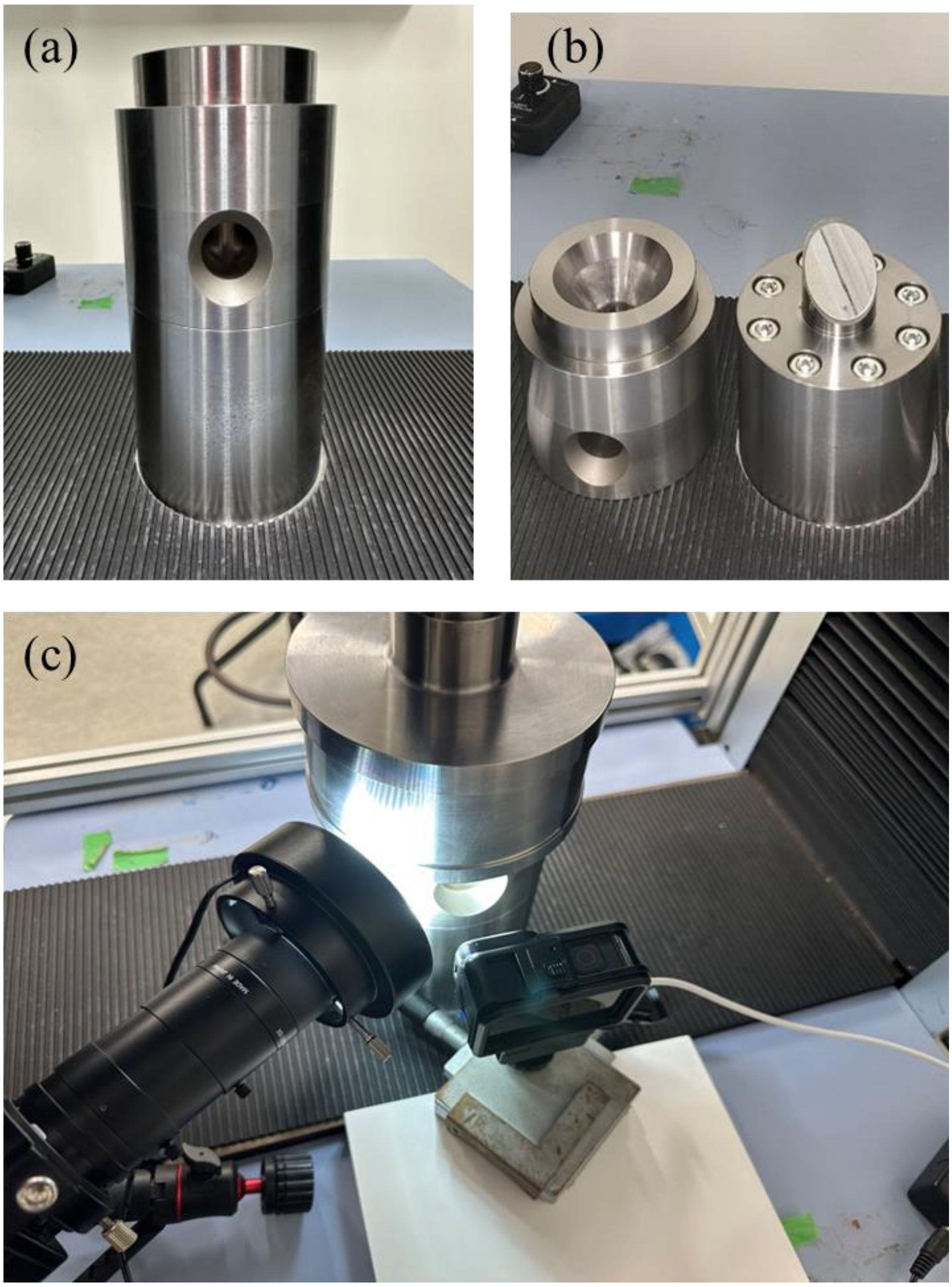

Fig. 4.2 Newly designed see-through aperture designed to observe specimens during the testing; (a) viewing port, (b) mirror inside the base jigs, and (c) recording system consisting of camera and LED.

4.1.2. Manufacturing process of specimens

The test specimens are circular sheets, each featuring a diameter of 50 mm. An integral component of evaluating the formability of both multi-layered and single-layered specimens bonded with adhesives involves a comprehensive comparative analysis with their unitary counterparts. This investigation is further designed to unravel the distinctive effects arising from varying materials and specimen thicknesses. The laminated metal sheets in this study were composed of A1050 (pure aluminum with a purity exceeding 99.50%), A5052 (an Al-Mg aluminum alloy with a magnesium content ranging from 0.5% to 5.6%), and SPCC (Steel Plate Cold Commercial with a carbon content not exceeding 0.15%). A detailed breakdown of the materials, adhesives, and thicknesses pertaining to the unitary specimen and layered specimens are presented in Table 4.1 and Table 4.2, respectively.

The manufacturing process for the layered specimens is listed as follow and visually delineated in Fig 4.3.

(a) This process commences with the uniform application of adhesives onto rectangular metal plates, measuring 220 mm x 120 mm, with meticulous attention to achieving uniformity and eliminating any visible air bubbles, as depicted in Fig 4.3(a).

(b) Acrylic adhesive (HardlocTM: M-600-08, Denka Co., Ltd.) was formulated by blending two distinct resins, while epoxy adhesive (EP-171, CEMEDINE Co., Ltd.) constituted a single-component resin. Subsequently, an identically sized metal plate is placed over the adhesive-coated surface, firmly secured using substantial steel plates and clamps, as exemplified in Fig. 4.3(b).

(c) In the case of acrylic-bonded specimens, complete curing was achieved within 20 minutes at room temperature. Conversely, specimens bonded with epoxy adhesive necessitated a heat treatment process at 130°C for a duration of 30 minutes, facilitated by a heating furnace, as illustrated in Fig. 4.3(c).

(d) Following the curing phase, any excess adhesive was meticulously removed, culminating in the fabrication of three circular specimens, each featuring a 50 mm diameter, via a punching operation, as portrayed in Fig 4.3(d).

It is worth noting that for the single-layered specimens of A5052 and SPCC, as well as the multi-layered specimens bonded with epoxy, the adhesive layers were delaminated during the punching operation as shown in Fig. 4.4. This occurred due to the limited ductility of epoxy adhesives in contrast to acrylic adhesives, resulting in the absence of a significant plastic as shown in Ch. 2. Consequently, epoxy-bonded specimens were more susceptible to shear forces during the punching manufacturing process, leading to delamination. Given this consideration, the subsequent testing and comparative analysis primarily relied on data obtained from specimens bonded with acrylic adhesives.

Table 4.1 Material and thickness of unitary specimens.

Type	Material	Thickness [mm]
Unitary	A1050	1.6
Unitary	A5052	0.6 1.2
Unitary	SPCC	0.6, 1.2

Table 4.2 Material and thickness of layered specimens.

Type	Material	Adhesive	Thickness [mm]
Single-layered	A1050&A1050	Epoxy	0.8+0.8+α
Single-layered	A5052&A5052	Acrylic	0.6+0.6+α
Single-layered	SPCC&SPCC	Acrylic	0.6+0.6+α
Multi-layered	A5052&SPCC	Acrylic	0.6+0.6+ α

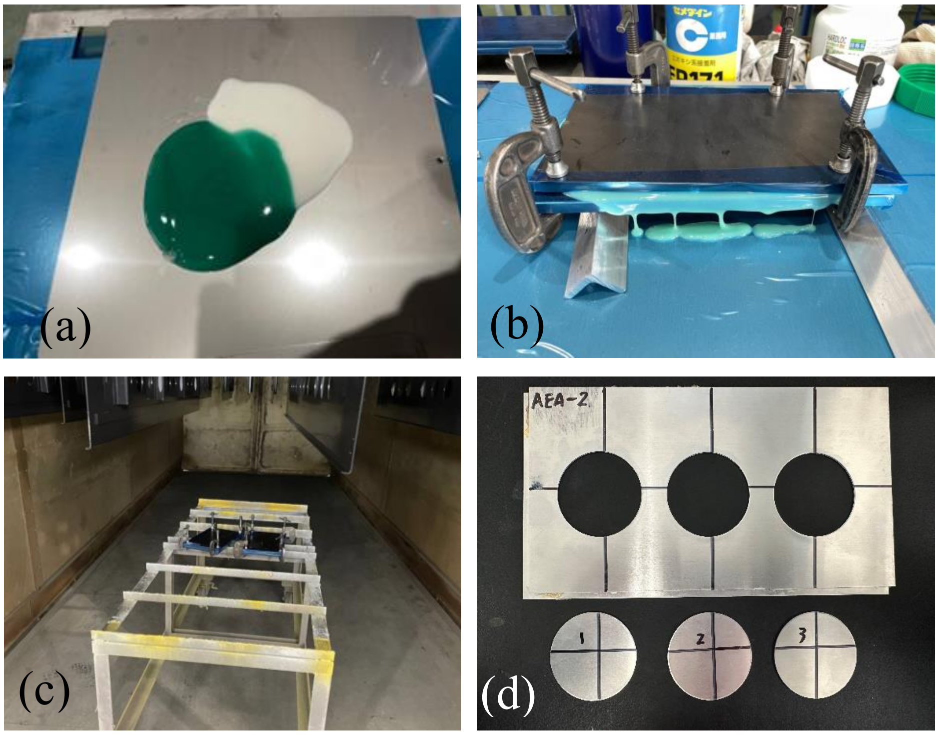

Fig. 4.3 Manufacturing process of bonded specimens; (a) pouring adhesives, (b) fixed by clamps and steel plates, (c) curing in the heating furnace, and (d) punched to circular plates.

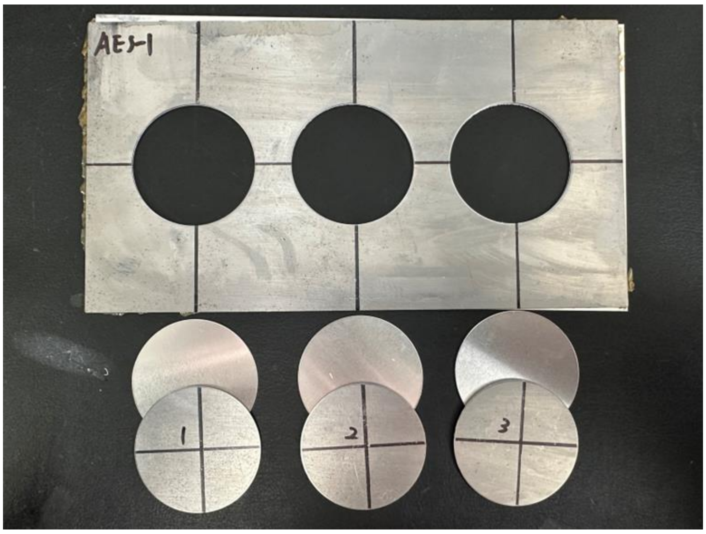

Fig. 4.4 Multi-layered specimens bonded by epoxy adhesives delaminated during the punching manufacturing process.

4.2. Testing results of conical cup testing

4.2.1. Load-displacement curves of unitary specimens

The unitary specimens, which were not layered with adhesive, were subjected to the initial testing procedures, serving as the fundamental benchmark dataset for subsequent evaluations encompassing both multi-layered and single-layered specimens. The prescribed test protocol involved the application of a controlled punch speed set at 0.5 mm/min, with the test concluding upon the distinct and sharp decline in load, signifying the point of failure.

The unitary specimen category encompassed three distinct types. These included pure aluminum (A1050) specimens with a thickness of 1.6 mm, aluminum alloy (A5052) specimens with thicknesses of 0.6 mm and 1.2 mm, and SPCC specimens with thicknesses of 0.6 mm and 1.2 mm. The load-displacement curves, derived from the outcomes of the testing of A1050 and A5052 specimens, are presented in Fig 4.5(a), while those pertaining to SPCC specimens are depicted in Fig. 4.5(b). Recall that the abbreviation of specimens in Fig. 4 denotes the kind of material, thickness and No. of test specimen such as “AL16-2” which is No.2 specimen of “AL”uminum (A1050 or A5052) with a 16 mm thickness. On these plots, the horizontal axis represents the stroke displacement, while the vertical axis signifies the load exerted by the punch. These load-displacement curves serve as pivotal indicators of the overall performance of the conical cup testing methodology.

The assessment of the testing process can be delineated into two distinctive phases. In the initial phase, spanning from 0 mm to approximately 15 mm, the metal sheet experiences elongation as the drawing forces progressively increase due to the punch, marking the initiation of plate deformation. Subsequently, in the second phase, commencing at approximately 15 mm, a notable transition unfolds. As the stroke reaches this pivotal point, the fundamental drawing force begins to decline, a consequence of the diminishing flange area. However, a noteworthy phenomenon occurs: as more material is drawn into the die cavity, the contact area between the shell and the die undergoes significant expansion. This amplified contact area gives rise to an augmented reaction force from the die, consequently heightening the frictional resistance to drawing and, in turn, amplifying the draw force. Consequently, the total force escalates rapidly as the stroke progresses, culminating in its ultimate value upon the completion of drawing, immediately preceding the failure event marked by a sharp and abrupt decline in punch forces.

This discernible behavior in conical cup testing, characterized by two distinct phases, is a recurring pattern. However, it is essential to note that the specific transition point within these phases may exhibit variations contingent upon the materials and thicknesses being considered.

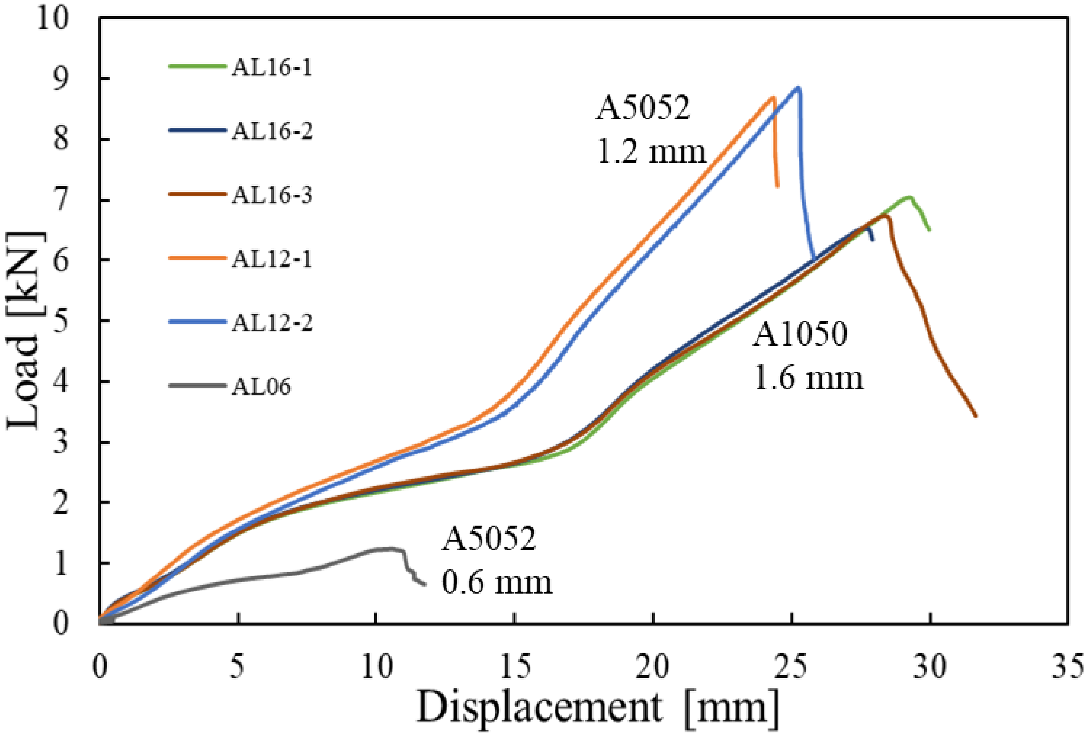

(a)

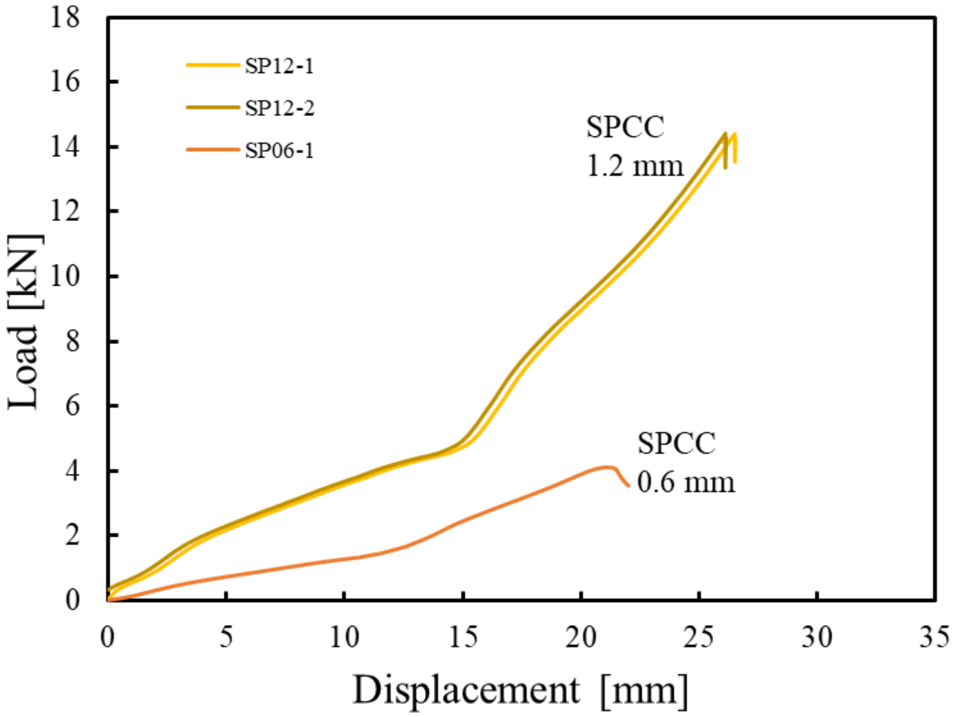

(b)

Fig. 4.5 Load-displacement curves of unitary specimens with different thickness; (a) A1050 and A5052, (b) SPCC.

4.2.2. Load-displacement curves of single material-layered specimens

Single (material)-layered specimens, comprising pure aluminum (A1050), aluminum alloy (A5052), or SPCC, were subjected to testing, and their resulting data were meticulously collected. These specimens encompassed pure aluminum (A1050) bonded with epoxy adhesive, featuring a thickness of 1.6 mm in addition to the adhesive layer thickness as indicated in Table 4.2. Similarly, aluminum alloy (A5052) specimens were adhered using acrylic adhesive, boasting a thickness of 1.2 mm plus the adhesive layer thickness. Additionally, SPCC specimens were bonded with acrylic adhesives and possessed a thickness of 1.2 mm, inclusive of the adhesive layer thickness.

The load-displacement curves stemming from the testing data for A1050 are visually presented in Fig 4.6(a), while the curves for A5052 are illustrated in Fig 4.6(b), and those pertaining to SPCC specimens are exhibited in Fig 4.6(c). Recall that the abbreviation of specimens in Fig. 5 denotes the kinds of material and adhesive, and No. of test specimen such as “AEA-4” which is No.4 specimen of “A”luminum (A1050 or A5052) bonded with “E”poxy adhesive and “SAS-3” No.3 specimen of “S”teel (SPCC) bonded with “A”crylic adhesive. In these figures, the horizontal axis denotes strokes, whereas the vertical axis signifies the load applied by the punch. As expounded in Section 3.1, the outcomes align with the typical behavior observed in conical cup testing. Initially, the reaction forces exhibit a gentle increase, subsequently transitioning into a rapid ascent after reaching the 15 mm mark.

The dataset comprises five A1050 samples showcased in Fig. 4.6(a), three A5052 specimens displayed in Fig 4.6(b), and an additional three SPCC samples depicted in Fig. 4.6(c). Notably, samples of the same material consistently exhibit remarkably consistent performance. Although the failure points exhibit variations due to disparities in adhesive conditions and the manufacturing process, they consistently cluster within proximity, differing by less than 10%. Consequently, it is evident that the specimens exhibit trustworthy reproducibility, with the single SPCC-layered specimens particularly demonstrating high reliability. It is worth mentioning that the load drops differ between aluminum and SPCC, with the former exhibiting a sharp drop, and the latter displaying a milder descent. This disparity may be linked to the development of surface roughness characteristics and subsequent plastic instability in thickness. The former experiences a rapid strain gradient and strain concentration, swiftly reaching the final failure point immediately after the maximum point.

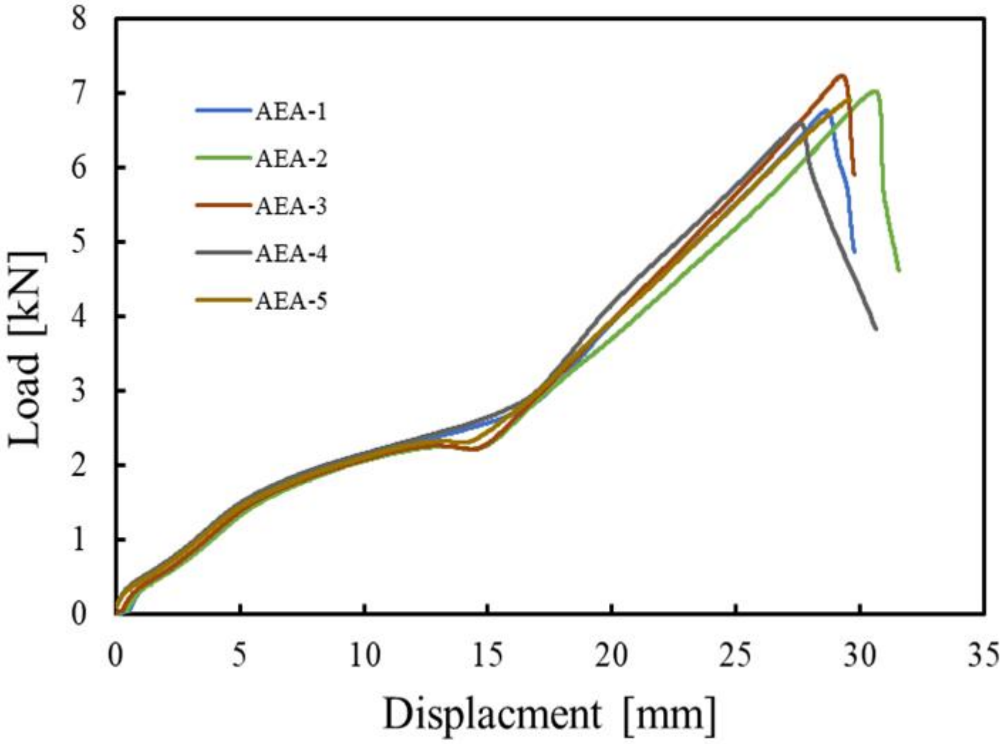

AEA-1
AEA-2
AEA-3
AEA-4
AEA-5
Load [kN]
Displacment [mm]
0
1
2
3
4
5
6
7
8
0
5
10
15
20
25
30
35

(a)

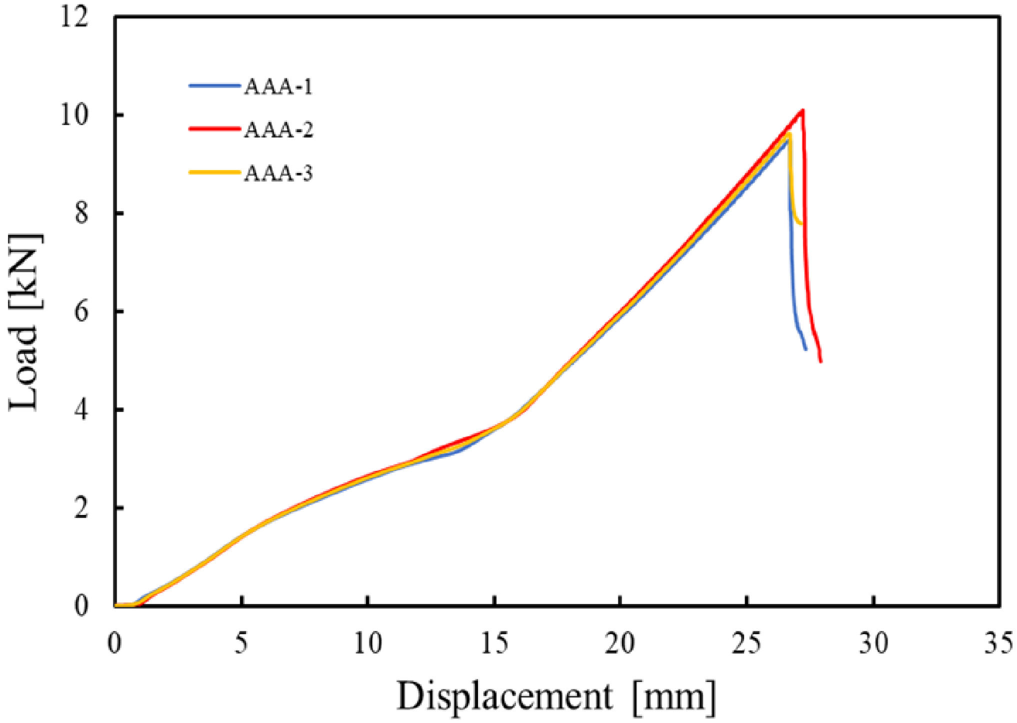

AAA-1
AAA-2
AAA-3
Load [kN]
Displacement [mm]
0
2
4
6
8
10
12
0
5
10
15
20
25
30
35

(b)

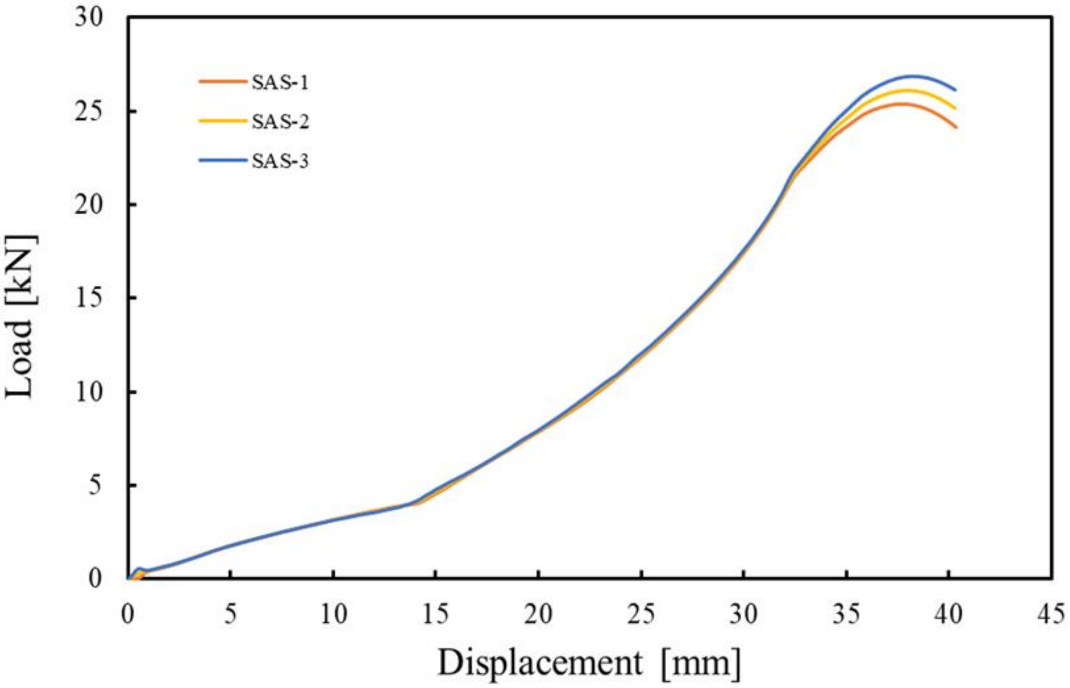

(c)

Fig. 4.6 Load-displacement curves of single material-layered specimens; (a) A1050 bonded by epoxy, (b) A5052 bonded by acrylic and (c) SPCC bonded by acrylic.

4.2.3. Load-displacement curves of multi materials-layered specimens

Multi (materials)-layered specimens, comprising aluminum alloy (A5052) and SPCC, were subjected to testing, which data were meticulously collected. These specimens were securely bonded using acrylic adhesive, with a uniform thickness of 1.2 mm (0.6 mm + 0.6 mm) plus the adhesive thickness (see Table 1). Four samples were subjected to testing, with three of them arranged such that the Al face was oriented upward (denoting as AAS-1 to AAS-3 in Fig. 4.8), while the fourth had the SPCC face positioned upward (denoting as SAA-1 in Fig. 4.8), as visually represented in Figs. 4.7 (a) and (b).

The ensuing load-displacement curves are illustrated in Fig. 4.8. The captions of both axes are the same as the previous. Consistent with Sec. 4.2.2, the results align closely with the typical characteristics of conical cup testing for both materials, as shown in Fig.

5. Initially, the reaction forces exhibit a gentle increase, followed by a notable acceleration after reaching the 15 mm threshold. Until this stage, the behavior is governed by that of SPCC because it is close to that in Fig. 4.6(c). However, the final rupture feature of sudden drop in load is similar to that of Al in Figs. 4.6 (a) and (b). Therefore, the process of deformation is dependent on the material with higher stiffness (SPCC in this case) and the final fracture dominantly happens in material side with the larger surface roughness which might induce the localized necking (Al in this case).

It is notable that the performance of the two testing orientations, with either the Al face or the SPCC face oriented upward, demonstrates remarkable similarity. This observation suggests that the orientation of the multi-material configuration has minimal influence on the formability of the multi-layered metal sheet. Furthermore, the congruence observed across the four curves underscores the reproducibility and reliability of the testing procedure.

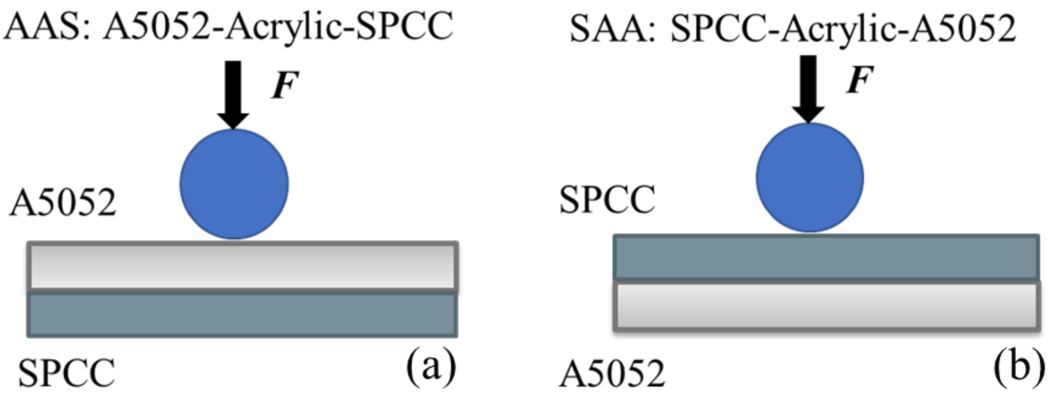

Fig. 4.7 The orientation of multi-material specimens (a) A5052 over SPCC, (b) SPCC over A5052.

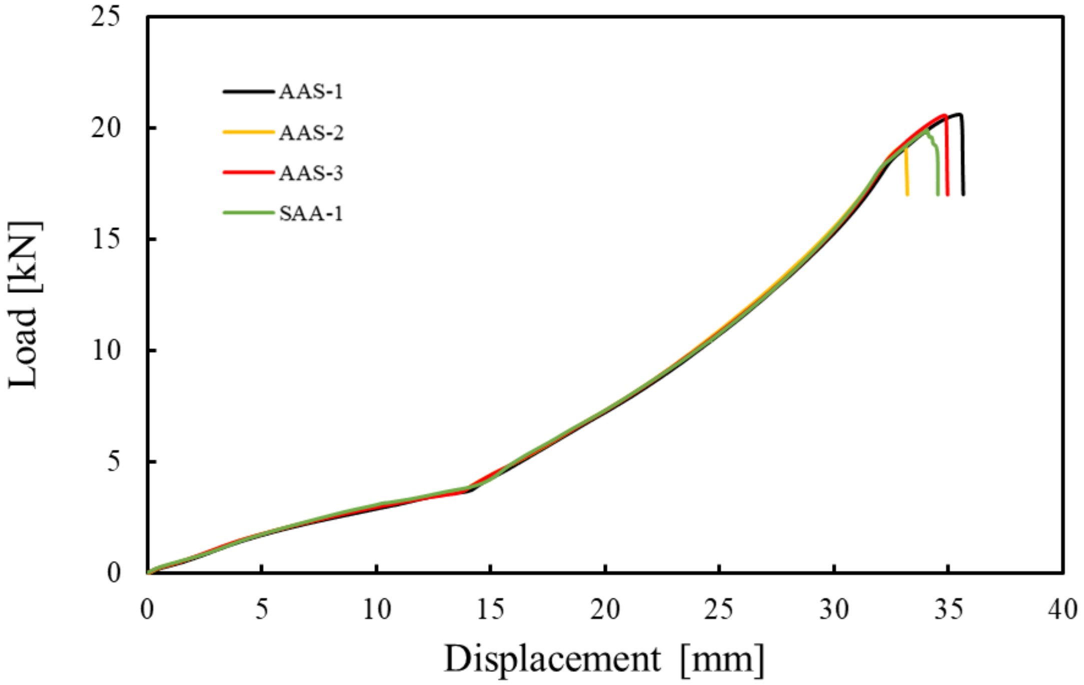

Fig 4.8 Load-displacement curves of single material-layered specimens; AAS-1 to AAS-2 representing Al face-up and SAA-1 representing SPCC face-up.

4.3. Considerations and discussions

4.3.1. Post-testing specimens and C.C.V.

In Fig. 4.9, we present typical visual post-testing representations with the Conical Cup Value (C.C.V.) [97] averaged using all the corresponding samples in Table 4.3, which is calculated as the average of the maximum and minimum outer edge diameters of specimens:

$$\mathrm{C.C.V.} = \frac{D_{max} + D_{min}}{2}. \tag{4.1}$$

In the context of unitary plates, it is notable that the C.C.V. tends to be more substantial for thinner plates, particularly those with a thickness of 0.6 mm. This observed trend is indicative of the diminished formability associated with these specimens, which becomes evident when analyzing the load-displacement curves illustrated in Fig. 4.5. For single aluminum-layered specimens, both A1050 and A5052, the C.C.V. values are quite similar to those of the unitary plates with the same thickness, reflecting a similar level of formability. However, in the case of single-layered SPCC specimens, the C.C.V. is notably smaller than that of the unitary plates, indicating a lower level of plastic formability. This discrepancy suggests that SPCC is less formable in comparison to aluminum when it comes to single-layered configurations.

In contrast, for the multi-layered specimens composed of A5052 and SPCC (or SPCC and A5052), the C.C.V. represents an intermediate value when compared to single-layered plates made from the same materials and featuring identical thicknesses. This observation suggests that the combination of materials and layering does not significantly alter the formability compared to single-layered configurations with the same materials and thickness.

Furthermore, it is important to highlight that discernible instances of local buckling are observable in the outer edges of plates with smaller thickness, particularly in the unitary plates. However, such phenomena are absent in thicker plates and those that have been adhesively bonded. This local asymmetrical deformation in the thinner unitary plates leads to structural instability during the testing process, which is not observed in thicker plates and multi-material layered specimens.

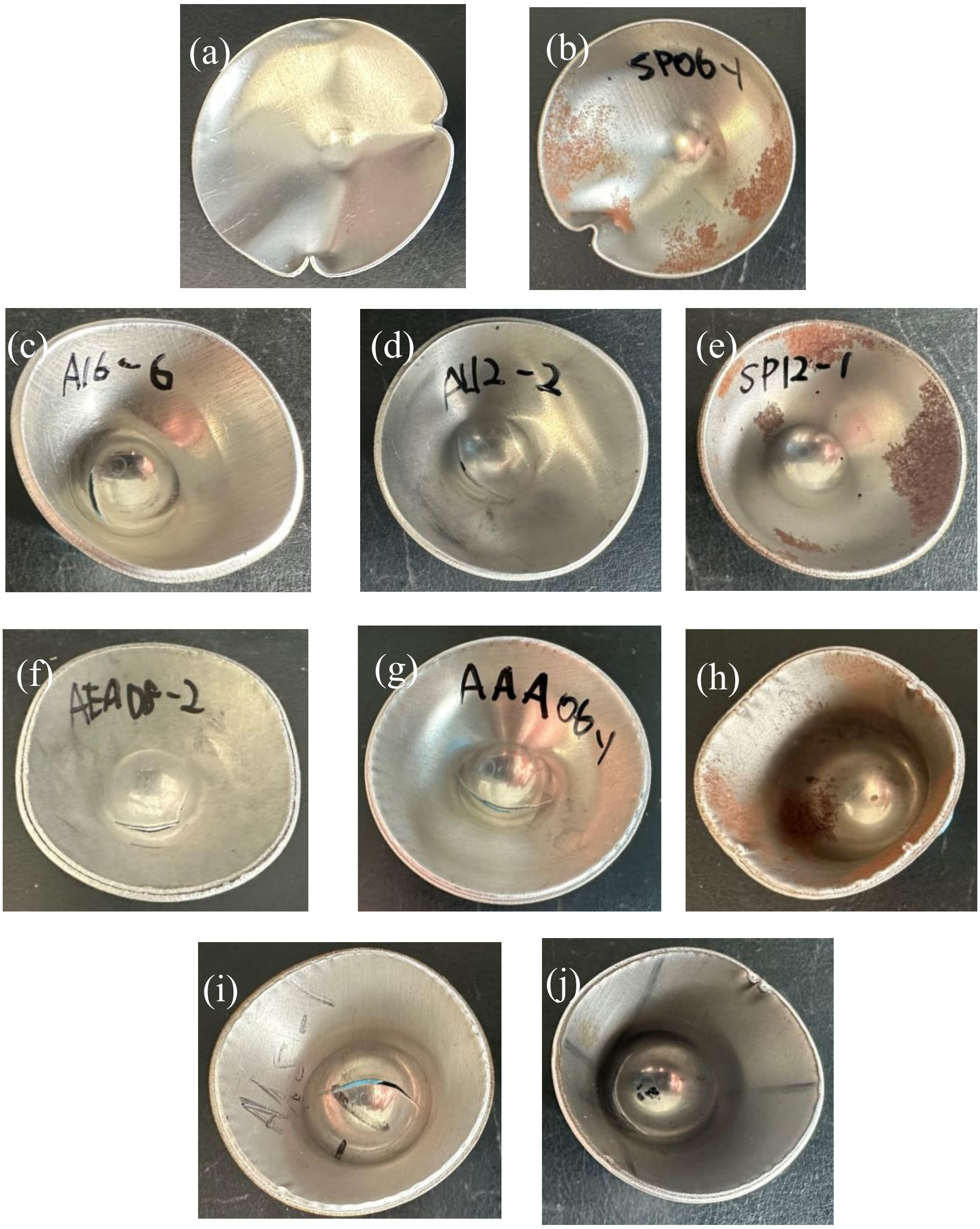

Fig. 4.9 Post-testing specimens of all types with details shown in Table 2. (a) to (e) Unitary, (f) to (h) single-layered and (i) to (j) Multi-layered specimens.

Table 4.3 Average Conical Cup Value (C.C.V.) for all types of specimens.

Specimens No.	Specimens type (thickness [mm])	C.C.V [mm]
a	Unitary A5052 (0.6)	45.8
b	Unitary SPCC (0.6)	42.1
c	Unitary A1050 (1.6)	39.6
d	Unitary A5052 (1.2)	41.2
e	Unitary SPCC (1.2)	40.1
f	Single-layered A1050 (0.8 + 0.8)	39.8
g	Single-layered A5052 (0.6 + 0.6)	41.0
h	Single-layered SPCC (0.6 + 0.6)	33.5
i	Multi-layered A5052-SPCC (0.6 +0 .6)	37.3
j	Multi-layered SPCC-A5052 (0.6 +0 .6)	37.3

4.3.2. Specimens during the testing process

As illustrated in Fig. 4.5(a) and Fig. 4.9(a), the unitary aluminum plates with a thickness of 0.6 mm exhibit structural instability at approximately 12 mm of stroke during testing. However, when these same 0.6 mm aluminum plates are effectively bonded with adhesive (as single A5052-layered specimens), they remain stable at the 12 mm stroke, as depicted in Fig. 4.6(b) and Fig. 4.9(g). Remarkably, they are capable of achieving a fracture point equivalent to that of thicker unitary plates in Fig. 4.5(a).

To investigate the root cause of this phenomenon, we selected four types of samples for further examination. These included unitary A5052 specimens with thicknesses of 0.6 mm and 1.2 mm, a single A5052-layered specimen with a thickness of 1.2 mm (comprising two 0.6 mm layers bonded together with adhesive), and another single A5052-layered specimen without any adhesive, effectively representing two simply stacked single-layered specimens. Testing was carried out, and the specimens were extracted from the jigs when the stroke reached 12 mm.

Visual inspection of the specimens at this 12 mm stroke juncture provided valuable insights. For the unitary specimens with 0.6 mm (Fig. 4.10(a)) and the single-layered specimens simply stacked without any adhesive (Fig. 4.10(b)), evident signs of asymmetrical deformation patterns and local buckling were observed at an early stage. In contrast, the single-layered bonded specimens (Fig. 4.10(c)) displayed symmetrical deformation without any indications of local buckling. This behavior closely resembled that of the unitary specimen with a thickness of 1.2 mm (Fig. 4.10(d)). Consequently, it can be inferred that the adhesive layer serves to enhance the stability of bonded thin plates, preventing asymmetrical deformation and averting local buckling. This transformation effectively enables the two bonded plates to function cohesively as a single thicker plate, thus contributing to the observed structural stability.

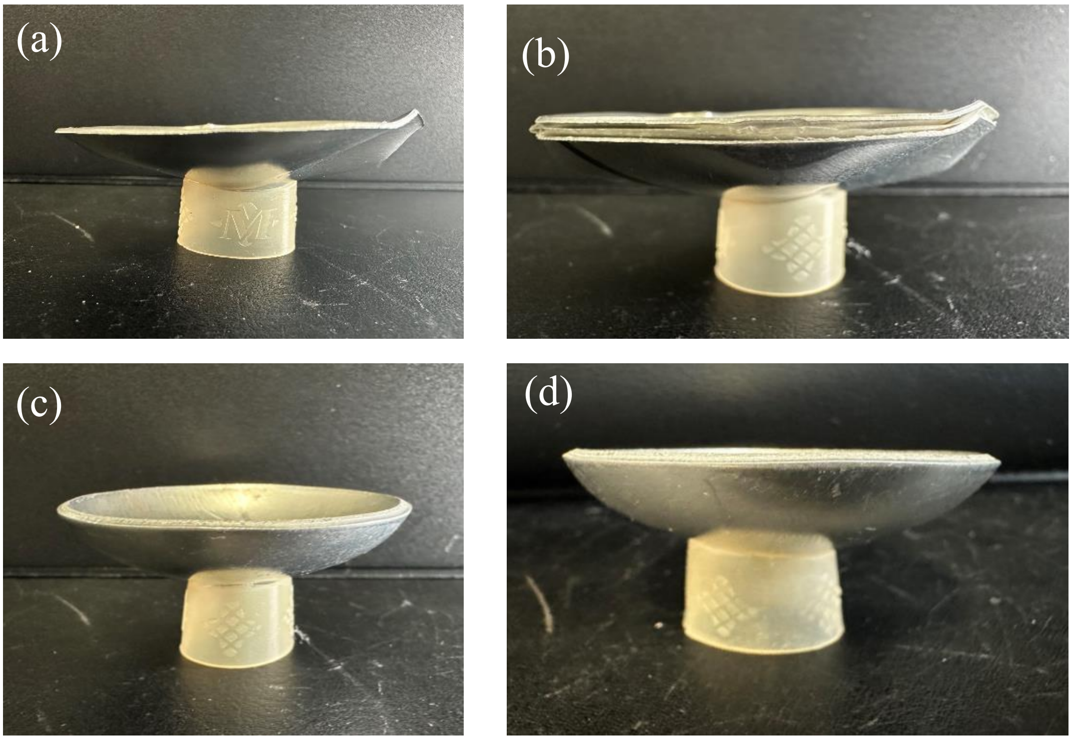

Fig. 4.10 Specimens during the testing at 12 mm stroke; (a) unitary Al plate with thickness of 0.6 mm, (b) Simply stacked two Al plates (0.6 mm, 0.6 mm), (c) single A5052-layered plate bonded by acrylic adhesive (0.6 + 0.6 mm), and (d) unitary Al. plate with thickness of 1.2 mm.

4.3.3. See-through aperture for in-situ observation

As elucidated in Section 4.1.1, conventional enclosures in the experimental setup cannot directly observe the evolving states of the specimens during testing. However, gaining insights into the behavior of specimens, particularly in their final stages of testing, is pivotal for a comprehensive understanding of their exact forming limit. To address this issue, a purposefully designed veining port featuring a mirror system was meticulously developed to facilitate the observation of the bottom of the specimens, as showcased in Fig. 4.11.

The results presented in Section 3 underscore the shared characteristics of conical cup testing across various specimen types. In this context, we provide an illustrative example of observation findings from single A5052-layered specimen (denoting as AAA-2 in Fig. 5(b)), which are correlated with corresponding points on the load-displacement curves (Fig. 4.12).

Let ΔD be the distance between the instant stroke and the load dropping stroke as:

$$\Delta D = D_{instant} - D_{dropping}. \tag{4.2}$$

Notably, at a juncture situated approximately 0.1 mm, several snapshots just before and after the point of load drop in the load-displacement curve, ranging from -0.1 to 0.1 mm, are taken in Fig. 4.12. And a conspicuous localized necking manifests along the circumferential direction around the central bottom of the specimens. This necking along thickness exhibits rapid growth, as depicted in Fig. 4.12 (a) to (b). Subsequently, it transforms into a fracture in close proximity to the load-drop points, as illustrated in Fig. 4.12 (c). The fracture expands outward, coinciding with a rapid reduction in load as shown in Fig. 4.12 (d) to (e). Based on these observations, it is apparent that the discernible necking happens nearly close to the load peek in the curves. Even if the forming limit estimated from the load-displacement curves, the error is negligibly small.

Images of other types of specimens (multi-layered and unitary specimens) at the same stage (ΔD ranging from -0.1 to 0.1) are presented in Figure 4.13. It is evident that specimens of different types at the same stage share similar characteristics in terms of the fracture growth process. Necking occurs and progresses close to the points where the load starts to drop, and it grows rapidly, nearly simultaneously with the reduction in load. This observation underscores the functionality of the see-through aperture in allowing for the in-situ observation of specimen behavior.

While in this study, the growth of necking and fracture aligns closely with the load drop, it is plausible that in other cases, the behavior of necking growth might precede or follow the load drop points. Therefore, the see-through aperture serves as a valuable tool for researchers, facilitating a better understanding of the precise timing and characteristics of necking and fracture in various scenarios.

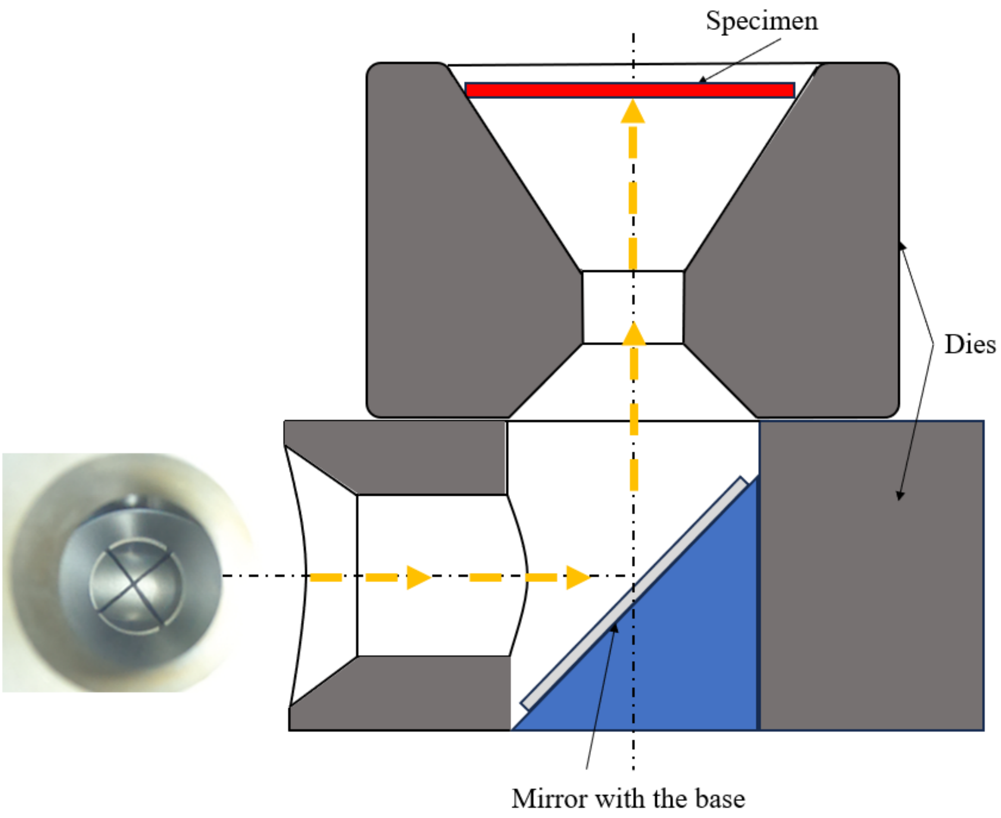

Fig. 4.11 Conceptual diagram of the see-through aperture and the example image observed from the viewing port.

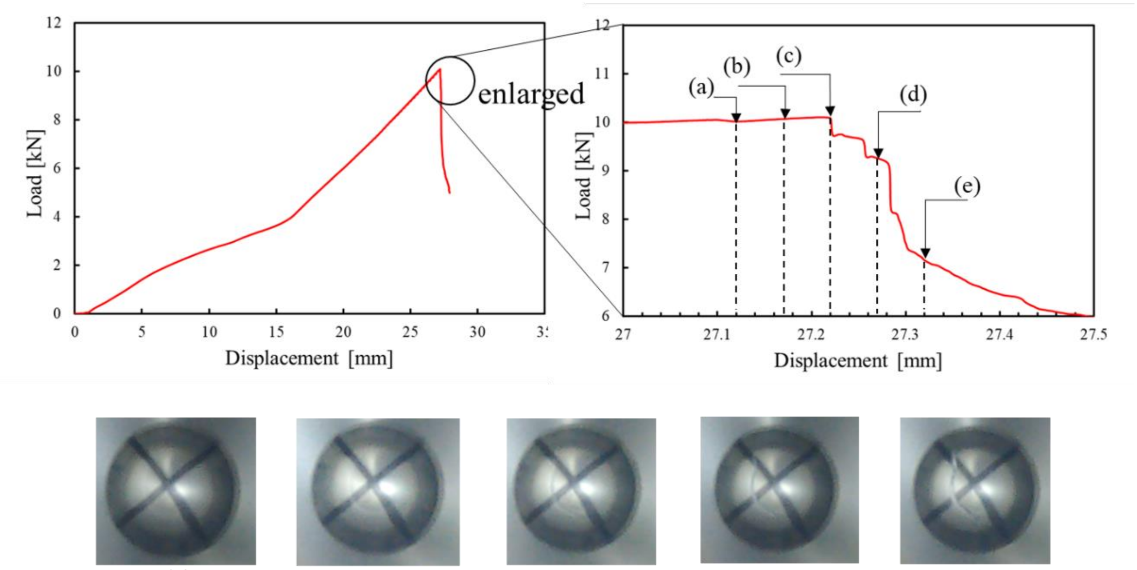

(a) $\Delta D = -0.1$ mm
(b) $\Delta D = -0.05$ mm
(c) $\Delta D = 0$ mm
(d) $\Delta D = 0.05$ mm
(e) $\Delta D = 0.1$ mm

Fig. 4.12 Different stages of specimens observed from the see-through aperture during juncture situated approximately 0.1 mm before and after the point of load drop with the corresponding points in load-displacement curve.

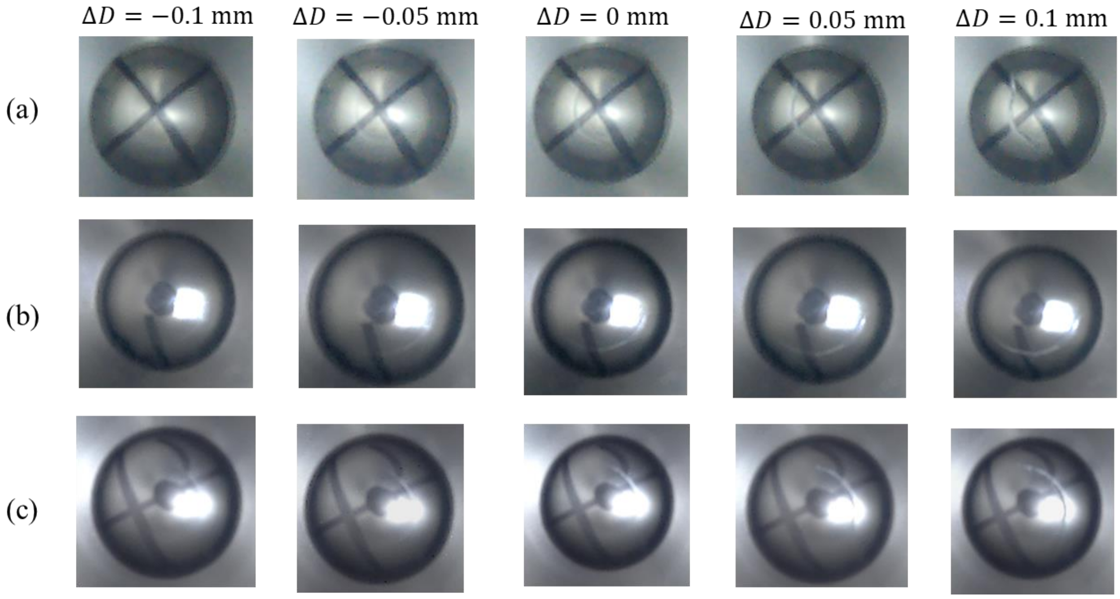

Fig. 4.13 Different types of specimens observed from the see-through aperture at the same stage of ΔD ranging from -0.1 to 0.1. (a) single-layered A5052 specimen, (b) multi-layered A5052-SPCC specimen and (c) unitary A5052 specimen.

4.3.4. Comparison among different types of specimens

Figure 4.14 provides an insightful comparison between single (material)-layered specimens and their unitary counterparts. It is worth noting that the data in Fig. 9 suggests that the adhesive's influence enables a material with half the plate thickness to exhibit equivalent or even superior plastic formability in comparison to a material with twice the plate thickness. As discussed in Section 4.3.2, the layered material by the adhesive appears to play a pivotal role in enhancing the stability of bonded thin plates, ensuring more uniform deformation while inhibiting local buckling. Consequently, this augmentation of formability effectively elevates the half-thickness plates to a level of performance comparable to that of a material with double the thickness, particularly in the context of aluminum. For SAS (single SPCC-layered specimen bonded by acrylic adhesive) in Fig. 4.14, a substantial increase in forming limits for 40% is discernible, underscoring the formability enhancements enabled by the adhesive. This observation highlights the critical role played by the properties of the parent material in determining the efficacy of adhesive interventions.

The outcomes from multi-layered specimens are then compared with those of unitary and single-layered specimens, as illustrated in Fig. 4.15. Strikingly, the multi-layered specimen (AAS; “A”luminum alloy 5052 and “S”PCC bonded by “A”crylic adhesive) exhibits a significantly expanded forming limit, marked by an approximate 40% increase when contrasted with the unitary A5052 (denoting as AL12 in Fig. 4.15), and by 35% increase when done with the unitary SPCC (SP12). This remarkable enhancement in formability can be attributed to the adhesive's capacity to augment stability, as discussed in Section 4.3.2. In comparison to the single SPCC-layered specimen (SAS), it's evident that the form limiting has a slight decrease with a remarkable reduction of weight. Specifically, there's only a mere 5% reduction in the forming limit. This signifies commendable performance, especially when considering that the total weight of the structure experiences a reduction of approximately 33% compared with unitary (SP12) and single-layered specimens (SAS). Conversely, when compared to the unitary (AL12) and single A5052-layered specimen (AAA), the multi-material specimen (AAS) showcases a substantial improvement that the forming limit increases a commendable 40% expansion. The results discussed in this section underscore the positive influence of bonded multi-layer structures on enhancing the formability of single-layered specimens.

In reference to Fig. 4.14, it is also noteworthy that the forming limits observed in the cases of single A1050-layered specimens bonded by epoxy adhesive (AEA) and single A5052-layered specimens bonded by acrylic adhesive (AAA) closely align with those of unitary specimens (AL12 and AL16), respectively, which are composed of identical materials and maintains a consistent total thickness. Conversely, the forming limit for SPCC exhibits a big improvement, as it can accommodate larger deformations with longer strokes in comparison to its unitary counterpart (SP12 and SAS). To elucidate the rationale behind this phenomenon, it is imperative to consider the contribution of the adhesive to the growth of surface roughness of metals, as schematically shown in Figs. 4.16 and 4.17.

During the plastic deformation of plate, the microscopic surface roughness is, generally, linked mainly to the rotation of crystalline grains faced to the surface due to the less constraint. The abrupt localized growth of surface roughness leads the local necking in the plate thickness direction, which can be recognized as the forming limit. Consequently, the delay in localization due to some constraint facilitates uniform deformation and increases the plastic formability [110], [111]. If the surface roughness in SPCC could be smaller than that of aluminum under the same loading state, the forming limits are expanded due to the adhered effect, as shown in Fig. 4.16. Conversely, for aluminum as shown in Fig. 4.17, the surface exhibits larger roughness than SPCC [112], probably resulting in interface local delamination between the adhesive layer and the surface of adhered metal during deformation and inducing the earlier necking. However, it should be noted that the layered material with two unitary ones with half thickness guarantees the same performance as the unitary material with double thickness due to the adhered effect, as shown in Fig. 4.14.

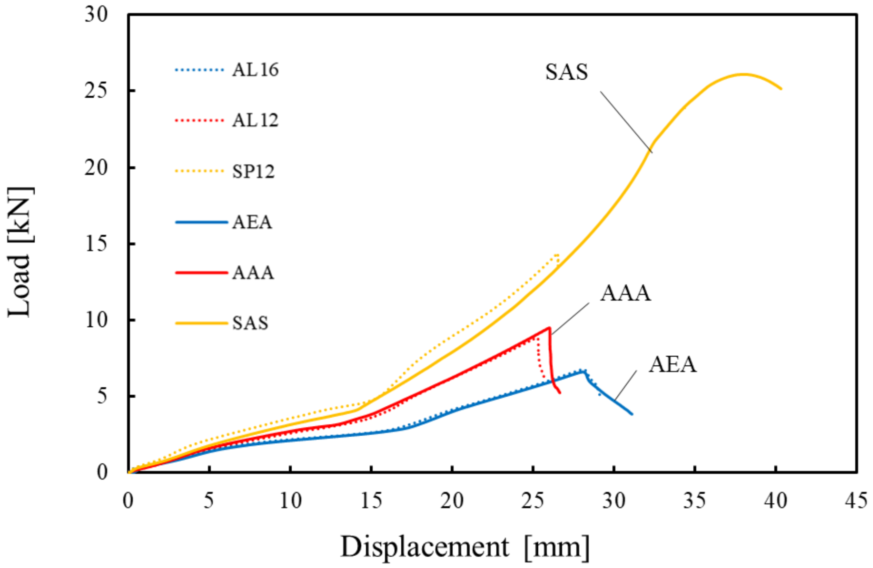

Fig. 4.14 Comparison between single-layered specimens of A1050 (denoting as AEA), A5052 (AAA) and SPCC (SAS) and their unitary counterparts with the same thickness (AL16, AL12 and SP12).

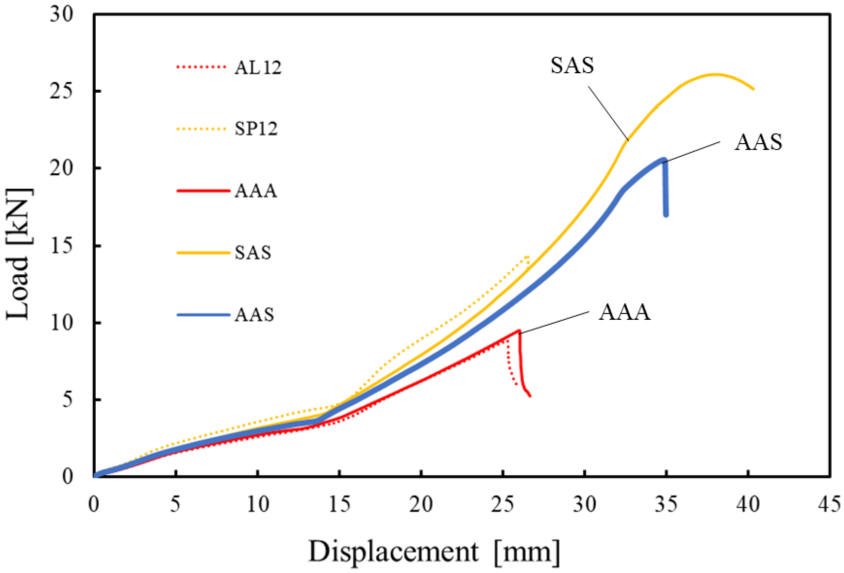

Fig. 4.15 Comparison between multi-layered specimens (AAS) and single-layered (AAA and SAS) as well as unitary specimens (AL12 and SP12).

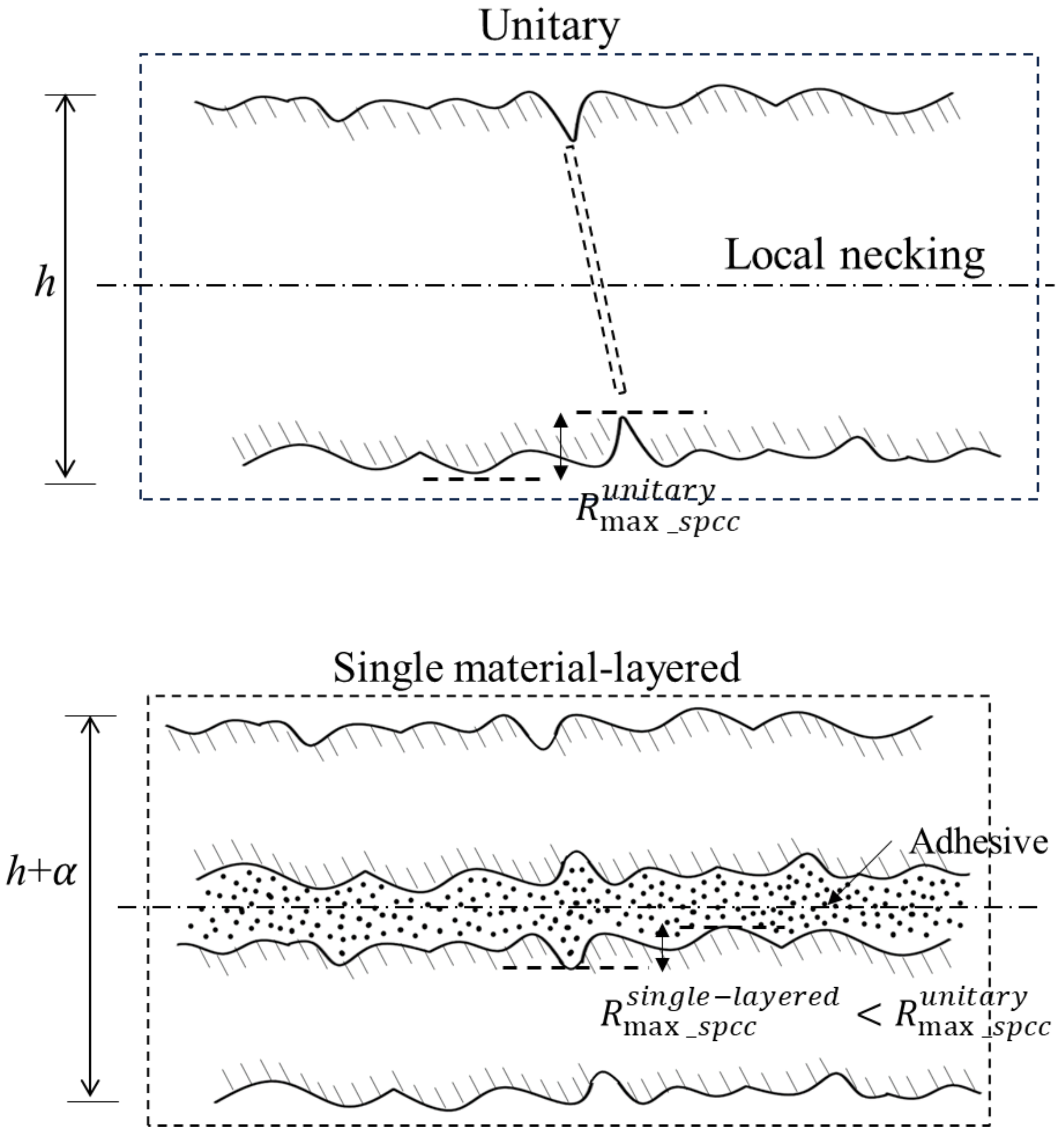

Fig. 4.16 The inhibitory effect on surface roughness of the adhesive as a polymer for SPCC.

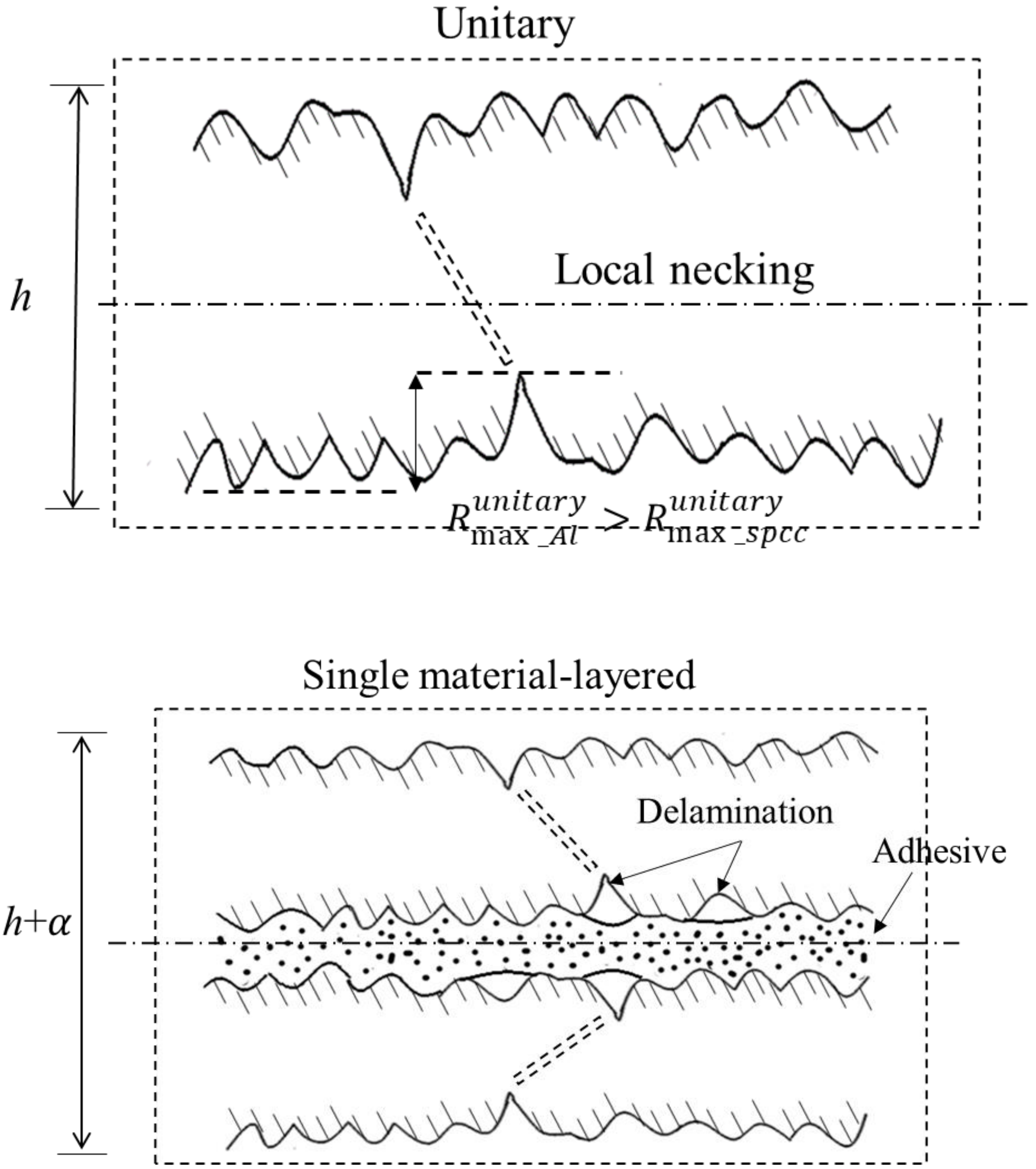

Fig. 4.17 The inhibitory effect on surface roughness of the adhesive as a polymer for Aluminum.

4.4. Conclusion

This chapter introduces a novel approach utilizing multi-layered plates bonded by adhesive, complemented by a specialized testing methodology based on conical cup testing. Unitary specimens of aluminum A1050, A5052, and steel SPCC, single (material)-layered specimens of A1050 bonded by epoxy adhesive, A5052 by acrylic, and SPCC by acrylic, and multi (materials)-layered specimens of A5052 and SPCC by acrylic were produced and tested. The examination of post-testing specimens, conducted at a 12 mm stroke, provides compelling evidence for the adhesive layer's role in augmenting the stability of bonded thin plates. This adhesive intervention effectively curtails asymmetrical deformation and forestalls the onset of local buckling.

Comparative analyses encompassing unitary specimens and single-layered specimens reveal an intriguing trend. In the scenario involving unitary specimens and single-layered specimens, each possessing an identical thickness of 1.2 mm and 1.6mm, the formability of the bonded specimens witnessed substantial enhancements. The inhibitory effect on surface roughness is considered to attribute the phenomenon of that the abrupt localized growth of surface roughness leads the local necking in the plate thickness direction. That is, it can facilitate the uniform deformation and increase the plastic formability due to the adhesive effect. Specifically, the forming limit reached a similar level with unitary specimens and had a slight increase of 4% exhibited for aluminum of A1050 and A5052 but exhibited a remarkable 40% increase for SPCC. This observed disparity in formability can be attributed to disparities in surface roughness characteristics between the materials. The influence of the adhesive is contingent upon the surface roughness of the adhered materials. Specifically, it is observed that delamination tends to manifest more readily on surfaces characterized by rougher textures. This propensity for delamination on rough surfaces exerts a pronounced impact on the efficacy of the adhesive interaction, marking a critical consideration in assessing adhesive performance. Furthermore, when examining the adhered specimens and the unitary ones sharing the same thickness of 0.6 mm, the transformative impact on formability becomes particularly pronounced. Here, the forming limit witnessed a striking increase, becoming 217% for A5052 and 176% for SPCC. This result suggests that the adhesive bonding factor manifests a formability akin to that of materials with double the thickness. This outcome signifies a remarkable enhancement in formability, chiefly attributed to the utilization of bonded multi-layer structures.

The comparative analyses of multi-layered specimens of A5052 and SPCC against the unitary specimens of A5052 or SPCC and the single-layered specimens using A5052 or SPCC serves as a poignant illustration of the significant influence exerted by adhesives on the endeavor of weight reduction through multi-materialization. The formability of the multi-layered specimens exhibited substantial enhancements, resulting in a notable 40% and 35% increase in the forming limit for A5052 and SPCC, respectively. Remarkably, this enhancement in formability was achieved concurrently with a commendable 33% reduction in weight compared with the unitary SPCC of the same thickness, underscoring the efficacy of the adhesive's role in this deformation process. These findings pertaining to multi materials-layer plates suggest that the adoption of adhesive bonding in plate materialization yields acceptable performance metrics, particularly in terms of achieving substantial weight reduction without compromising structural integrity. These results underscore the constructive influence of bonded multi-layer structures in enhancing the formability of single-layer specimens, and they hold significant promise in advancing materials engineering for weight reduction in various applications.

5. FEM Simulation of Conical Cup Testing

In Chapter 4, we employed the conical cup testing method that assesses the combined plastic formability of layered metal laminates bonded by adhesives. We conducted a detailed examination and comparison of the results obtained from three types of specimens. The conventional conical cup testing functions as an enclosed system, making it possible to gather and observe specimens only after testing has been completed. On the other hand, the original inclusion of a see-through aperture enhances the in-situ observation of the bottom of the specimens. Furthermore, the deformation process in conical cup testing encompasses a wide range of changes, including shrinkage flange deformation, elongation flange deformation, and rupture at the base of the punch. Consequently, the data collected from the testing is limited to load-displacement relations for the entire specimens quantitatively during the deformation, leaving critical details such as how the stress within the adhesive layer evolves during the deformation process unattainable through experimental means.

To gain a more comprehensive understanding of these crucial factors during testing, finite element analyses (FEM) were conducted using the same conical cup testing models. The FEM analyses allowed us to examine the performance of the concealed aspects of the specimens.

In this chapter, conical testing jig models were constructed and explored their use in FEM. We designed various patterns for the FEM models of specimens and thoroughly discussed their applicability. To ensure the accuracy of our analyses, we collected material properties for the same metals (Aluminum and SPCC) used in the ~~FEM~~ analyses by the uniaxial tension tests. These material properties were also compared with data obtained from the other reference sources.

An extensive comparative FEM analysis for different specimen types was constructed, including unitary, single(material)-layered, and multi(materials)-layered specimens. The findings from these analyses were further compared with the results of the experiments discussed in Chapter 4. A specific focus of our investigation was on the stress state within the adhesive layer. To gain deeper insights into the behavior of the adhesive layer during conical cup testing, we plotted the stress data onto the failure criterion curves, as detailed in Chapter 2. These analyses allowed us to examine the intricate behavior of the adhesive layer during the testing process, which can be challenging to assess through real experiments alone.

5.1. FEM models of conical cup testing

5.1.1. Models of conical cup testing jigs

To facilitate a direct comparison with the experimental results of the conical cup testing, the finite element analysis (FEM) model of the dies (illustrated in Fig. 5.1) was meticulously constructed to replicate the dimensions of the actual experimental jigs, as depicted in Fig. 4.1(a). A semispherical punch was incorporated into the model to simulate the metal used for pressing the specimens during testing. Both components were modeled using shell elements and designated as rigid bodies [113].

The jigs were assigned with the boundary conditions restricting all degrees of freedom, ensuring constriction in all directions. Meanwhile, the punch was subjected to the boundary conditions permitting movement exclusively along the z-axis. The coefficient of friction between the jig or punch and the specimen was set to be 0, considering the numerical stability and effectiveness. This comprehensive modeling aimed to closely emulate the experimental setup and conditions of the conical cup testing, facilitating ~~a~~ robust and meaningful comparative analysis between the FEM results and the actual experimental outcomes.

All the FEM analyses were performed by the commercial software HyperWorks (Ver. 2017.2, Altair Engineering, Inc.) which was installed into the self-constructed PC with CPU Intel® Core™ I9-10980XE which has 18 cores and 36 logical processors.

5.1.2. Models of specimens

The FEM models of specimens correspond to the three kinds of distinct specimen types introduced in Chapter 4 (the unitary, the single-layered, and the multi-layered) to assess the plastic formability of laminates bonded by adhesives. The material properties used for the validity of modeling are summarized in Table 5.1. Especially, the net area and length per beam element determines its tensile rigidity, bending rigidity and torsional rigidity, as shown in Table 5.1.

For the unitary specimen model, a plate composed of simple shell elements (as depicted in Fig. 5.2) was meticulously constructed, which has the total number of elements and nodes of 1404 and 1457, respectively. This model is well-suited for representing straightforward metal plates. The dimensions and kinds of materials as the unitary specimens are presented in Table 5.2, aligning with those employed in the actual conical cup testing.

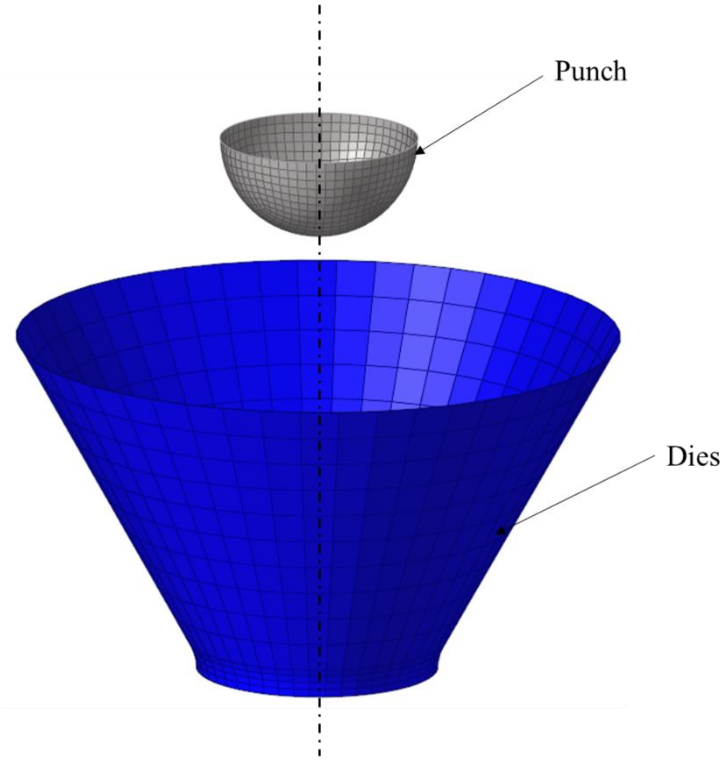

Fig 5.1 The models of dies and punch using in the FEM analysis

Table 5.1 The material properties used for the validity of modeling

Component	Property	Material	Young's modulus [GPa]	Poisson's ratio
Dies	Rigid body	Steel	-	-
Punch	Rigid body	Steel	-	-
Plates	Shell	Steel/Aluminum	210/70	0.3/0.35
Adhesive	Solid/Beam	Acrylic	0.35	0.4

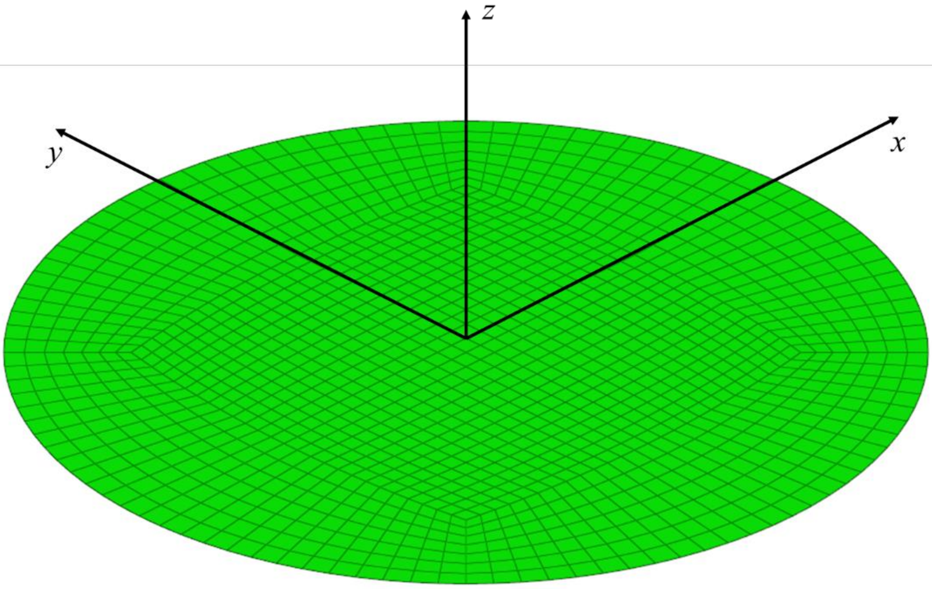

Fig 5.2 The FEM model for unitary specimens made of shell elements

Table 5.2 Dimensions and materials of the unitary specimen model

Specimens Type	Property	Material	Radius [mm]	Thickness [mm]
Unitary	Elasto-plastic	A5052	50	1.2
Unitary	Elasto-plastic	A5052	50	0.6
Unitary	Elasto-plastic	SPCC	50	1.2

Creating models for the single-layered and multi-layered specimens presents a more intricate challenge due to the composite nature involving three components: top metal layer, adhesive layer, and bottom metal layer. Initially, a model consisting of three laminated solid plates using solid element was considered with the top and bottom representing metal layers and the middle one representing the adhesive layer. However, when applied to the loading, as illustrated in Fig. 5.3, the solid elements failed to deform accurately, reflecting the disparity between the model and real conical cup testing. The inadequacy stemmed from each component having only a single layer, insufficient for simulating specimen deformation effectively due to the less mesh partition. To address this, the layer for each component was doubled (as depicted in Fig. 5.4), augmenting the element count in the thickness direction for smoother deformation.

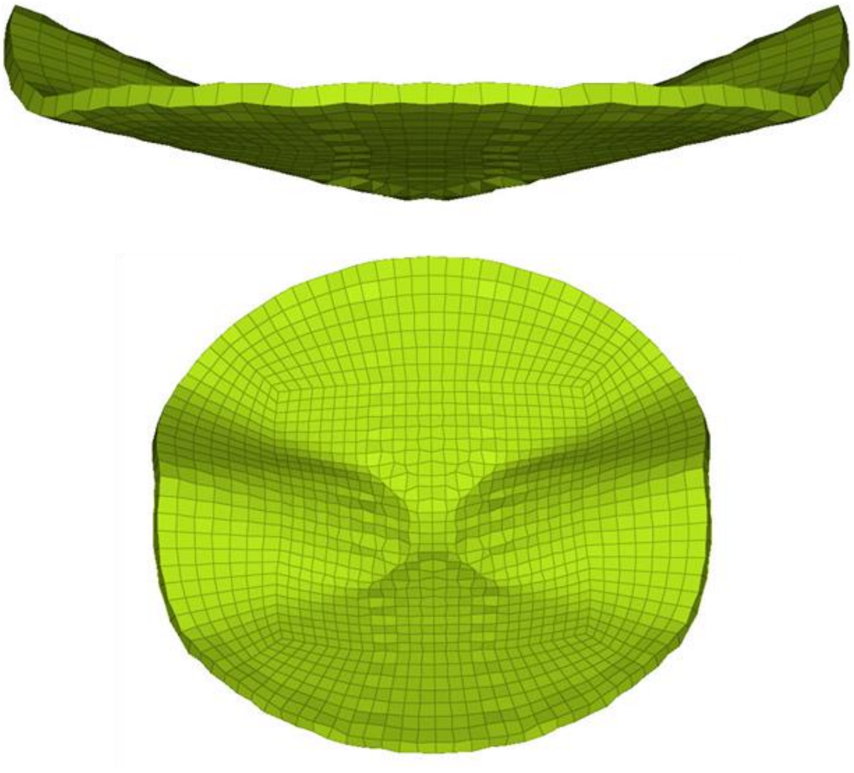

Fig 5.3 Deformation of one layer of the layered specimens model of solid elements.

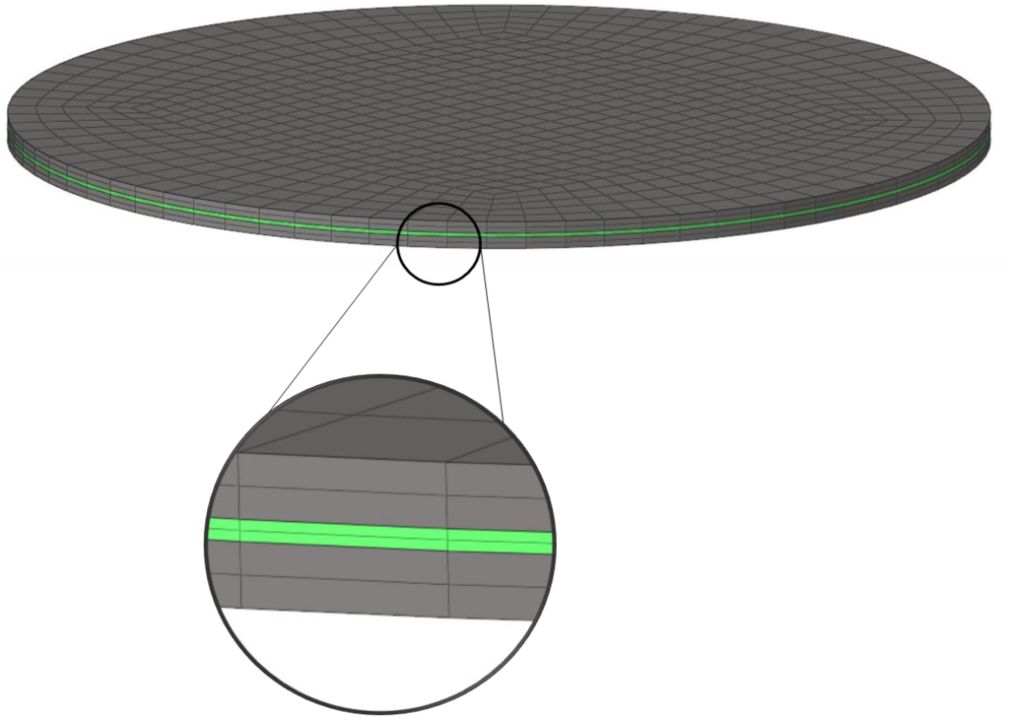

Fig 5.4 Model of layered specimens model of solid elements with two layers in thickness direction.

However, doubling the elements for all three layers resulted in a twofold increase in overall elements up to the number of elements and nodes with 8424 and 10199, respectively, significantly prolonging the analysis time. The computational time exceeded 500 hours, equivalent to approximately 20 days per analysis run. This extended duration was deemed unacceptable, given the multitude of specimens requiring analysis. Consequently, a more efficient approach was sought.

As previously discussed, establishing a connection between the top and bottom metal layers with an acceptable analysis time is crucial. To achieve this, the top and bottom plates, were replaced with shell elements, similar to the unitary models. The middle adhesive layer retained solid elements to simulate the bonding effect of the adhesive layer, as depicted in Fig. 5.5. This adjustment facilitated the overall behavior comparable to the solid models, with the output of the shell plates aligning with that of the solid ones, while the adhesive layer remained unchanged. The total number of elements decreased to about

2/3 of the former solid model, and the running time was reduced to approximately 190 hours. They are deemed acceptable. The dimensions and properties of the single-layered and multi-layered models are detailed in Table 5.3.

Table 5.3 Dimensions and materials of singe- and multi-layered specimen model

Specimens Type	Laminate property	Adhesive property	Material	Radius [mm]	Thickness (Adhesive) [mm]
Single-layered	elasto-plastic	elastic	A5052-A5052	50	0.6+0.6 (+0.4)
Single-layered	elasto-plastic	elastic	SPCC-SPCC	50	0.6+0.6 (+0.4)
Multi-layered	elasto-plastic	elastic	A5052-SPCC	50	0.6+0.6 (+0.4)

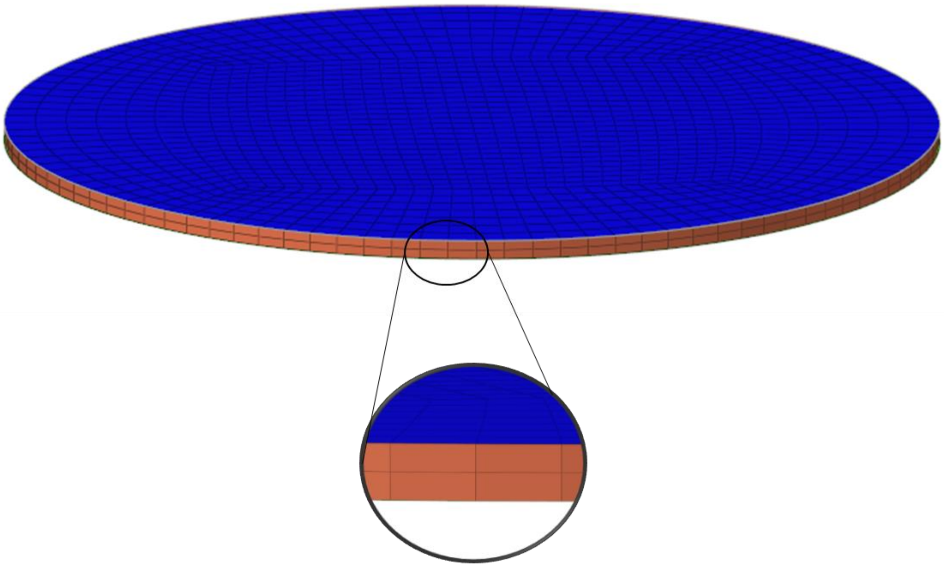

Fig. 5.5 Model of layered specimens model of shell and solid elements with two layers in adhesive layer.

While the shell-solid model yielded results and reduced running time to about one week, it was still relatively long considering the volume of samples requiring analysis. Referring to Table 5.3, the metal plates were assumed to be elasto-plastic bodies, and the adhesive layer was considered an elastic body. This allowed for the replacement of solid elements in the adhesive layer with beam elements, connecting corresponding nodes of the two shell plates. This led to a more simplified model comprising only shell and beam elements, as illustrated in Fig. 5.6. The total number of elements decreased to about 1/2 and 3/4 of the former solid model and shell model, respectively, and the running time was reduced to approximately 140 hours.

In the comparison of load-displacement curves between the “shell-solid-shell” and “shell-beam-shell” models for single-layered aluminum specimen, shown in Fig. 5.7, it is evident that as the stroke deepens, the load for the shell-solid-shell model exceeds that of the shell-beam-shell model. This discrepancy arises because the beam elements, serving to connect the nodes of metal shell elements, lose effectiveness to represent the deformation of adhesive layer as deformation increases. Consequently, the total stiffness of the adhesive layer diminishes, resulting in a smaller reaction force receiving in the punch. Despite this, both models exhibit similar overall performance within the same magnitude. Therefore, the simplified shell-beam-shell model can be still employed, saving the running time for the model with the much larger number of degree of freedom. It's important to note that stress state data for the adhesive layer cannot be output for the beam elements in the current commercial-based software. Hence, for a comprehensive understanding of the adhesive's effect during deformation, the shell-solid-shell model remains essential.

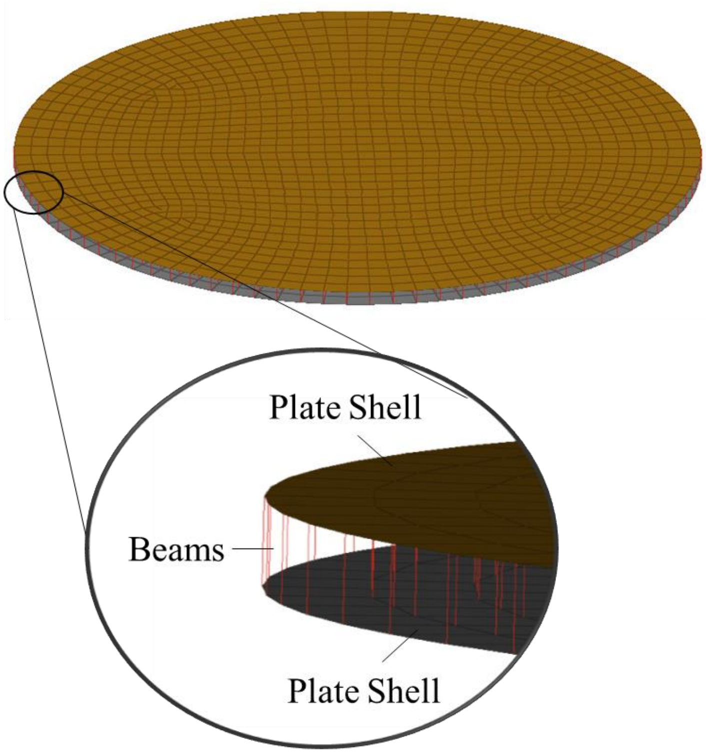

Fig 5.6 Model of layered specimens model of shell and beam elements

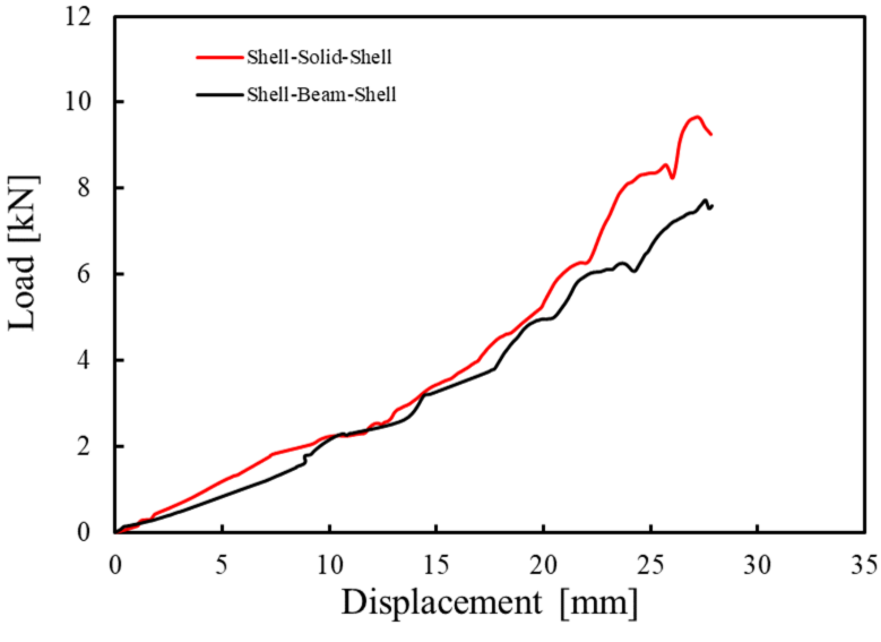

Fig 5.7 Load-displacement curves between shell-solid-shell and shell-beam-shell models for a single-layered Aluminum specimen.

5.2. Material properties applied to FEM analysis.

In the pursuit of comprehending the hidden phenomena and behaviors inherent in real conical cup testing, it becomes imperative to harmonize the material properties of the FEM model with those of the actual materials utilized in the experiments. This alignment is particularly crucial for the metal laminates, given that the overarching objective of the research is to assess the formability of bonded layered laminates.

Additionally, our analysis assumes an elasto-plastic behavior for the metal plates. It delves into the realm of plastic properties, specifically the n-value and C-value in the following n-power law hardening model [114]:

$$\sigma = C\varepsilon^{n}, \tag{5.1}$$

Evaluating these aspects is paramount for ensuring a comprehensive and accurate representation of material behavior in the FEM analyses, thereby facilitating a deeper understanding of the concealed plastic deformation in conical cup testing.

5.2.1. Tensile testing

To ascertain the material properties of the metals employed in specimen fabrication, a conventional flat tensile testing specimen was utilized, featuring dimensions outlined in Fig. 5.8. Each specimen was equipped with a bi-axial strain gauge, meticulously positioned to capture strain in both the z-axis and x-axis as shown in Fig. 5.9 (a). This setup facilitated the precise determination of Young's modulus and Poisson's ratio, ensuring accuracy through the deployment of the AG-50kNX tensile testing machine from Shimadzu Co., Ltd., as illustrated in Fig. 5.9 (b). The specifics of the materials and the respective specimens are comprehensively detailed in Table 5.4.

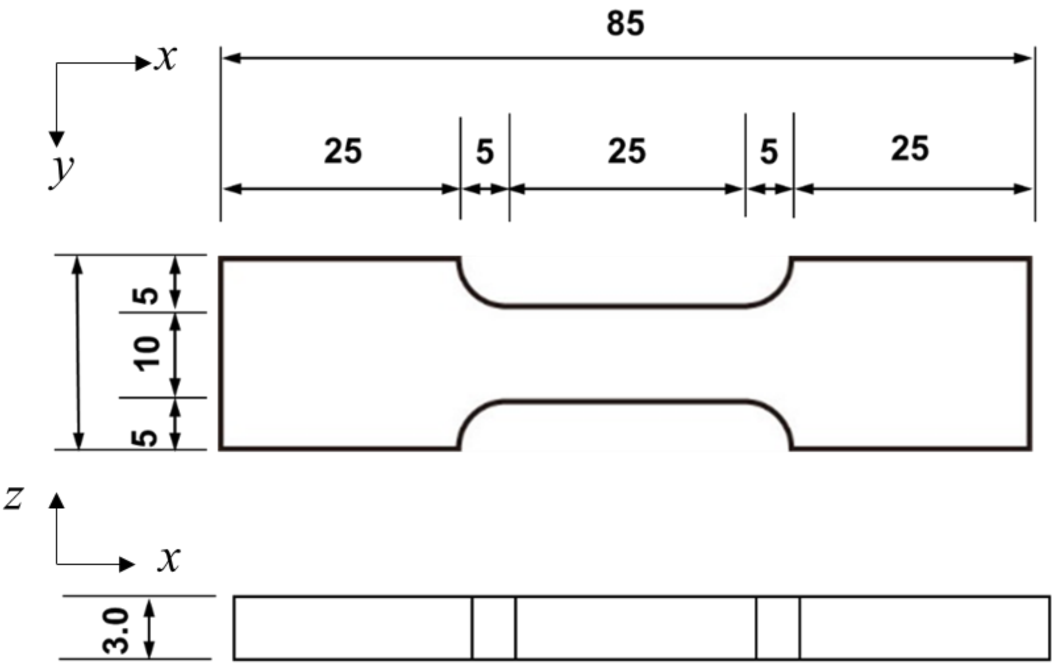

Fig. 5.8 The dimensions of flat tensile testing specimen used to evaluate material properties.

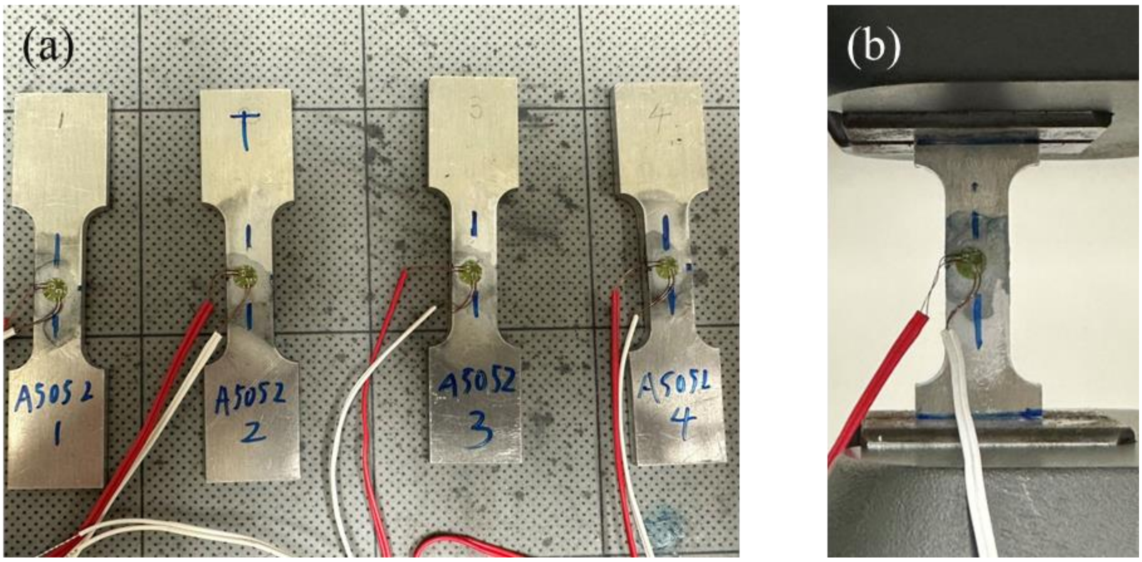

Fig. 5.9 The specimens with stain gage attached used in the tensile testing. (a) Bi-axial strain gage attached to specimens in z-axis and x-axis. (b) Specimens set to the tensile testing machine AG-50kN.

Table 5.4 The details of the specimens made from different materials

(a) A5052

Specimens No	Material	Parallel section Length [mm]	Parallel section Width [mm]	Thickness [mm]
1	A5052	24.9	10.1	2.98
2	A5052	24.9	10.1	2.96
3	A5052	25.1	10.1	2.95
4	A5052	25.0	10.1	2.94

(b) A1050

Specimens No	Material	Parallel section Length [mm]	Parallel section Width [mm]	Thickness [mm]
1	A1050	25.0	10.2	3.02
2	A1050	24.0	10.1	3.03
3	A1050	25.1	10.1	3.02
4	A1050	24.8	10.1	3.05

(c) SPCC

Specimens No	Material	Parallel section Length [mm]	Parallel section Width [mm]	Thickness [mm]
1	SPCC	23.8	9.96	3.16
2	SPCC	23.9	9.96	3.15
3	SPCC	24.1	9.97	3.15
4	SPCC	23.8	9.95	3.15

5.2.2. Estimation of hardening and material properties

The tensile testing was performed for all the three kinds of specimens listed in Table 5.4 with a strain rate of 6.67×10^{-4} [/s], which is satisfied with the requirement of quasi-static process. The nominal stress and strain were estimated according to the load-displacement relations collected from experiments:

$$\sigma_n = \frac{F}{A}, \tag{5.2}$$

$$\varepsilon_n = \frac{D}{L_0}, \tag{5.3}$$

where A is the cross-section area and L_0 is the original length of the parallel section shown in Table 5.4. An exemplary A5052 specimen is depicted in Fig. 5.10. The unloading and reloading process was iteratively conducted twice for one of the four specimens, ensuring a comprehensive strain collection to derive an accurate estimate of Young's modulus. Further illustrating the process, Fig. 5.11 showcases an example of specimen A5052-3.

Poisson's ratio was determined by computing the average of results from all specimens, accounting for the strains in both tensile and lateral directions:

$$v = -\frac{\varepsilon_x}{\varepsilon_z}, \tag{5.4}$$

with the example of specimens A5052-1 shown in Fig. 5.12. The processes above were performed for three specimens made from the three kinds of materials and the averaged Young’s modulus and Poisson’s ratio are shown in Table. 5.5. The material property of the adhesive layer is the same as the acrylic adhesive used in the optimization simulation of pipe specimens discussed in Chapter 3 with Young’s modulus of 0.35 GPa and Poisson’s ratio of 0.4.

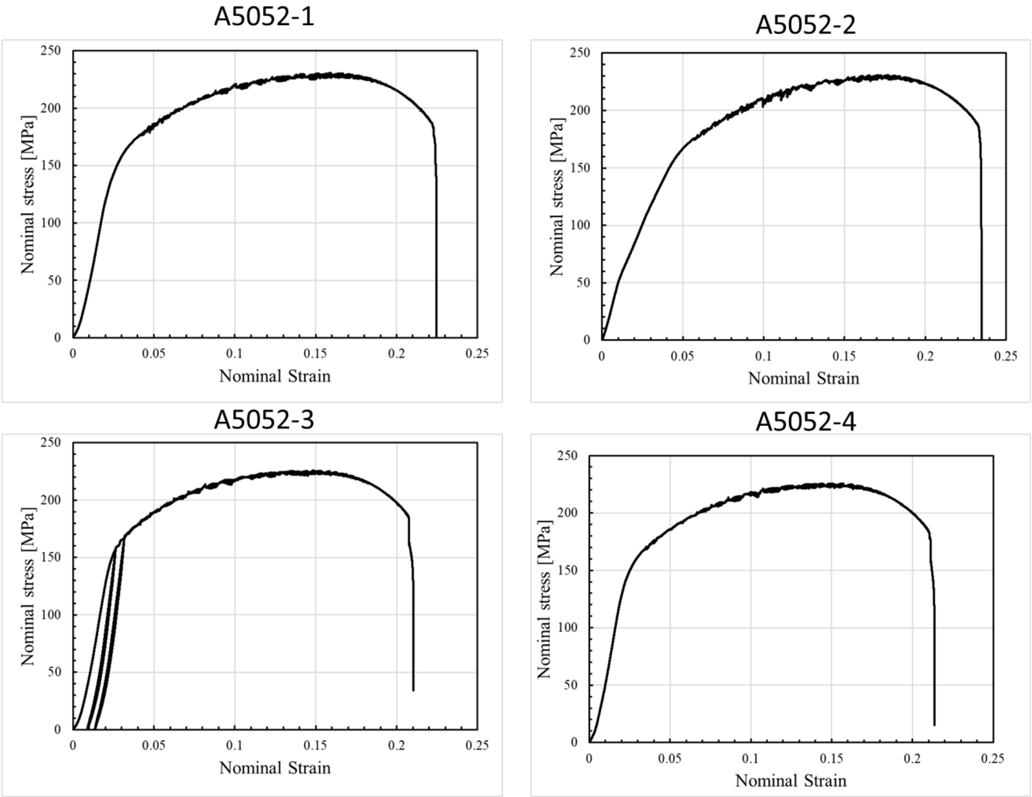

A5052-1

A5052-2

A5052-3

A5052-4

Fig. 5.10 The nominal stress and strain curves for the four specimens made of A5052

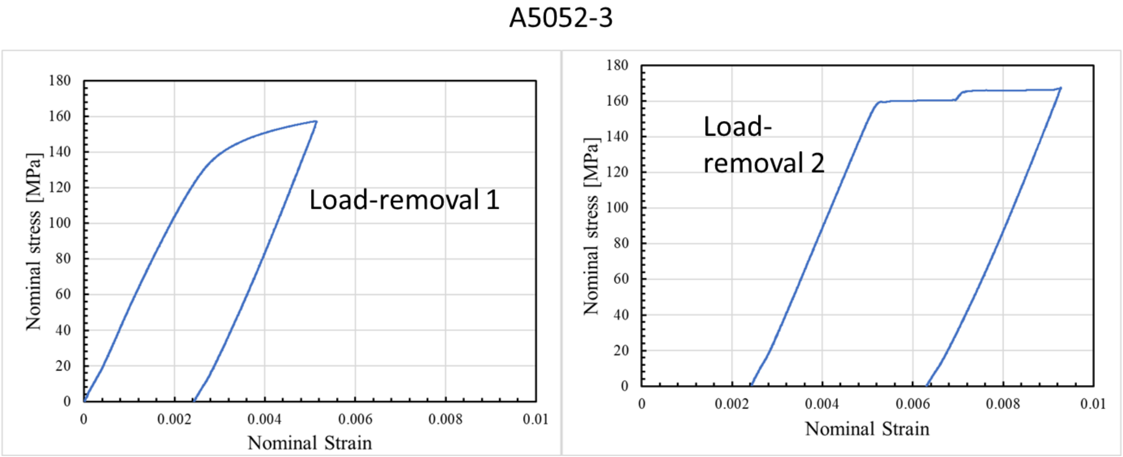

A5052-3

Fig. 5.11 The unloading and reload process of specimen A5052-3

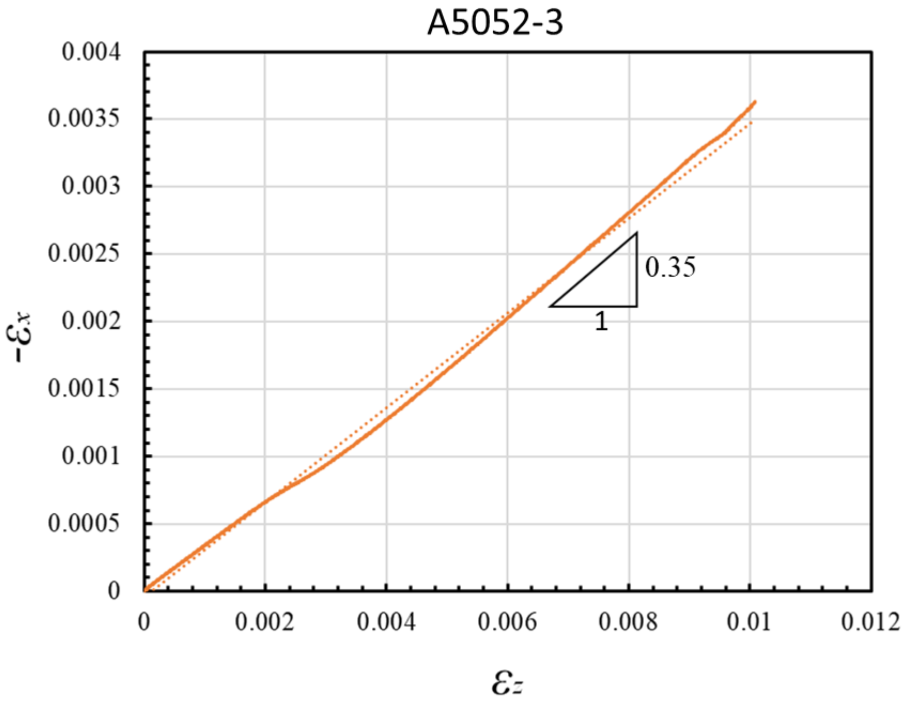

Fig. 5.12 The horizontal strain $-\varepsilon_x$ versus the vertical strain ε_z for the specimen A5052-3. The slope expresses the Poisson's ratio.

Table 5.5 The material properties estimated from the experiments

Material	Young's modulus [GPa]	Poisson ratio
A1050	56.6	0.30
A5052	59.8	0.35
SPCC	150	0.32

In order to get the *n*-value and *C*-value in Eq. (5.1) which should be applied into the elasto-plastic analyses of metal laminates, it is necessary to obtain the true stress and true strain. The plastic nominal strain is first estimated as:

$$\varepsilon_n^p = \varepsilon_n - \frac{\sigma_n}{E}, \tag{5.5}$$

where σ_n and ε_n are nominal stress and total strain obtained form Eqs. (5.2) and (5.3). E is Young's modulus including errors obtained from original experiment data. Then, the total nominal strain could be adjusted with the correction:

$$\varepsilon_n' = \varepsilon_n^p - \frac{\sigma_n}{E'} \tag{5.6}$$

where E' is the accurate Young’s modulus obtained according to Fig. 5.11. Thus, the true stress and true strain could be estimated from the adjusted nominal strain as:

$$\sigma_t = \sigma_n e^{\varepsilon_t} = \sigma_n(1 + \varepsilon_n'), \tag{5.7}$$

$$\varepsilon_t = \ln(1 + \varepsilon_n'). \tag{5.8}$$

Subsequently, the *n*-value and *C*-value in Eq. (5.1) were deduced by fitting the curve of true stress and true strain. Fig. 5.13 illustrates this fitting process using A5052 specimens. The black line represents the curve of nominal stress and adjusted nominal strain, the blue line delineates the curve of true stress and true strain, and the red line signifies the fitting curve in accordance with the hardening law presented in Eq. (5.1). The averages of the *n*-value and *C*-value were calculated from all specimens with curves of *n*-power law shown in Fig. 5.14. The acquired data for the three materials are documented in Table 5.6 alongside reference data [115]-[117].

Table 5.6 The *n*-value and *C*-value obtained from fitting with the reference data

Material	*n*-value	*C*-value [MPa]	*n*-value in reference	*C*-value in reference [MPa]
A1050	0.0381	132	0.24	155
A5052	0.193	391	0.29	400
SPCC	0.26	540	0.19	505

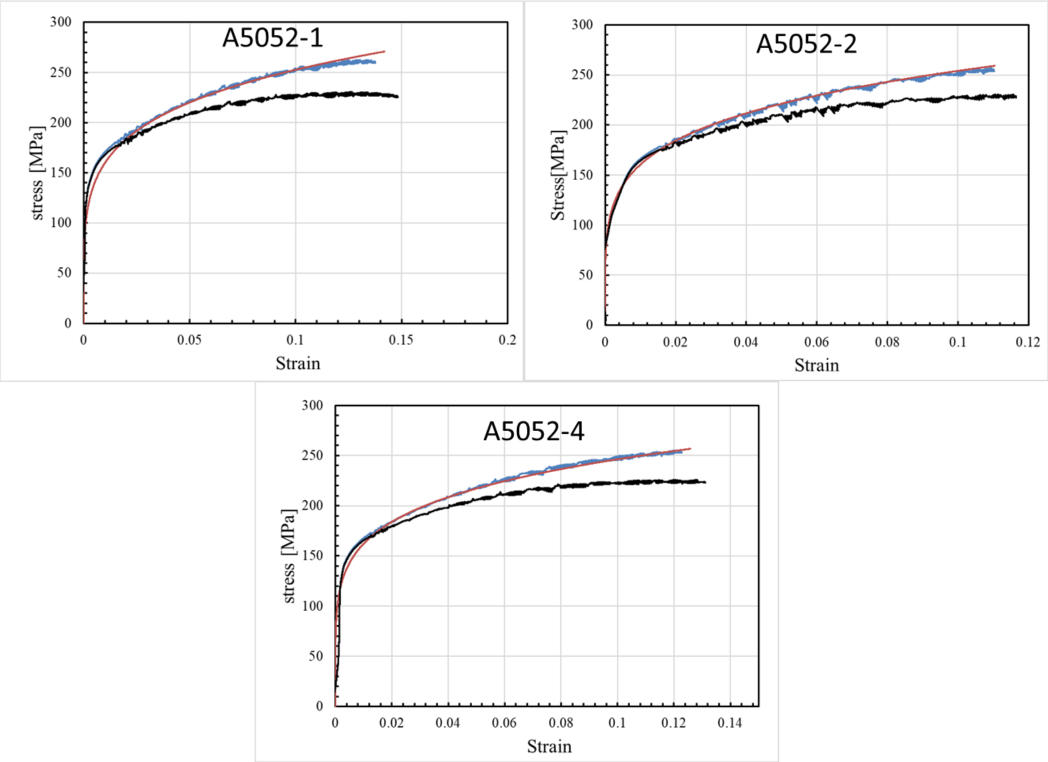

Fig 5.13 The fitting curve in accordance with the hardening law with the curve of true-stress-true stain and the curves of nominal stress and adjusted nominal strain.

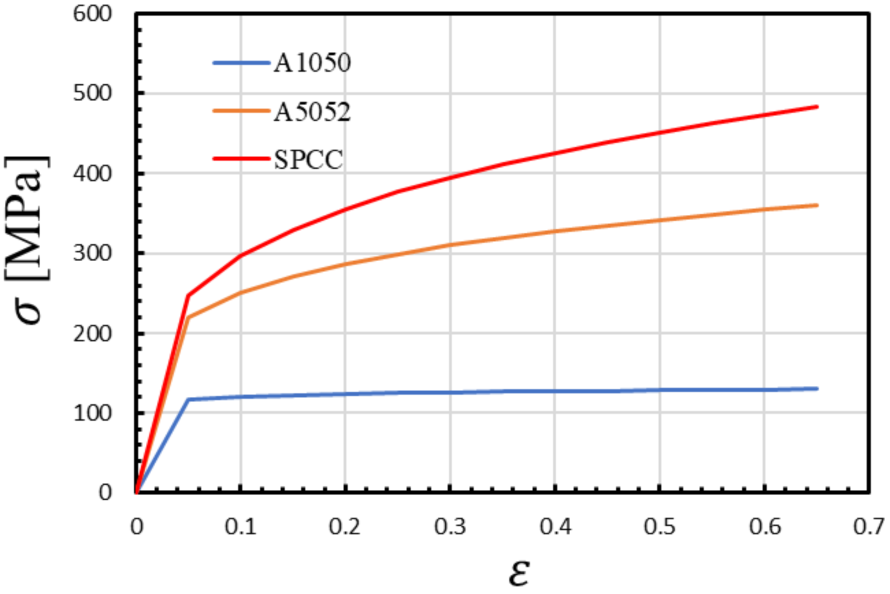

Fig 5.14 The *n*-power hardening law curves obtained from the fitting.

5.3. Results and discussions

5.3.1. General performance of FEM analysis

The simulations were executed with a punch velocity of 0.3 mm/min, considering the simulation time constraints. To maintain symmetry in the deformation process, a constrict boundary condition was applied to the four elements at the center of the circular specimen, allowing movement only along the *z*-axis. The specimens, as listed in Tables 5.2 and 5.3, were incorporated into the simulation.

As discussed in Section 4.2, the specimens of different materials in conical cup testing exhibit uniform deformation characteristics. The simulation mirrors these characteristics, with distinct magnitudes for the same type of specimens made of different materials, yet sharing identical deformation patterns. Consequently, the deformation of each specimen type is considered as a general performance in conical cup testing. In this section, specimens made of A5052 are chosen as typical features. The primary objective of the simulation is to comprehend the deformation process, unobservable during conical cup testing, and to verify the adhesive's effect. The simulation primarily focuses on the press deformation, employing displacement control without failure analysis. The selected simulation range spans from 0 mm to 30 mm, aligning with the experimental results in Section 4.2, where the load-dropping points consistently fall below 30 mm stroke.

The representative deformation patterns for unitary 0.6 mm, unitary 1.2 mm, and single (material)-layered specimens made of A5052 at 3 mm intervals from 0 mm to 30 mm are illustrated in Fig. 5.15 to Fig. 5.19.

In the initial phase, ranging from 0 mm to 12 mm, all three specimens exhibit uniform and symmetric deformation. Within the stroke range of 12 mm to 15 mm, single-layered and unitary 1.2 mm specimens continue to deform uniformly and symmetrically, while the deformation of unitary 0.6 mm specimens becomes asymmetric, with localized deformation occurring at the circumferential edge.

From 15 mm to 24 mm, the asymmetric deformation of unitary 0.6 mm becomes more pronounced, leading to complete shape collapse. Unitary 1.2 mm and single-layered specimens maintain symmetric deformation, although localized deformation at the circumferential edge also appears for unitary 1.2 mm specimens. In the final stage, from 24 mm to 40 mm, unitary 1.2 mm and single-layered specimens undergo significant deformation while remaining symmetric.

In the final stage, from 24 mm to 30 mm, unitary 1.2 mm and single-layered specimens undergo significant deformation while still remaining almost symmetric. However, localized deformation around the edge along the circumferential direction occurs for both specimens, but it is more apparent for the unitary 1.2 mm specimen. From this fact, it is important to note that, despite the much smaller Young's modulus of adhesive layer than the metal layers, the performance of single-layered specimen consisting of two A5052 unitary 0.6 mm layers and the adhesive layer is almost equivalent to that of A5052 unitary 1.2 mm regardless of the introduction of interface of adhesive layer. As long as no defect nucleation such as delamination or void occurs in the interface, the constraint due to the adhesive layer effectively delays the buckling of structure and plastic instability of localization.

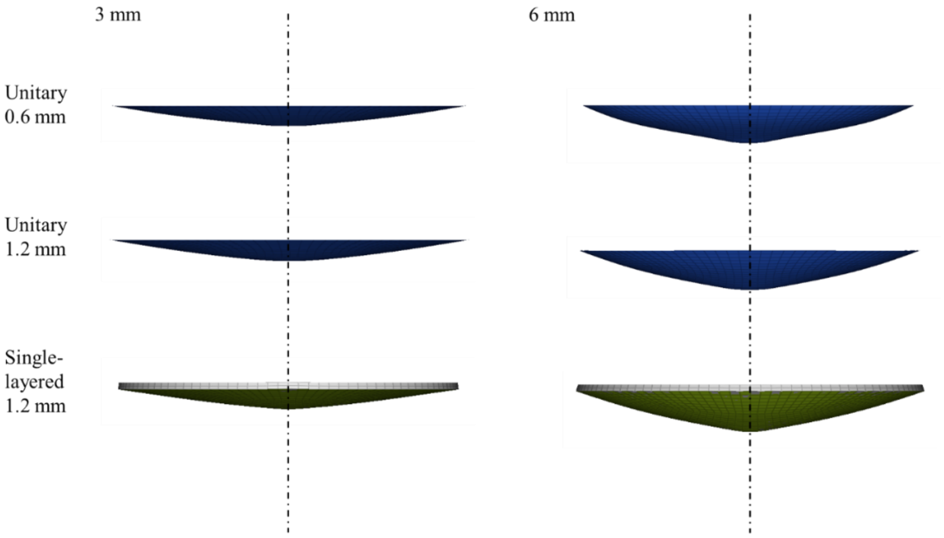

Fig 5.15 Deformation of unitary 0.6 mm, unitary 1.2 mm and Single-layered specimens at the strokes of 3 mm and 6 mm.

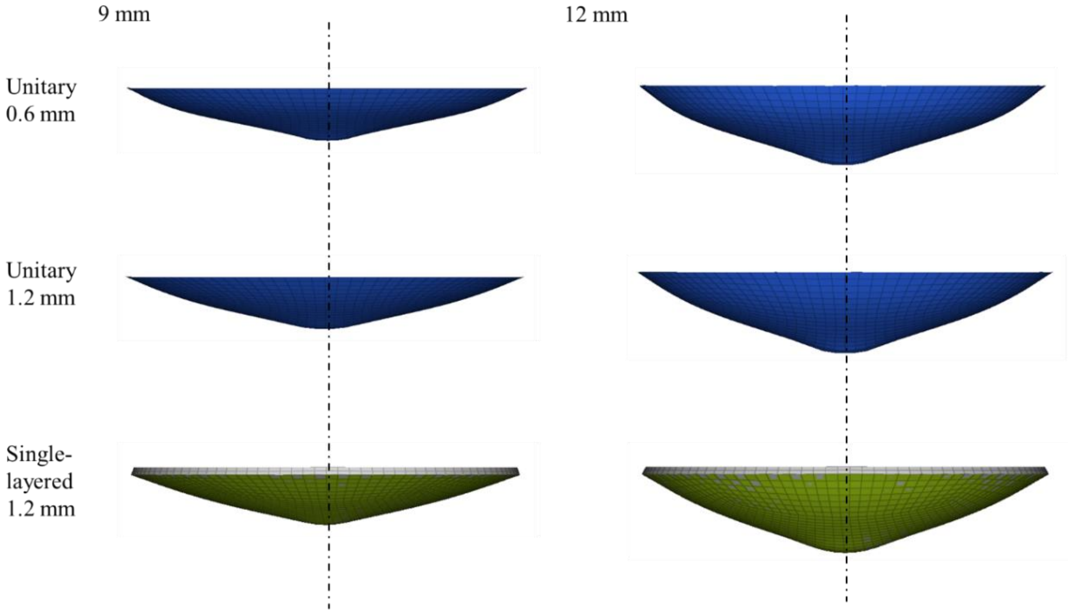

Fig 5.16 Deformation of unitary 0.6 mm, unitary 1.2 mm and Single-layered specimens at the strokes of 9 mm and 12 mm.

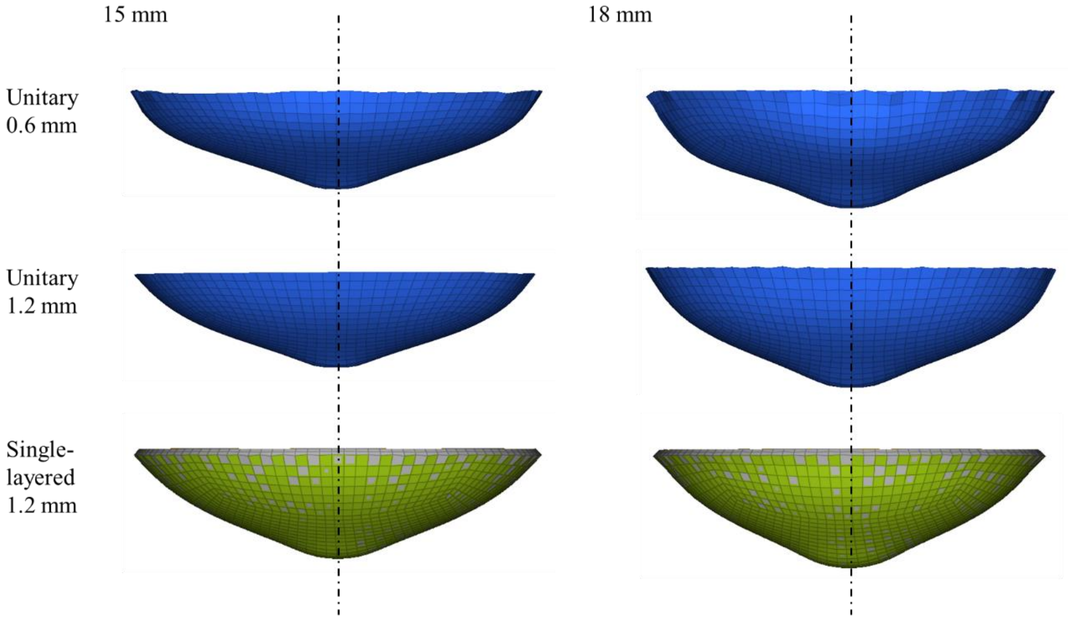

Fig 5.17 Deformation of unitary 0.6 mm, unitary 1.2 mm and Single-layered specimens at the strokes of 15 mm and 18 mm.

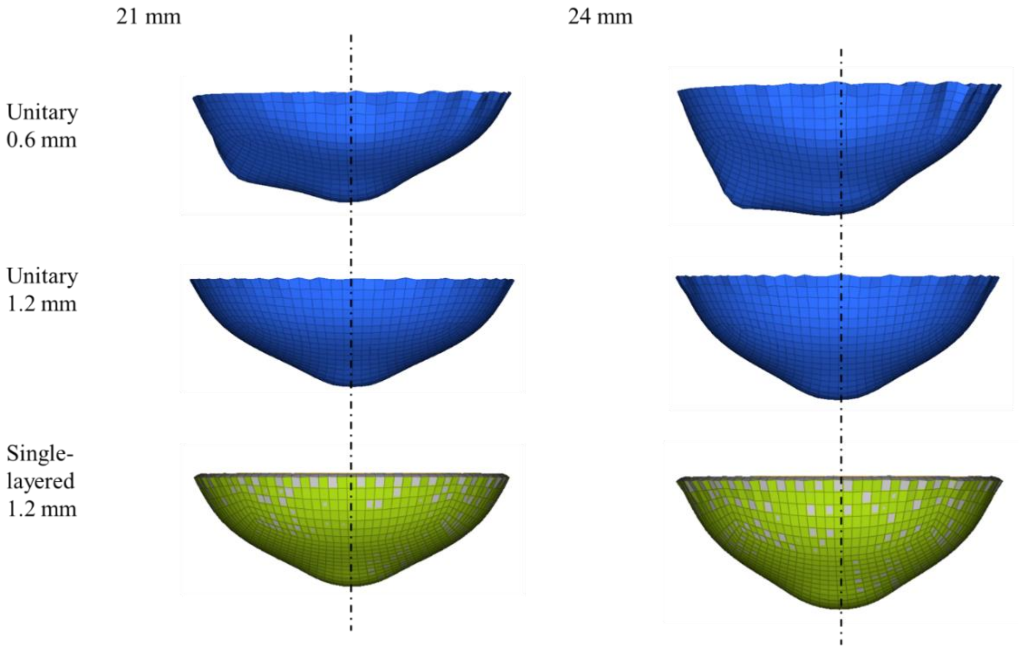

Fig 5.18 Deformation of unitary 0.6 mm, unitary 1.2 mm and Single-layered specimens at the strokes of 21 mm and 24 mm.

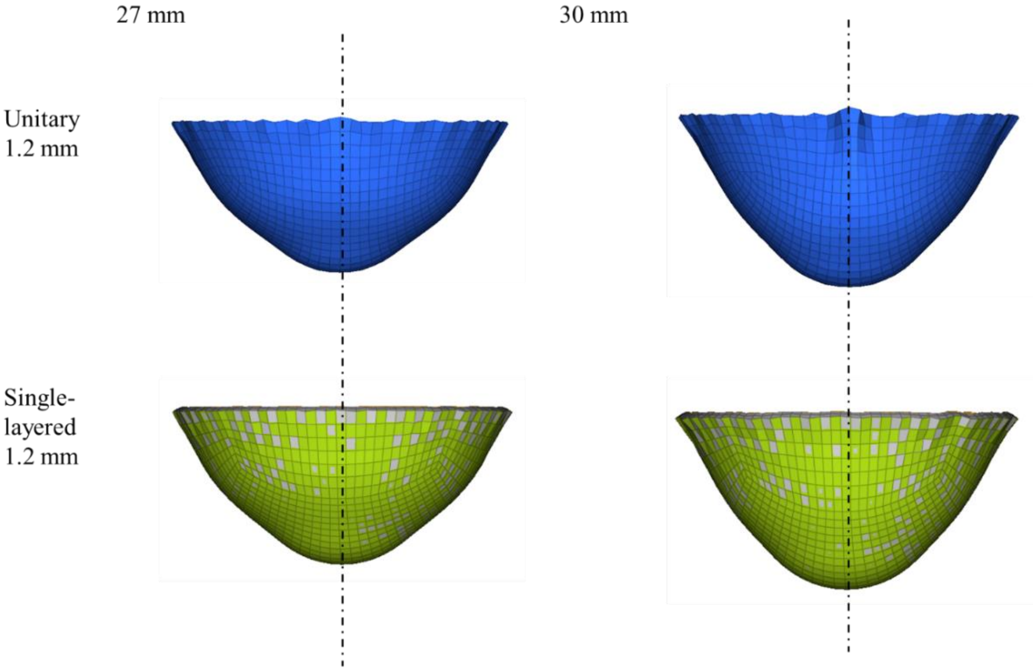

Fig 5.19 Deformation of unitary 1.2 mm and Single-layered specimens at the strokes of 27 mm and 30 mm.

5.3.2. Comparison between FEM and experiment results

To comprehend the deformation behavior discussed previously and compare with the experiment results of the specimens made of single kind of material, load-displacement curves for unitary 0.6 mm, unitary 1.2 mm, and single-layered specimens are presented in Fig. 5.20 with the results of real conical cup testing discussed in Chapter 4. First, the curves obtained from the FEM results for unitary 1.2 mm and single-layered specimens closely align, reflecting their uniform deformation process observed in Fig. 5.15 to Fig. 5.19.

Both curves between the FEM and experiment results generally agree well for all three specimen types. This congruence arises from the consistent geometry and boundary conditions set in both the simulation and real testing. Additionally, the material properties applied in the simulation were derived from the tensile testing results outlined in Section 5.2, ensuring identical representation with the actual specimens.

Remind that the curve of FEM in the unitary 0.6 mm continues because of no fracture while the experimental result stopped at around 13 mm due to the breaking. However, even the FEM solution becomes serrate after around 15mm due to the buckling and the severe antisymmetric deformation, as shown in Figs. 5.17, 5.18 and 5.19.

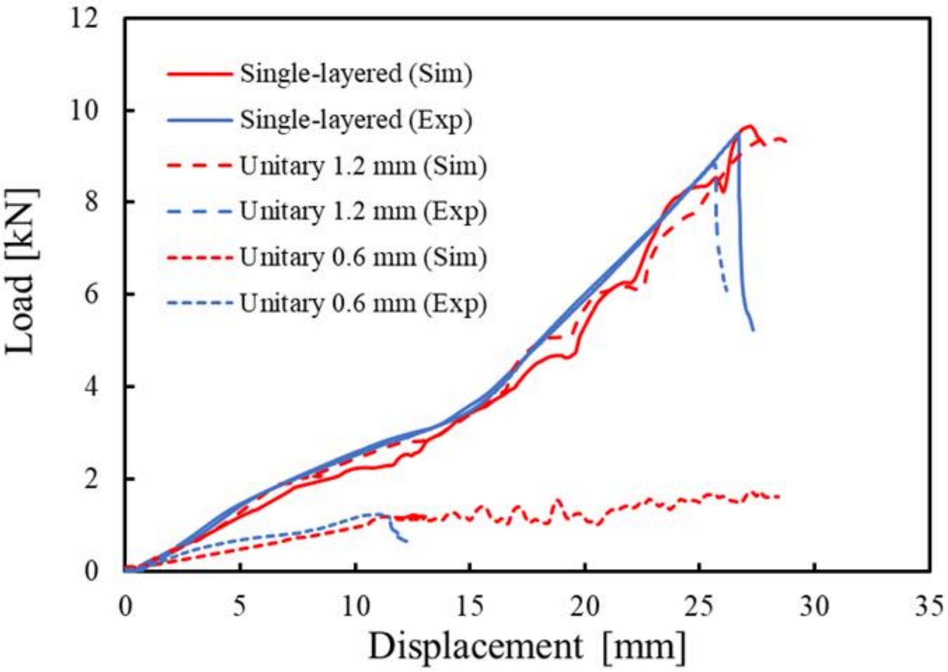

Fig. 5.20 The load-displacement curves of unitary 0.6 mm, unitary 1.2 mm and single-layered specimens. The red lines represent the simulation results and the blue lines represent the experiment results.

Subsequently, a comparison was conducted between the simulation results of multi-layered models and the actual multi-layered specimen made from A5052 and SPCC, bonded by acrylic adhesives. This comparison aimed to validate the appropriateness of the experimental results. Fig. 5.21, corresponding to Fig. 4.15, displays the load-displacement curves of the multi-layered specimens, alongside those of the experimental and simulated unitary specimens made from A5052 and SPCC. It's important to note that since the simulation did not include failure analysis, the load-drop points of the simulation cannot be identified. Therefore, the simulation range was chosen based on the experimental results in Fig. 4.15 to ensure a relatively accurate comparison.

The load-displacement curves of the simulated multi-layered specimens align uniformly with those of the real multi-layered specimens, similar to the behavior observed in the single-layered and unitary specimens. These results reaffirm the conclusion drawn from Fig. 4.15 that adhesive-bonded multi-layered specimens exhibit a significantly expanded forming limit with a notable reduction in weight. This marked enhancement in formability can be attributed to the adhesive's capacity to augment stability.

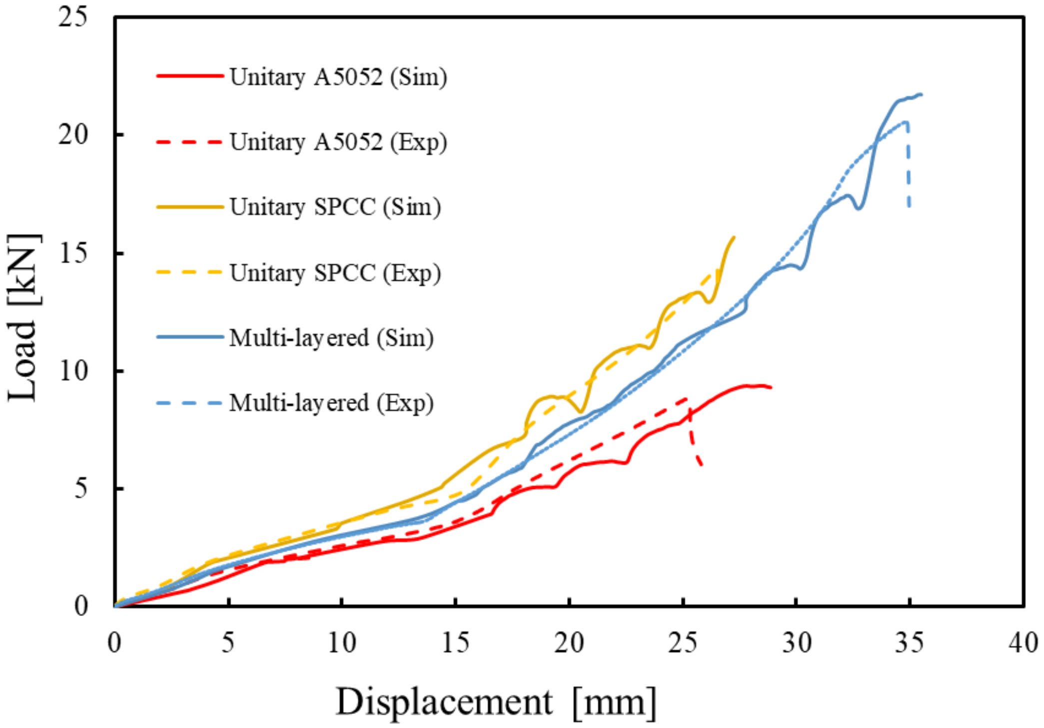

Fig. 5.21 The load-displacement curves of multi-layered specimens and the unitary specimens made of A5052 and SPCC. The solid lines represent the simulation results and the dotted lines represent the experiment results.

Furthermore, the assessment of the deformation simulation can be divided into two distinct phases, paralleling the real conical cup testing in Section 4.2. In the initial phase, spanning from 0 mm to approximately 15 mm, the metal sheet experiences elongation as drawing forces progressively increase due to the punch, signifying the initiation of plate deformation (Fig. 5.22 (a)). The second phase, commencing at approximately 15 mm, involves a notable transition where the fundamental drawing force begins to decline due to the diminishing flange area. As the material is more drawn into the die cavity, the contact area between the shell and the die undergoes significant expansion (Fig. 5.22 (b)). This amplified contact area results in an augmented reaction force from the die, heightening frictional resistance to drawing and increasing the draw force. This simulation allows examination of the specimens inside the jigs, providing insights into their deformation features, which are challenging to observe in real conical cup testing.

Significantly, in the case of unitary 0.6 mm, both experimental and simulation results indicate an early onset of load instability. In Section 4.3.2, when the unitary 0.6 mm specimens were extracted from the jigs for observation, their deformation was asymmetric, and a localized substantial deformation occurred on one side, as depicted in Fig. 4.10. However, pinpointing the exact stroke where the loss of symmetry began seems to be difficult in the experiments. The simulation aids in identifying such elusive features that are almost impossible to observe or pinpoint accurately in real testing. The simulated deformation of unitary 0.6 mm specimens in Fig. 5.17 and 5.18 reveals the loss of symmetry and the localization of deformation at the edge in the early stages of the deformation process at around 15 mm, as mentioned before. In contrast, the thicker unitary specimens and the bonded layered specimens maintain symmetric deformation and stability until the final stages, aligning with the observations in Section 4.3. Thus, the simulation can be considered an accurate analysis, suitable for examining the features of real testing that are otherwise challenging to approach.

Consequently, the simulation results and comparisons validate the conclusion that asymmetric deformation contributes to the loss of stability. With the influence of the adhesive layer, the top and bottom metal sheets can deform uniformly, eliminating the localization of local deformation. Thus, their formability is enhanced to the same level as thicker plates with twice their thickness because of the adhesive.

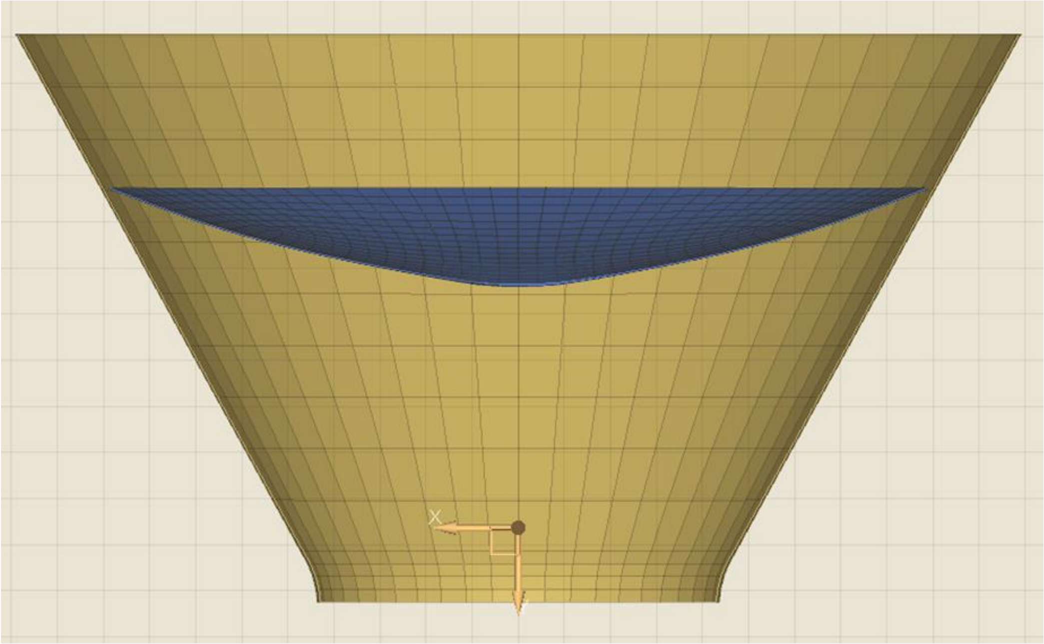

(a)

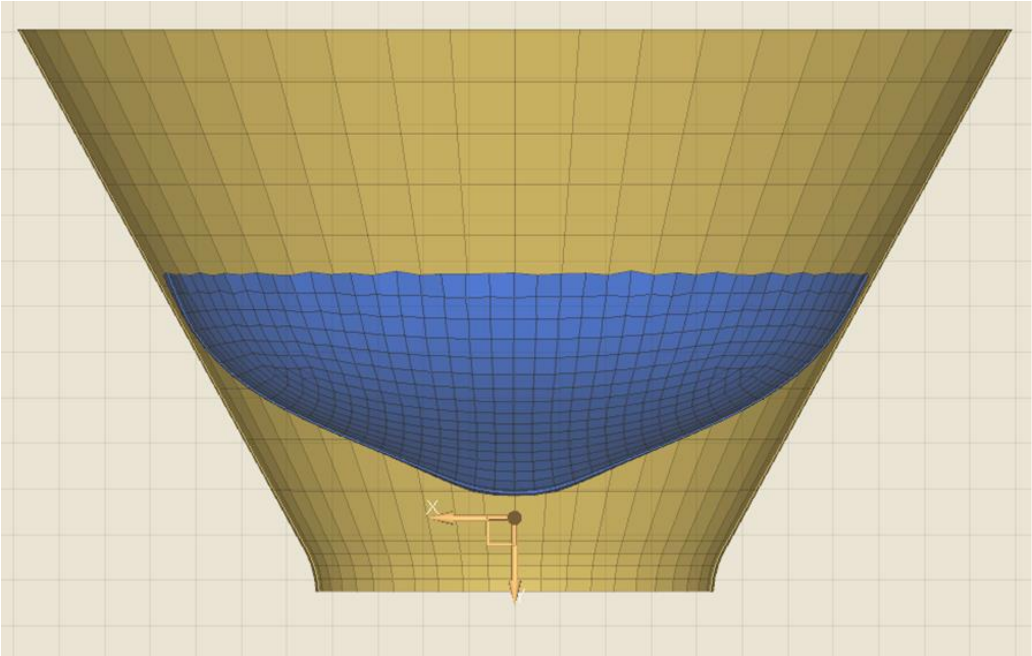

(b)

Fig. 5.22 The section view of deformation process during different stages of conical cup testing. (a) Phase 1 from 0 mm to about 15 mm and (b) Phase 2 after 15 mm.

5.4. Discussion on the adhesive layer during the deformation process

5.4.1. Line-wise stress distribution of adhesive layer

The discussion on the conical cup testing in Section 4.3 and the simulation results in Section 5.3 has emphasized the positive impact of the adhesive layer on enhancing the formability of layered specimens. The adhesive layer facilitates uniform deformation of the two thin plates, preventing localized deformation. Consequently, a thorough examination of the adhesive's behavior during testing becomes essential to comprehend the bonding mechanism of layered laminates and substantiate the adhesive's efficacy in improving formability. As outlined in Chapter 4, no information on the stress states in the real conical cup testing is expected due to the lack of measurement way. Thus, the simulation results of the adhesive layer, where the stress state can be extracted, prove invaluable in scrutinizing the adhesive's performance.

Given the symmetrical deformation of circular specimens within the adhesive layer before reaching instability, the stress states among elements along the circumference at the same radius exhibit uniformity. Consequently, the sequence of elements along the radial direction serves as representative indicators. To comprehensively grasp the stress state distribution across each part of the entire specimen and to discern the evolving patterns during the process, elements adjacent to the centerline were selected, spanning along one diameter line from -a to a with the center of the specimens presumed as the origin where a is the initial length from the origin to the outer edge, as depicted in Fig. 5.23

As elucidated in Chapter 2, the adhesive undergoes a complex stress state in real manufacturing or industrial processes. To assess the elastic limits of the adhesive material under multi-axial stress conditions, failure criterion curves were plotted in the mean stress (σ_m) and octahedral shear stress (τ_{oct}) plane. Since the adhesive layer in the simulation is also assumed to be elastic, the failure criterion curve of the acrylic adhesive in the σ_m and τ_{oct} plane of Fig. 2.5 (b), can be employed to evaluate the stress state of the adhesive layer in the conical cup testing simulation. The mean stress σ_m and octahedral shear stress

τ_{oct} of the elements in the model of single-layered A5052 specimens bonded by acrylic adhesive were calculated according to the first invariant of stress tensor I_1 and the second invariant of deviatoric stress tensor J_2 by Eqs. (2.5) and (2.6) with the relations $\sigma_m = \frac{1}{3}I_1$ and $\tau_{\mathrm{oct}} = \sqrt{\frac{2}{3}J_2}$. In contrast to the tensile testing of pipe specimens, which involves only a positive mean stress, the adhesive layer in conical cup testing may undergo compression, resulting in a negative mean stress. Consequently, the failure criterion discussed in Section 2.3 was extended to the negative direction in the σ_m axis, indicated by the red-colored curves in the following figures. In general, the adhesive shows the strong anisotropy in strength, which means that the strength for compression is much larger than that of expansion. Thus, this assumption may be in the safe side in the structural analyses. It is crucial to note that the failure criterion curve was derived from the elastic limits, implying that exceeding the boundary of the curves signifies deformation beyond the elastic limits.

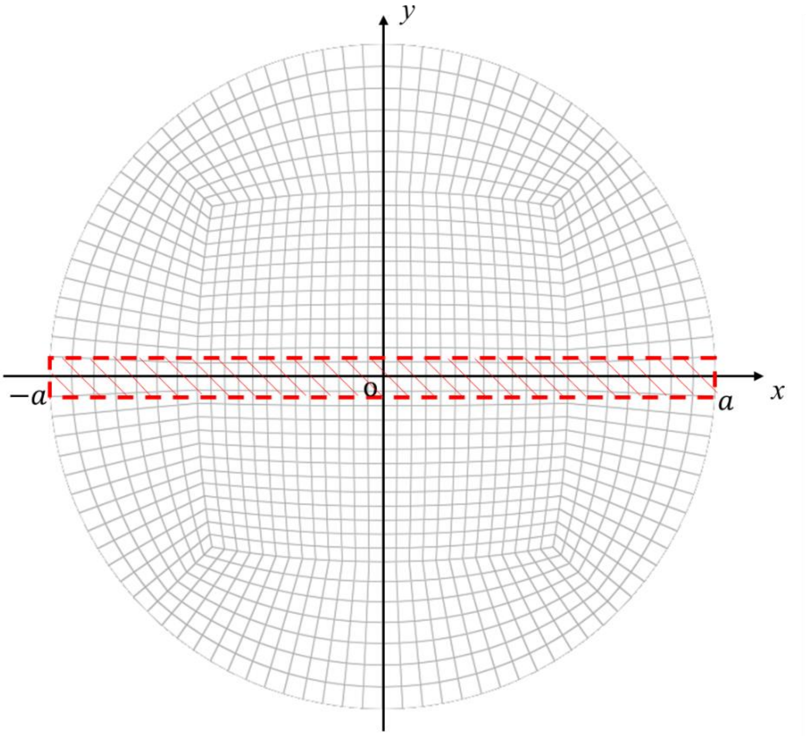

Fig. 5.23 Elements adjacent to the centerline spanning from -a to a in radial direction,

with the center of the specimens presumed as the origin.

Four significant stages were examined at strokes of 0 mm, 6 mm, 18 mm, and 27 mm, as illustrated in Fig. 5.24. Remind that the horizontal axis indicates a mean stress and the vertical one does an octahedral shear stress. All the obtained stress set of the mean stress and octahedral shear stress along the prescribed line in the plate are plotted in Fig. 5.24, which are averaged toward thickness. At the 0 mm stroke in Fig. 5.24 (a), no load was applied, resulting in a stress state of zero. For the 6 mm stroke in Fig. 5.24 (b), corresponding to phase 1 of the conical cup testing (as discussed in Section 4.2 and Section 5.3), the specimen undergoes elongation due to the drawing force applied by the punch, and most elements remain within the failure curve. This suggests that the majority of the adhesive layer was still under elastic deformation. The distribution of elements was relatively stable, indicating a steady stress state for the adhesive layer.

At the 18 mm stroke (considered as phase 2) in Fig. 5.24 (c), where deep drawing effects intensified with the increasing contact area between the specimens and dies, both the magnitudes of σ_m and τ_{oct} experienced a rapid increase. This aligns with the discussion on the load-displacement curve, signifying a notable transition after approximately 15 mm. All elements had crossed the failure curve, indicating that the deformation of the adhesive layer becomes plastic, consistent with the high level of deformation observed at this stage of the testing process.

At the 27 mm stroke in Fig. 5.24 (d), representing the final stage according to the experimental results where failure occurred at the specimen's bottom, the stress state reaches a considerable level, and the distribution of elements becomes highly decentralized.

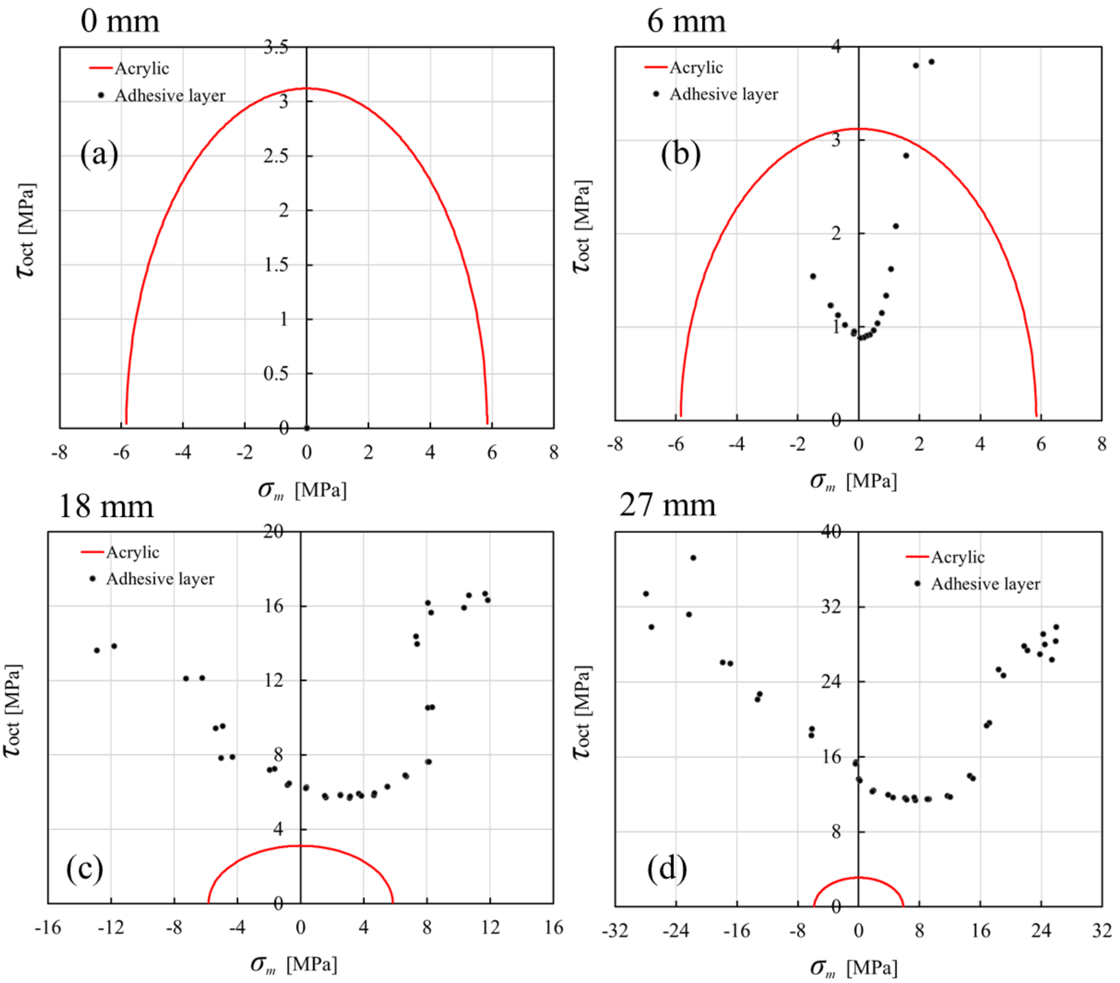

Fig 5.24 Stress states of the elements adjacent to the centerline in the σ_m and τ_{oct} plane with the failure criterion curve of acrylic adhesive at different strokes during the conical cup testing simulation. (a) 0 mm, (b) 6 mm, (c) 18 mm and (d) 27 mm.

Furthermore, to elucidate the symmetry of the specimens during testing, the mean stress and octahedral shear stress of selected alonglements in Fig. 5.23 were individually plotted against their distance from the center of the circular specimens. These plots were generated for four distinct stages at strokes of 0 mm, 6 mm, 18 mm, and 27 mm, as illustrated in Fig. 5.25 for the mean stress and Fig. 5.26 for the octahedral shear stress. In this representation, the origin is fixed at 0, with the minus quadrant (depicted in red) denoting elements in the left half of the specimen, and the plus quadrant representing elements in the other half.

At a stroke of 0 mm, both mean stress and octahedral shear stress were uniformly zero for all elements, indicating an absence of applied load. As evident in Figs. 5.25 (b) and ~~Fig.~~ 5.26 (b), the plots exhibited nearly perfect symmetry against the vertical axis, signifying that symmetric deformation persisted at any stage. Notably, large octahedral shear stress coincided with substantial mean stress, particularly at the center of the specimens directly pressed by the punch. Thus, both contributions to the damage nucleation mechanism warranted consideration. The mean stress consistently decreased as elements moved away from the center, and the outer region has the minus sign denoting compressional mean stress. Regardless of the sign of mean stress, the octahedral shear stress is much affected by the magnitude of mean stress. These plots offer a clear depiction of the stress states in various parts of the specimens, to be explored in greater detail in Section 1.4.2.

At a stroke of 18 mm, the overall stress states remained symmetric, albeit with some singularity points. The magnitudes of mean stress and octahedral shear stress remained significant, especially around the center, indicating concentrated stress. Conversely, at the specimen's edge, the magnitudes of mean stress and octahedral shear stress increased rapidly due to the expanding contacting area between the specimens and dies, a result of the heightened reaction force from the drawing effect.

In the final stage at a stroke of 27 mm, it became evident that areas with both large mean stress and octahedral shear stress, such as elements around the center and those near the edge, lost their symmetry, indicating non-uniform deformation. This observation aligns with findings from experiments and simulations, confirming that, at this stage, deformation becomes asymmetric. As stress states reach elevated levels, the adhesive effect diminishes, and the adhesive layer fails to maintain the symmetry and uniform deformation of the two bonded plates. Consequently, the asymmetry of stress states reflects asymmetrical deformation, with stress concentrating on one side of the specimens, leading to local deformation and necking. These discussions on stress states provide robust evidence supporting the estimation of the adhesive effect from the experimental results discussed in Section 4.3.

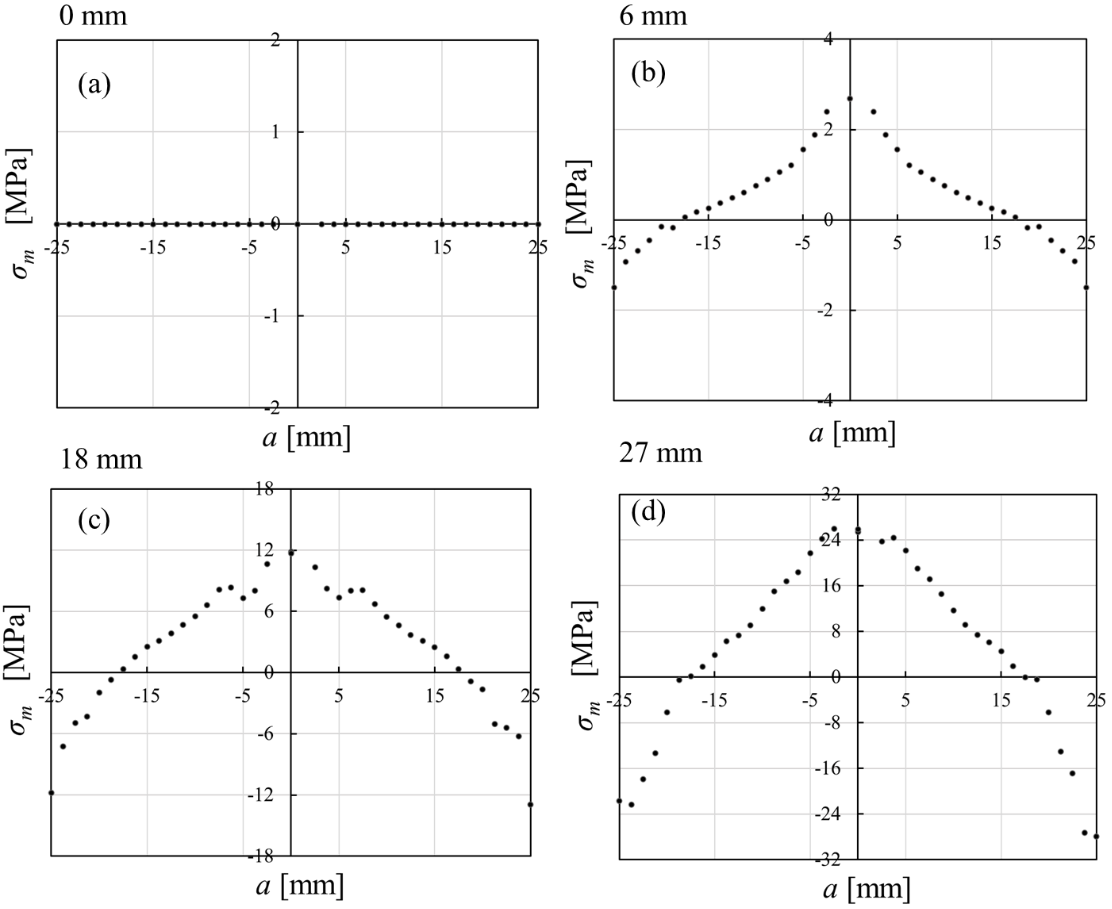

Fig 5.25 The mean stress of the elements plotted with their distance of the center in the radial direction.

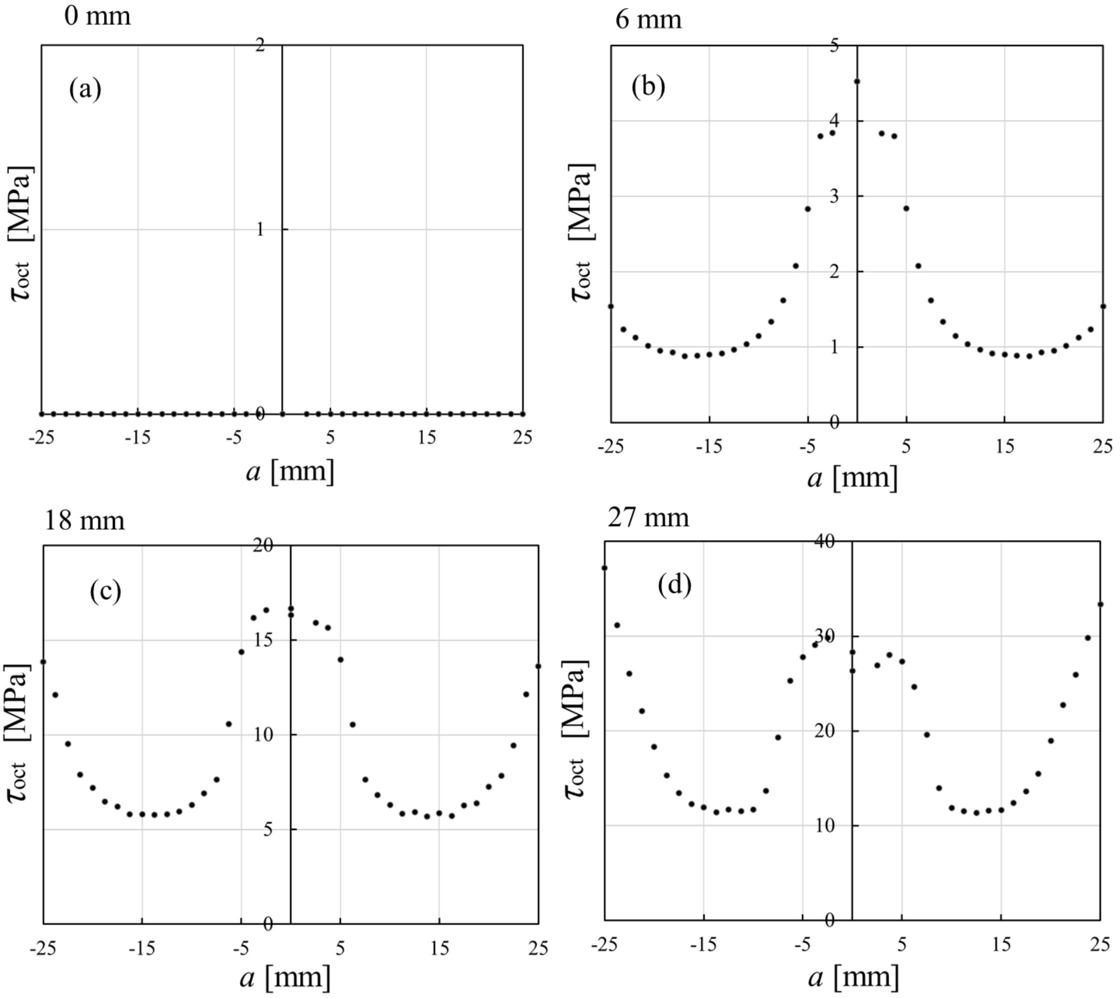
0 mm

6 mm

18 mm

27 mm

Fig 5.26 The octahedral shear stress of the elements plotted with their distance of the center in the radial direction.

5.4.2. Stresses correlated with their positions

One of the salient features of conical cup testing lies in its intricate combination of various deformation types. Consequently, the stress state at the 18 mm stroke (Fig. 5.24 (c)) stands as representative of conical cup testing, embodying the complex deformations inherent in this stage. To decipher the typical stress distribution within the specimens during conical cup testing, the stress state of each element was correlated with its position in the radial direction sequence, as depicted in Fig. 5.27.

The stress states of all elements were classified into five groups, each corresponding to a distinct area of the specimens along the radial direction. Group A encompassed elements in the upper right section of the plots, signifying elements experiencing both high shear stress and stretching normal stress. These elements, located at the center of the adhesive layer, are directly connected to the punch, resulting in elevated shear and normal stresses due to elongation deformation by the punch.

Group B comprised elements in the upper left section of the plots, indicating elements undergoing both high shear stress and compressional normal stress (σ_m is negative). These elements, situated at the outer edge, are in direct contact with the dies, leading to substantial shear and normal stresses induced by the drawing forces applied by the dies.

Groups C and D included elements close to the center or edges that do not make direct contact with the punch or dies but are still influenced by the drawing forces. Consequently, these elements experience relatively large shear stress and normal stress, albeit smaller than those in Group A or Group B.

Finally, Group E consisted of the remaining elements experiencing both small shear and normal stress. These elements occupy the middle area between the center and edge of the specimens. Given their distance from both the center and edge, the stretching force and drawing forces applied by the punch and dies have a limited impact on them, resulting in a comparatively small stress state.

This nuanced distribution of stress states, corresponding to the arrangement of elements, aids in comprehending how the stress state evolves during conical cup testing. Moreover, it facilitates the identification of locations where stress concentration occurs, offering valuable insights for predicting areas with high stress where failures may potentially manifest.

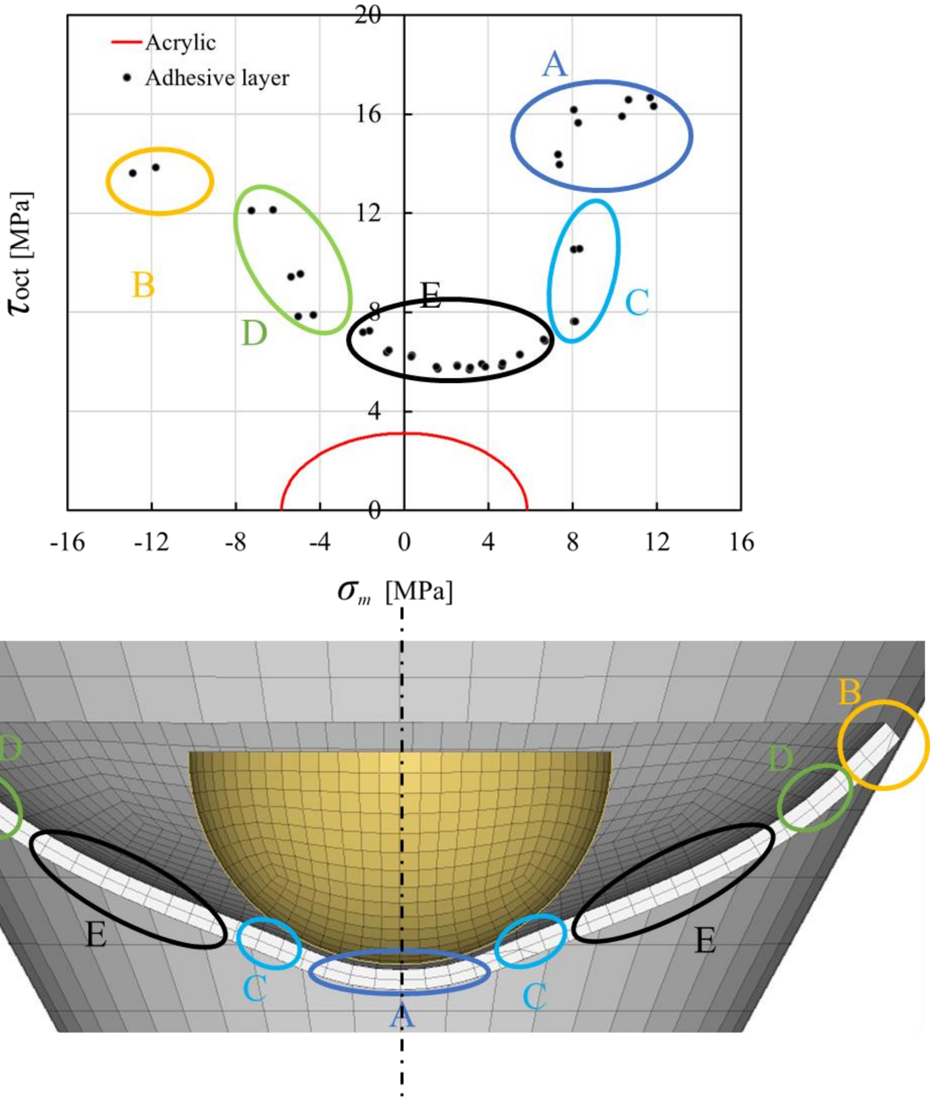

Fig 5.27 The 5 groups of the stress state of each element in adhesive layer in the σ_m and τ_{oct} plane correlated with the position in the radial direction sequence in specimens.

5.4.3. Distribution of all elements in adhesive layer

The stress state of representative elements within the adhesive layer, analyzed along the radial direction at significant strokes during conical cup testing, has been scrutinized in Sections 5.4.1 and 5.4.2 to elucidate the adhesive layer's typical behavior. However, for a more comprehensive understanding of the adhesive layer's behavior and mechanism within layered laminates, it is imperative to delve into the stress states of all elements in the adhesive layer with a finer granularity of stroke increments.

As a result, the mean stress (σ_m) and octahedral shear stress (τ_{oct}) of all elements in the adhesive layer in the model of single-layered A5052 specimens bonded by acrylic adhesive were calculated as Section 5.4.1 and plotted into the σ_m and τ_{oct} plane with failure criterion curve of acrylic adhesive. The stress states were assessed at intervals of 3 mm strokes, ranging from 0 mm to 27 mm, with their corresponding positions on the load-displacement curves depicted from Fig. 5.28 to Fig. 5.32.

In the strokes with small magnitudes, corresponding to the initial phases of the conical cup testing from 0 mm to 9 mm (Fig. 5.28), the stress states are relatively modest, and the majority of elements are positioned within the failure curve, signifying elastic deformation. This interval corresponds to the first phase, as delineated in Section 4.2 and 5.3, characterized by elongation deformation and primarily influenced by the punch force. Consequently, stress values increase gradually with the progression of strokes. The overall distribution of elements remains stable and regular, indicating that the adhesive, along with the bonded laminates, undergoes stable and symmetric deformation during this phase. Notably, between strokes 3 mm and 6 mm, elements commence exceeding elastic limits, signifying a transition from elastic to plastic deformation. To pinpoint the exact stroke where adhesive layer deformation surpasses elastic limits, a finer step of 0.5 mm was introduced from 4 mm, as depicted in Fig. 5.29. At 5 mm stroke, all elements still fall within the failure curve, while at 5.5 mm stroke, elements begin to breach the failure curve boundaries.

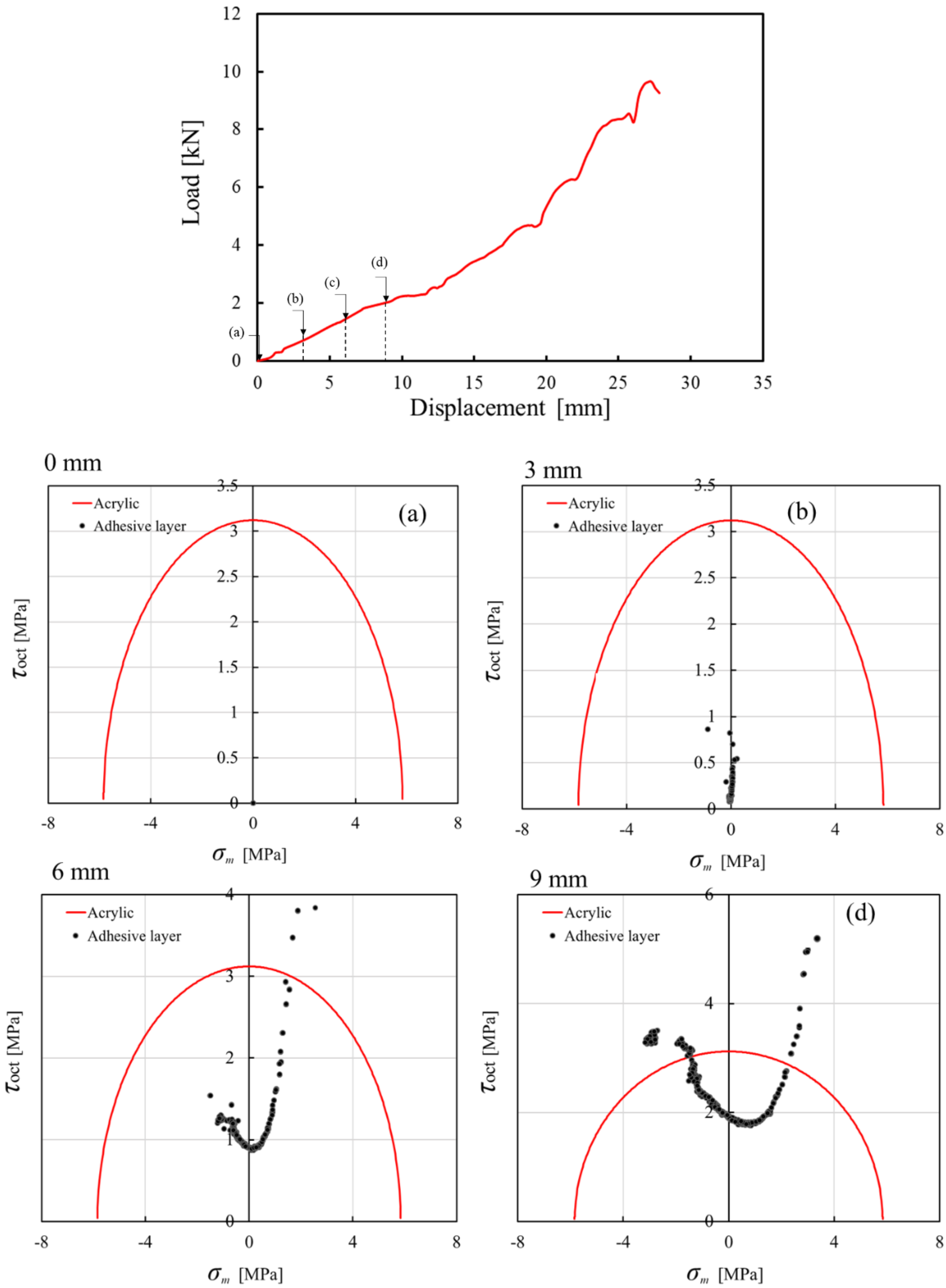

Fig. 5.28 Stress states of all elements in the σ_m and τ_{oct} plane with the failure criterion curve of acrylic adhesive with their corresponding positions during the simulation. (a) 0 mm, (b) 3 mm, (c) 6 mm, (d) 9 mm.

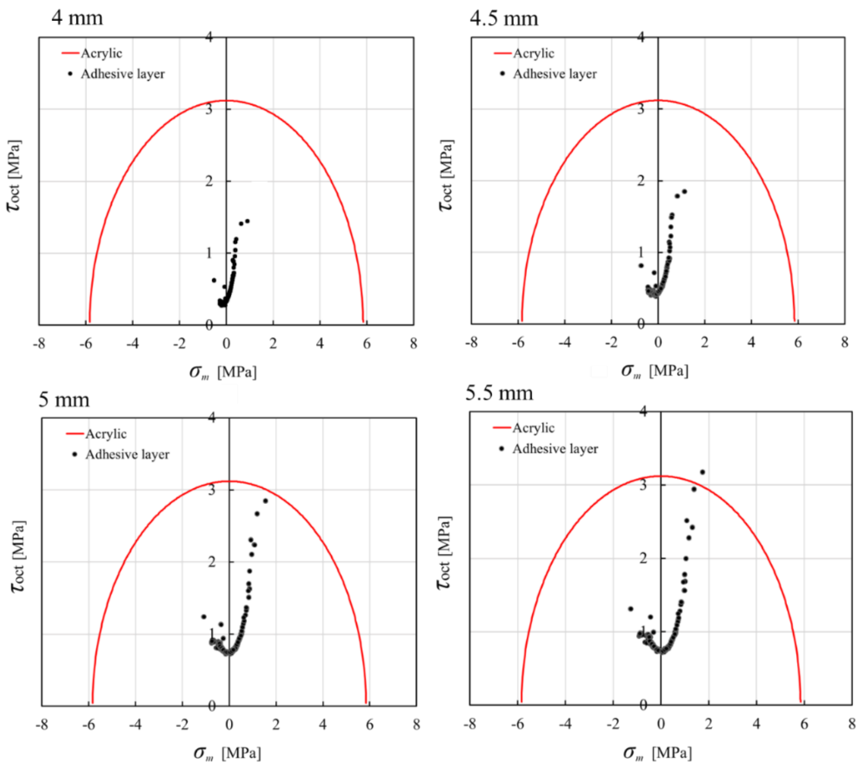

Fig. 5.29 Stress states of all elements in the σ_m and τ_{oct} plane with the failure criterion curve of acrylic adhesive at strokes 4 mm to 5.5 mm for 0.5 mm intervals.

During the strokes ranging from 12 mm to 21 mm (Fig. 5.30), which constitute the intermediate stages of the conical testing and mark the transition from phase 1 to phase 2, the deformation patterns undergo a shift. In phase 2, the drawing force exerted by the dies intensifies, coinciding with an expansion in the contact surface area between the specimen and dies. Consequently, both shear stress and normal stress experience rapid escalation, with all elements surpassing elastic limits by the 15 mm stroke. The overall distribution of elements remains relatively stable until the 18 mm stroke, beyond which the previously settled elements exhibit a trend toward dispersion. To pinpoint the precise stroke at which all elements breach the elastic limits, a finer stroke interval of 0.5 mm was employed from 12 mm, as illustrated in Fig. 5.31. By the 13 mm stroke, elements with the smallest shear stress had already exceeded the failure curve, signifying that the deformation of all elements in the adhesive layer had surpassed elastic limits.

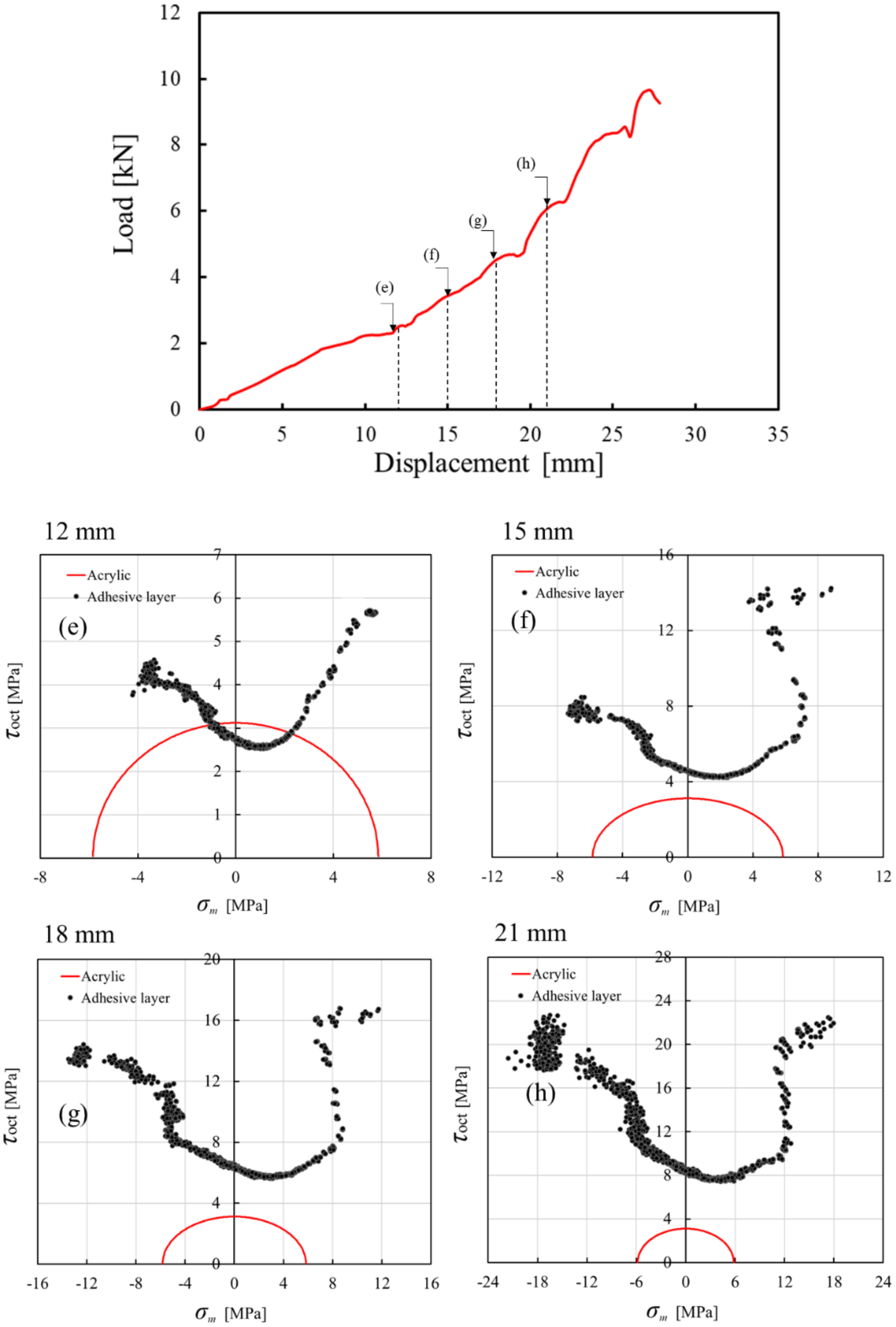

Fig. 5.30 Stress states of all elements in the σ_m and τ_{oct} plane with the failure criterion curve of acrylic adhesive with their corresponding positions during the simulation. (e) 12 mm, (f) 15 mm, (g) 18 mm, (h) 21 mm.

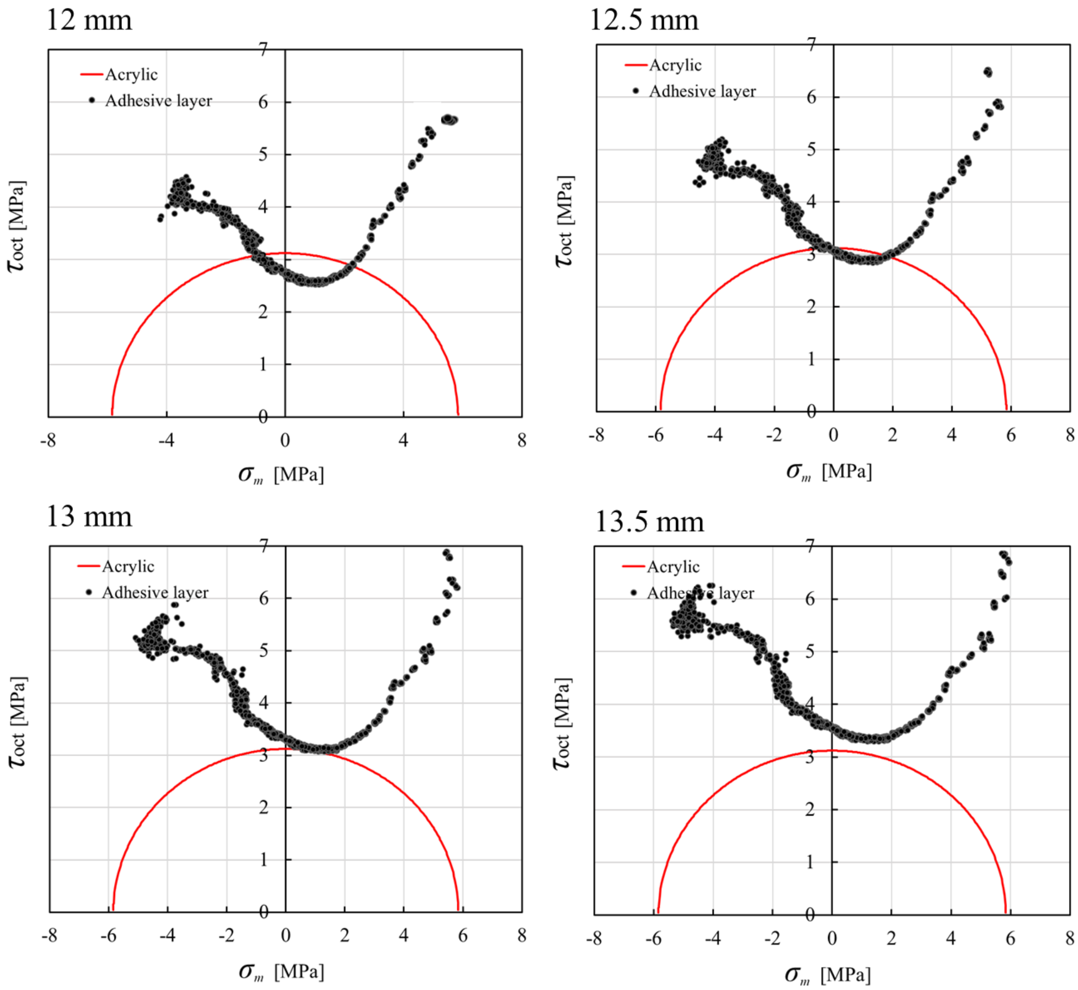

Fig. 5.31 Stress states of all elements in the σ_m and τ_{oct} plane with the failure criterion curve of acrylic adhesive at strokes 12 mm to 13.5 mm for 0.5 mm intervals.

In the final stage of the conical cup testing, with strokes ranging from 24 mm to 27 mm (Fig. 5.32), the stress states attain significantly high levels, and the distribution of elements becomes noticeably disordered, particularly among those elements situated at the left top sides of the plane. Referring to Fig. 5.27, these elements correspond to those positioned around the edges, in direct contact with the dies. The discernible trend of elements around the edges indicates that stress states are becoming unstable, leading to asymmetrical deformation around the edges. This phenomenon is attributed to the adhesive near the edges experiencing substantial shear and normal stress, compromising the bonding effect. Consequently, the top and bottom laminates fail to deform uniformly, resulting in localized deformation. At the top right side of the plane, where both shear stress and normal stress levels are elevated, stress concentration occurs at the central area in direct contact with the punch. This concentration diminishes the bonding effect of the adhesive, leading to local necking in the top and bottom laminates and eventual crack formation. The outcomes of the stress state analysis in the simulation align with the observations from the experimental results discussed in Section 4.3.

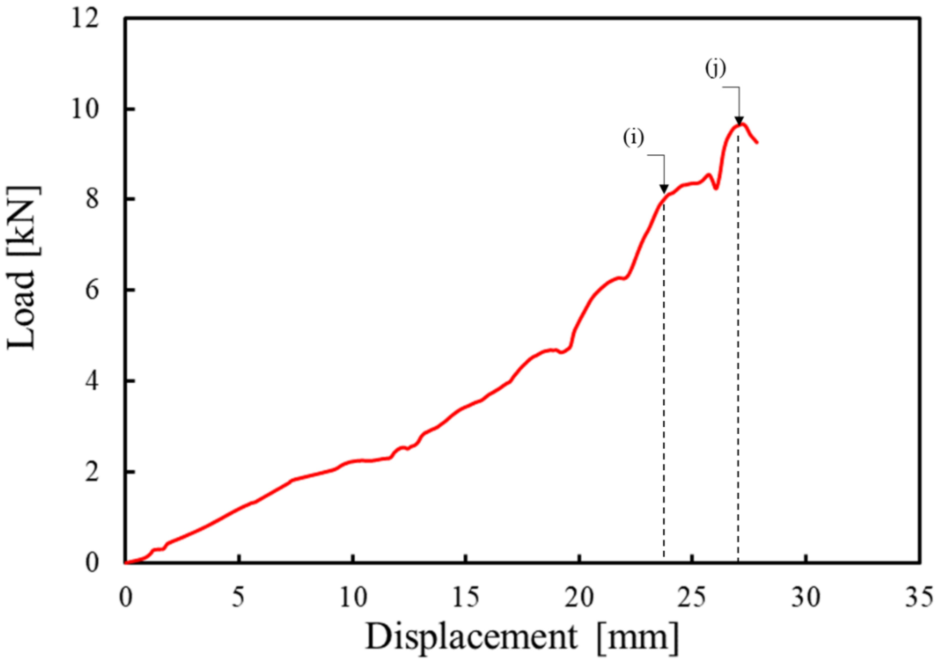

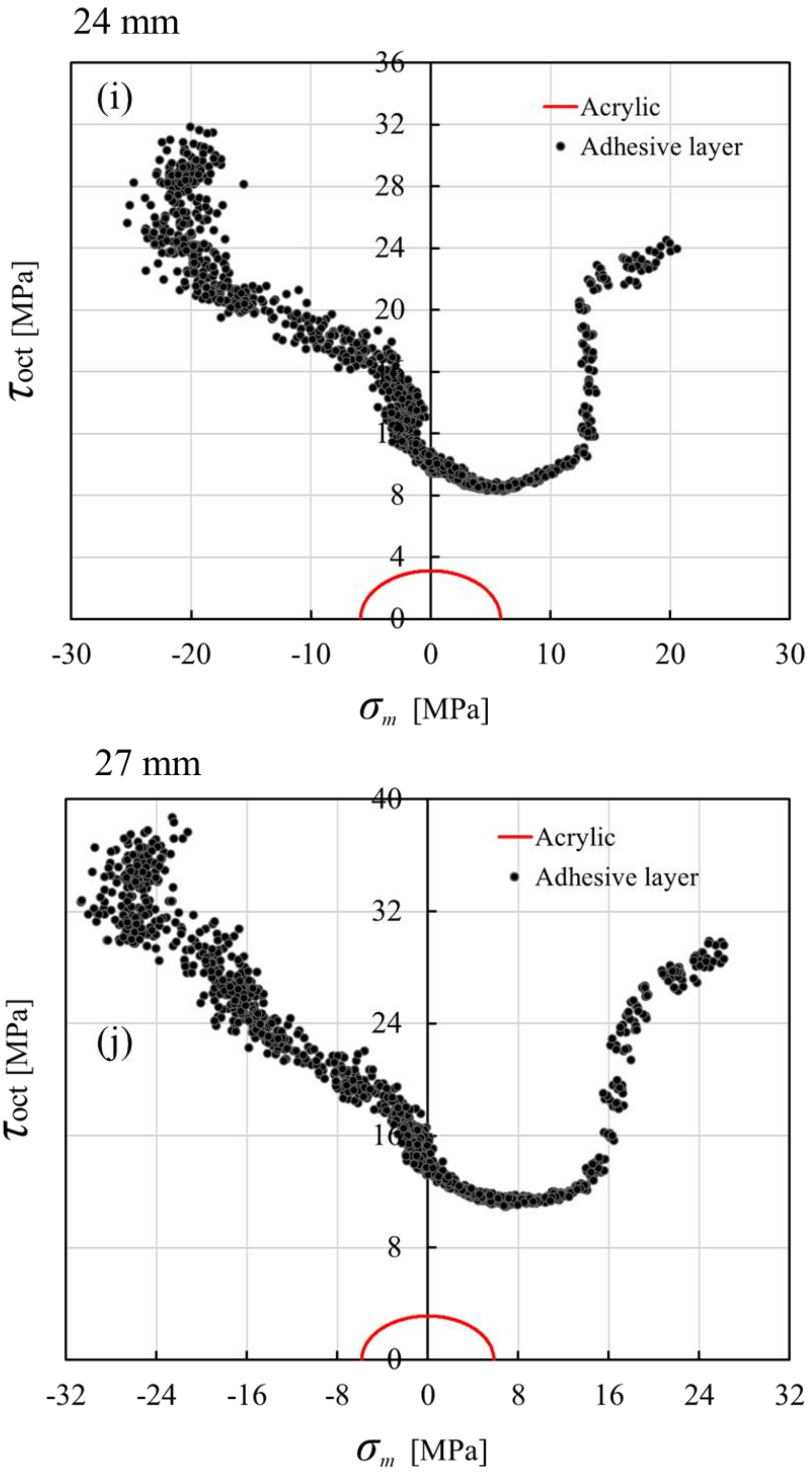

Fig. 5.32 Stress states of all elements in the σ_m and τ_{oct} plane with the failure criterion curve of acrylic adhesive with their corresponding positions during the simulation. (i) 24 mm and (j) 27 mm.

5.5. Conclusion

In this chapter, a comprehensive comparison analysis between conical testing and the FEM simulation was conducted, employing jig models with identical dimensions to the real testing apparatus. FEM models of specimens were meticulously designed, and their applicability was extensively discussed. The shell-solid model emerged as the most suitable for this research, providing the capability to scrutinize the adhesive effects of layered specimens within an acceptable running time. Additionally, the shell-beam model proved to be a suitable simplified alternative for the analysis of load-displacement relations in a large number of specimens, facilitating substantial time saving.

To ensure the accuracy of our analysis, material properties for the metals (aluminum and SPCC) utilized in the FEM analysis were sourced from specimens identical to those used in experimental tests and compared with data from reference sources. A detailed comparative analysis encompassing different specimen types—unitary, single-material-layered, and multi-material-layered—was conducted. The simulation results and comparative analyses of unitary A5052 specimens of 0.6 mm and 1.2 mm, single-layered A5052 specimens, and multi-layered specimens demonstrated consistent alignment with experimental outcomes. Thus, the simulation results and comparisons substantiate the conclusion that asymmetric deformation contributes to the loss of stability.

To gain deeper insights into the behavior of the adhesive layer during conical cup testing, stress state data of the elements in the adhesive layer were plotted onto the failure criterion curves, as detailed in Chapter 2. The stress states of the elements were further analyzed by plotting them against their distance from the center of the circular specimens. The outcomes verified the complex stress states in the adhesive layer which is essential in the real industry and reveal a notable trend: as the stress states reach higher levels, the deformation becomes asymmetric, signifying a diminished impact of the adhesive layer. The analysis elucidated the adhesive layer's behavior, aiding in identifying the performance of different parts within the adhesive layer. The distribution of elements in the stress plane became unstable and discrete in the later stages of conical cup testing, validating experimental discussions that the adhesive promotes uniform deformation of the top and bottom laminates while inhibiting local deformation. Notably, the stress concentration of elements in specific areas emerged as crucial observations for predicting locations prone to crack formation.

In conclusion, the simulation proves to be a valuable tool and method, facilitating the examination of approachable features of experiments and corroborating the established verdicts derived from real testing.

6. Conclusion

To address the pressing need for reducing CO2 emissions and energy consumption, the weight reduction of transportation equipment has become a pivotal objective. This necessitates the adoption of multi-material structures, with bonding dissimilar materials emerging as a crucial aspect of this endeavor. Adhesion, as a versatile method for joining various dissimilar materials, holds promise for constructing multi-material structures. Ensuring the strength of the bonded area is of utmost importance. The strength of bonded structures is influenced by both material and structural factors, necessitating a co-design process that considers both the strength of adhesive materials under multi-axis states and the shape of the bonded interface. In the automotive sector, there is a noticeable trend towards the substantial utilization of metal laminates in body construction. This not only facilitates diverse designs for automobile frames but also opens the door to significant weight reduction through the incorporation of bonded metal laminates made of multiple materials.

The initial phase of this study involves an investigation to uncover the disparities in shape optimization for different adhesives. This is accomplished by employing failure criteria obtained through the evaluation of pipe specimens, which simulate multi-axial stress states using uniaxial tensile testing. In the latter part of the research, the primary objective is to conduct a comprehensive evaluation of the plastic formability of multi-layered metal structures. Reference to unitary metal sheets serves as a benchmark to assess the influence of adhesives and ascertain the viability of implementing multi-layered configurations. This exploration aims to pave the way for the seamless integration of such configurations into industrial production processes.

The conclusions drawn from each chapter are summarized as follows:

In Chapter 1, the focus was on the study of multi-material structures, particularly in the context of automobiles which provided an overview of joining technologies for different materials with the aim of achieving multi-material structures. It highlighted adhesion as a promising joining technology for the future. The co-design process of adhesive-bonded structures was thoroughly reviewed, emphasizing its comprehensive nature. The chapter also discussed the advantages of bonded metal laminates and underscores the importance of evaluating the plastic formability of such laminates. Limitations of conventional testing methods were explored, and the chapter outlines the requisites for establishing proper testing methodologies. Additionally, the chapter elucidated the objectives and purposes of the study, providing an organizational framework for the paper.

In Chapter 2, the failure function of the epoxy adhesive was derived through tensile testing employing pipe specimens with an inclined cutting surface, allowing for the assessment of a multiaxial stress state at the adhesive interface. A comparative analysis was conducted by juxtaposing the obtained failure function of the epoxy adhesive with the failure function of acrylic adhesives. The epoxy adhesive displayed higher strength overall, particularly in response to hydrostatic pressure, where it significantly surpassed the strength of acrylic adhesive. Notably, a non-zero peak in the failure function of the epoxy adhesive prompted a reformulation shedding light on the influence of hydrostatic pressure on the maximum distortional strength of the adhesive material. Subsequently, a power law specific to the epoxy adhesive was established and juxtaposed with its acrylic counterpart to investigate the thickness dependence of the adhesives showing that if the appropriate h^* is chosen, the multi-material failure curve can be transferred to keep identical with the single-material one which means they have the same property.

In Chapter 3, a shape optimization problem was devised, considering distinct failure functions for diverse adhesive materials. Throughout the optimization, a noteworthy trend emerged: the design data points' distances from the origin within the failure plane diminished progressively, showcasing the efficacy of the optimization in minimizing the objective function. Upon attaining optimized configurations, it became evident that these refined shapes could substantially reduce applied stress levels underscoring the substantial improvement in the mechanical integrity of the adhesive layer facilitated by these final shapes. The driving force behind the geometric transformations in the adhesive layer is encapsulated by the shape gradient function which plays a pivotal role in governing the adhesive layer's response to mean stress and shear stress. Notably, the shapes of the adhesive layers remain unchanged for epoxy adhesive when $\alpha = 0$ and for acrylic adhesive when α approaches infinity. This characteristic serves as a valuable indicator, highlighting the suitability of the initial model for multi-material design endeavors.

In Chapter 4, a pioneering approach involving multi-layered laminates bonded by adhesive, coupled with specialized conical cup testing, was implemented encompassing unitary and single/multi-layered configurations of different materials. Comparative analyses revealed intriguing trends, particularly in unitary and single-layered specimens with identical thickness. Bonding substantially improved formability, attributed to the inhibitory effect on surface roughness, facilitating uniform deformation and enhancing plastic formability. Comparative analyses involving multi-layered specimens of A5052 and SPCC against unitary and single-layered counterparts demonstrated the substantial influence of adhesives on weight reduction through multi-materialization. The formability of multi-layered specimens significantly improved, with a 40% and 35% increase in the forming limit for A5052 and SPCC, accompanied by a commendable 33% weight reduction compared to unitary SPCC of the same thickness. These findings highlight the constructive influence of bonded multi-layer structures, holding promise for weight reduction in diverse applications without compromising structural integrity.

In Chapter 5, a thorough comparison analysis between conical testing and FEM simulation was undertaken, employing jig models mirroring the real testing apparatus. Meticulously designed FEM models, primarily the shell-solid model, demonstrated superior suitability, enabling scrutiny of adhesive effects within an acceptable runtime. A detailed comparative analysis spanning unitary, single-material-layered, and multi-material-layered specimens affirmed consistent alignment between simulation results and experimental outcomes. This substantiated the conclusion that asymmetric deformation contributes to stability loss. Delving into the adhesive layer's behavior during conical cup testing, stress state data were plotted onto failure criterion curves and further analyzed by plotting them against their distance from the center of the circular specimens. This analysis verified the complex stress states in the adhesive layer which is essential in the real industry and revealed the adhesive layer's role in promoting uniform deformation while inhibiting local deformation. Stress concentration in specific areas provided critical insights for predicting crack-prone locations. Thus, the simulation emerges as a valuable tool, facilitating the examination of experimentally approachable features and reinforcing established conclusions derived from real testing.

In conclusion, this study delved into a co-design process, optimizing the shapes of adhesive-bonded structures based on a failure criterion derived from experiments that considered both material and structural factors. The optimized shapes achieved a significant reduction in applied stress levels, emphasizing a notable enhancement in the mechanical integrity of the adhesive layer. The analyses of experimental and FEM simulation results for single- and multi-layered specimens, in comparison with unitary specimens, provided robust evidence of the adhesive's impact in amplifying the formability of bonded laminates. This underscores the positive influence of bonded multi-layer structures, offering promise for weight reduction across diverse applications without compromising structural integrity.

Appendix 1: The properties of adhesives

The properties of both epoxy and acrylic adhesives used in this research were obtained from the testing performed by Kobe Material Testing Laboratory. The specimens were made from the same adhesive materials applied to the bonded laminates and the testing were performed under different loading speed 0.03 mm/s and 0.003 mm/s representing different strain rates 3×10^{-3} /s and 3×10^{-4} /s. The specimens were cut off from the solid made from the adhesives as shown in Fig. A1. The nominal stress-strain curves and true stress-strain curves of the epoxy adhesive (EP-171, CEMEDINE Co., Ltd.) with different strain rates are shown in Figs. A3 and A4, respectively. The nominal stress-strain curves and the true stress-strain curve of the acrylic adhesive (HardlocTM: M-600-08, Denka Co., Ltd.) are shown in Figs. A5 and A6, respectively. The material properties, including Young's modulus, 0.2% yield stress, tensile stress and elongation, were obtained and listed in Table A1. For epoxy adhesives, the values were obtained from the average value of all the testing data as it doesn't show the dependence on the strain rate while for acrylic, as it is dependent to the strain rate, the values were obtained for different strain rate. According to the results, both adhesives have relatively clear elastic behavior. As a result, the properties of the adhesive layers in the simulation model were set as elastic.

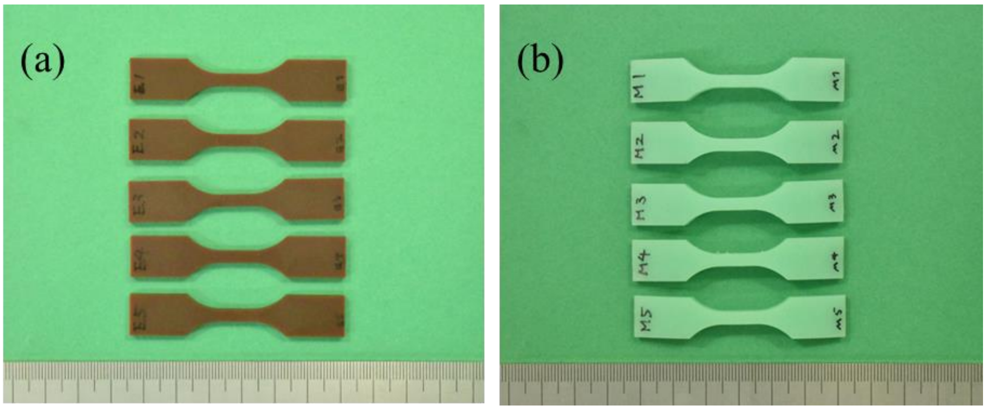

Fig. A1 The specimens made from adhesive. (a) Epoxy (EP-171, CEMEDINE Co., Ltd.) and (b) Acrylic (HardlocTM: M-600-08, Denka Co., Ltd.).

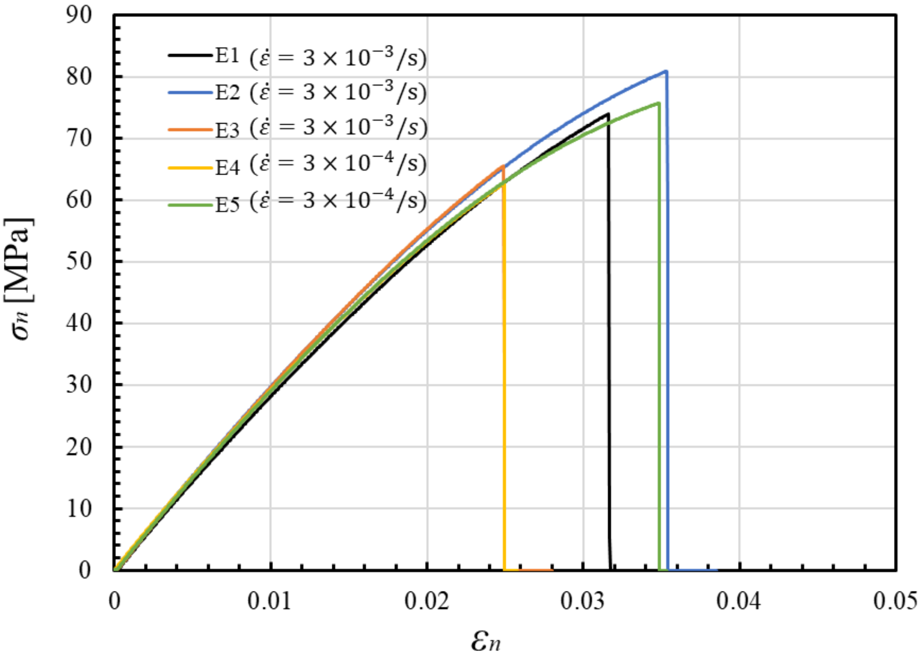

Fig. A2 The nominal stress and strain curve for the epoxy adhesive (EP-171, CEMEDINE Co., Ltd.).

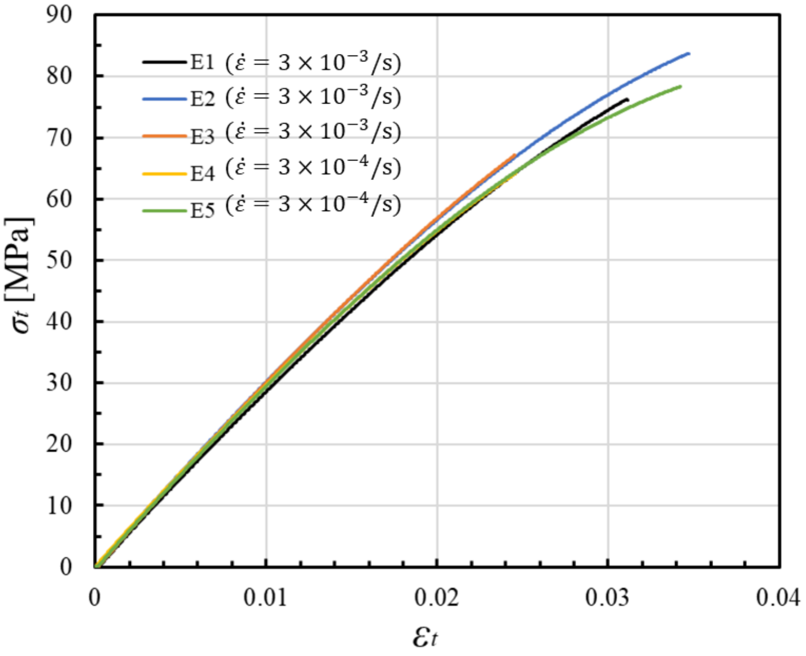

Fig. A3 The true stress and strain curve for the epoxy adhesive (EP-171, CEMEDINE Co., Ltd.).

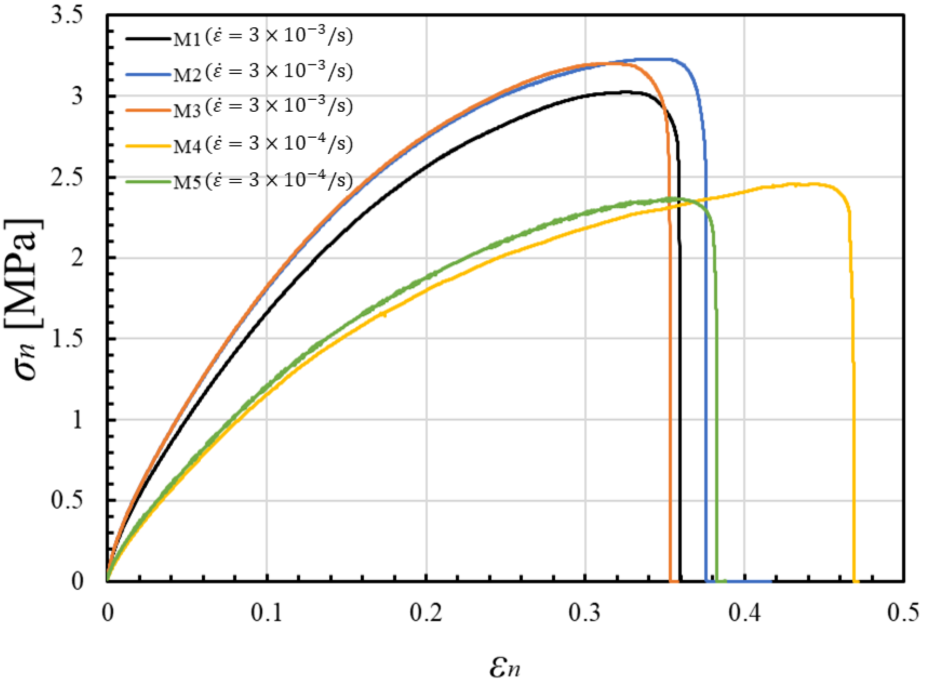

Fig. A4 The nominal stress and strain curve for the acrylic adhesive (HardlocTM: M-600-08, Denka Co., Ltd.).

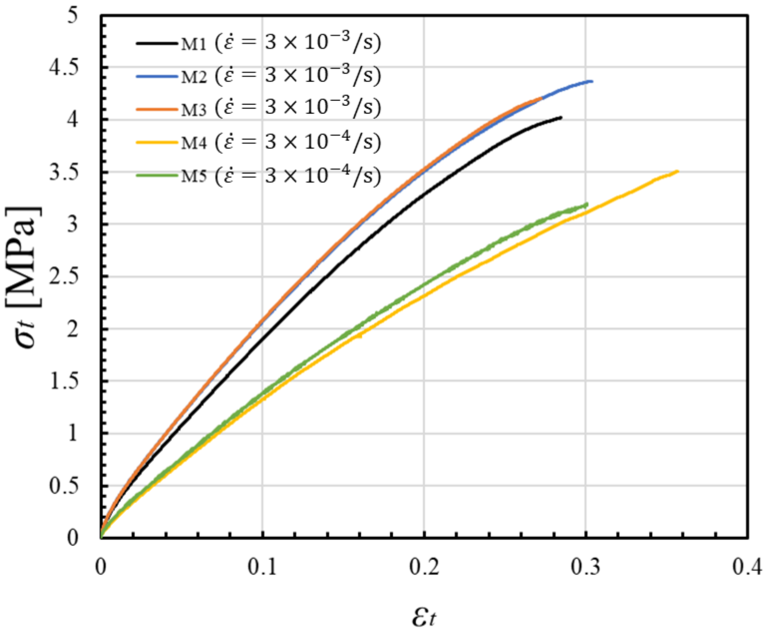

Fig. A5 The true stress and strain curve for the acrylic adhesive (HardlocTM: M-600-08, Denka Co., Ltd.).

Table A1 The material properties of the epoxy and acrylic adhesives

Material		Young's modulus [MPa]	0.2% Yield Stress [MPa]	Tensile Stress [MPa]	Elongation [%]
Epoxy (EP171)		2820	51.6	71.7	3.03
Acrylic (M-600-08)	$\dot{\varepsilon} = 3 \times 10^{-3}/s$	182	0.201	3.14	33.5
	$\dot{\varepsilon} = 3 \times 10^{-4}/s$	141	0.108	2.41	38.5

Reference

[1] United Nations Climate Change https://unfccc.int/event/cop-21

[2] International Energy Agency, CO2 Emission in 2022, https://iea.blob.core.windows.net/assets/3c8fa115-35c4-4474-b237-1b00424c8844/CO2Emissionsin2022.pdf

[3] Ministry of Land, Infrastructure, Transport, and Tourism, https://www.mlit.go.jp/sogoseisaku/environment/sosei_environment_tk_000007.html (accessed on 17th May 2023).

[4] European Parliament, CO2 emission standards for new cars and vans, https://www.europarl.europa.eu/RegData/etudes/BRIE/2022/698920/EPRS_BRI(2022)698920_EN.pdf

[5] Ministry of Land, Infrastructure, Transport, and Tourism, https://www.mlit.go.jp/jidosha/content/001337988.pdf (accessed in Mar. 2020).

[6] 兵藤知明, 岸輝雄, “自動車のマルチマテリアル化とその技術戦略”, 藤本雄一郎, 漆山雄太監修, 自動車のマルチマテリアル戦略, 株式会社エヌ・ティー・エス, (2017), pp. 3-9.

[7] 藤本雄一郎, “欧州におけるマルチマテリアル・異材接合の動向と国内メーカの対応策”, 藤本雄一郎, 漆山雄太監修, 自動車のマルチマテリアル戦略, 株式会社エヌ・ティー・エス, (2017), pp. 11-17.

[8] ISMA website, http://isma.jp

[9] Goede, M., Stehlin, M., Rafflenbeul, L., Kopp, G. and Beeh, E., “Super Light Car—lightweight construction thanks to a multi-material design and function integration”, European Transport Research Review, Vol. 1, No. 1 (2009), pp. 5-10.

[10] Martinsen, K., Hu, S. J. and Carlson, B. E., “Joining of dissimilar materials”, CIRP Annals, Vol. 64, No. 2 (2015), pp. 679-699.

[11] 三瓶和久, “自動車メーカにおけるマルチマテリアル化 ~日本の自動車メーカの適用例を中心に~”, 藤本雄一郎, 漆山雄太監修, 自動車のマルチマテリアル戦略, 株式会社エヌ・ティー・エス, (2017), pp. 91-99.

[12] 鈴木励一, “接合技術の現状から将来展望まで”, 藤本雄一郎, 漆山雄太監修, 自動車のマルチマテリアル戦略, 株式会社エヌ・ティー・エス, (2017), pp. 115-127.

[13] Hino, M., Mitooka, Y., Murakami, K., Urakami, K., Nagase, H. and Kanadani, T., “Effect of aluminum surface state on laser joining between 1050 aluminum sheet and polypropylene resin sheet using insert materials” Materials transactions, Vol. 52, No. 5 (2011), pp. 1041-1047.

[14] Katayama, S. and Kawahito, Y., “Laser direct joining of metal and plastic”, Scripta materialia, Vol. 59, No. 12 (2008), pp. 1247–1250.

[15] 三瓶和久, “異種材料のレーザ接合技術”, 藤本雄一郎, 漆山雄太監修, 自動車のマルチマテリアル戦略, 株式会社エヌ・ティー・エス, (2017), pp. 129-137.

[16] 二宮崇, 上向賢一, “レーザ溶接 / 摩擦撹拌接合技術によるチタン合金接合技術”, 藤本雄一郎, 漆山雄太監修, 自動車のマルチマテリアル戦略, 株式会社エヌ・ティー・エス, (2017), pp. 173-178.

[17] 永塚公彬, 中田一博, “金属 / CFRP 異材抵抗スポット溶接技術”, 藤本雄一郎, 漆山雄太監修, 自動車のマルチマテリアル戦略, 株式会社エヌ・ティー・エス, (2017), pp. 139-147.

[18] Mortazavi, S. N., Marashi, P., Pouranvari, M. and Masoumi, M., “Investigation on joint strength of dissimilar resistance spot welds of aluminum alloy and low carbon steel”, In Advanced Materials Research, Trans Tech Publications, Vol. 264, (2011), pp. 384-389.

[19] Liyanage, T., Kilbourne, J., Gerlich, A. P., and North, T. H., “Joint formation in dissimilar Al alloy/steel and Mg alloy/steel friction stir spot welds, Science and Technology of Welding and Joining”, Vol. 14, No. 6 (2009), pp. 500–508.

[20] Amancio-Filho, S. T., Bueno, C., Dos Santos, J. F., Huber, N. and Hage Jr, E., “On the feasibility of friction spot joining in magnesium/fiber-reinforced polymer composite hybrid structures”, Materials Science and Engineering: A, Vol. 528, Nos. 10-11 (2011), pp. 3841-3848.

[21] Yusof, F., Miyashita, Y., Seo, N., Mutoh, Y. and Moshwan, R., “Utilising friction spot joining for dissimilar joint between aluminium alloy (A5052) and polyethylene terephthalate”, Science and Technology of Welding and Joining, Vol. 17, No. 7 (2012), pp. 544-549.

[22] 杉本幸弘, 西口勝也, 田中耕二郎, “摩擦熱による異種材料接合技術”, 藤本雄一郎, 漆山雄太監修, 自動車のマルチマテリアル戦略, 株式会社エヌ・ティー・エス, (2017), pp. 101-108.

[23] 行武栄太郎, “摩擦攪拌接合技術による難燃性マグネシウム合金接合技術”, 藤本雄一郎, 漆山雄太監修, 自動車のマルチマテリアル戦略, 株式会社エヌ・ティー・エス, (2017), pp. 153-160.

[24] 福田敏彦, “摩擦攪拌接合技術によるアルミニウム合金接合技術”, 藤本雄一郎, 漆山雄太監修, 自動車のマルチマテリアル戦略, 株式会社エヌ・ティー・エス, (2017), pp. 161-172.

[25] Meschut, G., Janzen, V. and Olfermann, T., “Innovative and highly productive joining technologies for multi-material lightweight car body structures”, Journal of Materials Engineering and Performance, Vol. 23, No. 5 (2014), pp. 1515-1523.

[26] Ling, Z., Li, Y., Luo, Z., Feng, Y. and Wang, Z., “Resistance element welding of 6061 aluminum alloy to uncoated 22MnMoB boron steel”, Materials and Manufacturing Processes, Vol. 31, No. 16 (2016), pp. 2174-2180.

[27] Rohde, M., Südmeyer, I., Urbanek, A. and Torge, M., “Joining of alumina and steel by a laser supported brazing process”, Ceramics International, Vol. 35, No. 1 (2009), pp. 333-337.

[28] Sechi, Y., Tsumura, T. and Nakata, K., “Dissimilar laser brazing of boron nitride and tungsten carbide”, Materials & Design, Vol. 31, No. 4 (2010), pp. 2071-2077.

[29] 平田好則, “NEDO/ISMA プロジェクトにおける溶接接合技術 (特集 異種材料溶接・接合の潮流)”, 溶接技術= Welding technology: 一般社団法人日本溶接協会誌, Vol. 65, No. 5 (2017), pp. 40-44.

[30] Yash, N., Ayush, G., Rohit, S., Rhea, R., Archana, Shivani, S., Shivangi K., “Microwave Welding of Metals and Non-metals (Thermo-Plastics) [Joining or welding of two Materials using microwave]”, International Journal of Scientific

Research in Engineering and Management (IJSREM), Vol. 07, No. 3 (2023).

[31] Nafikov, M.Z. and Zagirov, I.I., “Lack of fusion at the electrical contact welding of steel wires”, Welding International, Vol. 34, No. 10-12 (2020), pp. 460-464.

[32] 鈴木晴彦, “セルフピアッシングリベット技術”, 藤本雄一郎, 漆山雄太監修, 自動車のマルチマテリアル戦略, 株式会社エヌ・ティー・エス, (2017), pp. 149-152.

[33] He, X., Pearson, I. and Young, K., “Self-pierce riveting for sheet materials: state of the art. Journal of materials processing technology”, Vol. 199, Nos. 1-3 (2008), pp. 27-36.

[34] Fink, A., Camanho, P. P., Andrés, J. M., Pfeiffer, E. and Obst, A., “Hybrid CFRP/titanium bolted joints: Performance assessment and application to a spacecraft payload adaptor”, Composites Science and Technology, Vol. 70, No. 2 (2010), pp. 305-317.

[35] Abe, Y., Mori, K. and Kato, T., “Joining of high strength steel and aluminium alloy sheets by mechanical clinching with dies for control of metal flow”, Journal of materials processing technology, Vol. 212, No. 4 (2012), pp. 884-889.

[36] Lee, C. J., Kim, J. Y., Lee, S. K., Ko, D. C. and Kim, B. M., “Parametric study on mechanical clinching process for joining aluminum alloy and high-strength steel sheets”, Journal of Mechanical Science and Technology, Vol. 24, No. 1 (2010), pp. 123-126.

[37] Szlosarek, R., Karall, T., Enzinger, N., Hahne, C. and Meyer, N. “Mechanical testing of flow drill screw joints between fibre-reinforced plastics and metals” Materials Testing, Vol. 55, No. 10, (2013), pp. 737-742.

[38] 鈴木励一 “自動車のマルチマテリアル化と異材接合技術の実態: かしめ・嵌合技術の復活と発展 (特集 日本の溶接事情の今を知る 溶接を取り巻くニーズと課題)”, 溶接技術= Welding technology: 一般社団法人日本溶接協会誌, Vol. 65 No. 1 (2017), pp. 64-72.

[39] 崎山達也, 村山元, 内藤恭章, 才田健二, 宮崎康信, 及川初彦, 野瀬哲郎, “自動車ボディにおける鋼板とアルミニウム合金板との異種金属接合技術”, 新日鉄技報, Vol. 393, (2012), pp. 91-98.

[40] Min, J., Li, Y., Li, J., Carlson, B. E. and Lin, J., “Friction stir blind riveting of carbon fiber-reinforced polymer composite and aluminum alloy sheets”, The International Journal of Advanced Manufacturing Technology, Vol. 76, No. 5-8 (2015), pp. 1403-1410.

[41] Mori, K. I., Bay, N., Fratini, L., Micari, F. and Tekkaya, A. E., “Joining by plastic deformation”, CIRP Annals, Vol. 62, No. 2 (2013), pp. 673-694.

[42] Jack, R. V., “Mechanical fastening of polymer composites”, Polymer Engineering and Science, Vol. 29, No. 19 (1989), pp. 1332-1339.

[43] 佐藤千明, “自動車構造用接着接合技術の最新動向”, 鋳造工学, Vol. 83, No. 12 (2011), pp. 738-742.

[44] Kawasaki, S., Nakajima, G., Haraga, K., and Sato, C., “Functionally graded adhesive joints bonded by honeymoon adhesion using two types of second generation acrylic adhesives of two components”, The Journal of Adhesion, Vol. 92, Nos. 7-9 (2016), pp. 517–534.

[45] 山根健, “BMWにおけるマルチマテリアル化と接着・接合技術の将来展望”, 藤本雄一郎, 漆山雄太監修, 自動車のマルチマテリアル戦略, 株式会社エヌ・ティー・エス, (2017), pp. 109-114.

[46] 佐藤千明, “マルチマテリアル化を支える接着接合技術” , 藤本雄一郎, 漆山雄太監修, 自動車のマルチマテリアル戦略, 株式会社エヌ・ティー・エス, (2017), pp. 215-224.

[47] 多賀康訓, “マルチマテリアル化を支える界面制御技術”, 藤本雄一郎, 漆山雄太監修, 自動車のマルチマテリアル戦略, 株式会社エヌ・ティー・エス, (2017), pp. 115-127.

[48] 杉村博之, “高分子と金属の光活性化接合技術”, 藤本雄一郎, 漆山雄太監修, 自動車のマルチマテリアル戦略, 株式会社エヌ・ティー・エス, (2017), pp. 115-127.

[49] Smith, S., Vrenken, J., & van der Veldt, T., “Structural performance of adhesive and weld-bonded joints in AHSS”, Welding in the World, Vol. 57, No. 1 (2013), pp. 147-156.

[50] Sun, X., Stephens, E. V. and Khaleel, M. A., “Fatigue behaviors of self-piercing rivets joining similar and dissimilar sheet metals”, International journal of fatigue, Vol. 29, No. 2 (2007), pp. 370-386.

[51] Smith, B., Spulber, A., Modi, S., Fiorelli, T., “Technology Roadmaps: Intelligent Mobility Technology, Materials and Manufacturing Processes, and Light Duty Vehicle Propulsion”, Center for Automotive Research, (2017)

[52] Colin H, S. Dennis E, M. and Neil, P., *Manual of Engineering Drawing (Fifth Edition),* 547-560 (2020).

[53] Weisbrodt, M., Kowalczyk, A. and Kowalczyk, K., “Structural Adhesives Tapes Based on a Solid Epoxy Resin and Multifunctional Acrylic Telomers”, Polymers, Vol. 13 (2021).

[54] Sharp, F., Bonser, T., “Epoxy resin adhesives”, International application published with international search report (published on 18 Mar. 2021).

[55] Schlechte, J. S., “Advances in epoxy adhesives”, Advances in Structural Adhesive Bonding (Second Edition), Woodhead Publishing (2023), pp. 3-67.

[56] Kinloch, A., “J. Adhesion and Adhesives: Science and Technology”, London: Chapman and Hall, Ltd, (1987). pp. 26, 139, 365.

[57] Yohannes, L. Yaphary, Zechuan, Y., Raymond, H.W. L., David, H. and Denvid, L., “Molecular dynamics simulations on adhesion of epoxy-silica interface in salt environment”, Composites Part B: Engineering, Vol. 131 (2017), pp.165-172.

[58] JIS K6850, “Adhesives−Determination of tensile lap-shear strength of rigid-to-rigid bonded assemblies”, (1999).

[59] Ikegami, K. and Sugibayashi, T., “A method of estimating the strength of adhesive bonded joints of metals”, The Journal of Adhesion, Vol. 21, Nos. 3-4 (1987), pp. 211–227.

[60] Adams, R. D., “Strength predictions for lap joints, especially with composite adherends”, A review, The Journal of Adhesion, Vol. 30, Nos. 1-4 (1989), pp. 219–242.

[61] Pinto, A. M. G., Magalhães, A. G., Campilho, R. D. S. G., de Moura, M. F. S. F., and Baptista, A. P. M., “Single-lap joints of similar and dissimilar adherends

bonded with an acrylic adhesive", The Journal of Adhesion, Vol. 85, No. 6 (2009), pp. 351–376.

[62] JIS K6854, "Adhesives−Determination of peel strength of bonded assemblies", (1999).

[63] Kaelble, D. H., "Theory and analysis of peel adhesion: adhesive thickness effects", The Journal of Adhesion, Vol. 37, Nos. 1-3 (1992), pp. 205–214.

[64] Thouless, M. D. and Jensen, H. M., "Elastic fracture mechanics of the peel-test geometry, The Journal of Adhesion", Vol. 38, Nos. 3-4 (1992), pp. 185–197.

[65] Adams, R. D., Atkins, R. W., Harris, and J. A., Kinloch, A. J., "Stress analysis and failure properties of carbon-fibre-reinforced-plastic/steel double-lap joints", The Journal of Adhesion, Vol. 20, No. 1 (1986), pp. 29–53.

[66] da Silva, L. F., da Silva, R. A. M., Chousal, J. A. G. and Pinto, A. M. G., "Alternative methods to measure the adhesive shear displacement in the thick adherend shear test", Journal of Adhesion Science and Technology, Vol. 22, No. 1 (2008), pp. 15-29.

[67] Crocombe, A. D. and Adams, R. D. "An elasto-plastic investigation of the peel test", The Journal of Adhesion, Vol. 13, Nos. 3-4 (1982), pp. 241-267.

[68] Zhang, Y., Hazelton, D. W., Knoll, A. R., Duval, J. M., Brownsey, P., Repnoy, S., Soloveichik, S., Sundaram, A., McClure, R. B., Majkic, G., Selvamanickam, V., "Adhesion strength study of IBAD–MOCVD-based 2G HTS wire using a peel test", Physica C: Superconductivity, Vol. 473, (2012), pp. 41-47.

[69] 田中延宜, "接着剤の試験方法", 溶接学会誌, Vol. 70, No. 4 (2001), pp. 416-420.

[70] Jorgensen, G. J., Terwilliger, K. M., DelCueto, J. A., Glick, S. H., Kempe, M. D., Pankow, J. W., Pern, F. J., McMahon, T. J., "Moisture transport, adhesion, and corrosion protection of PV module packaging materials", Solar Energy Materials and Solar Cells, Vol. 90, No. 16 (2006), pp. 2739-2775.

[71] Brewer, J. C. and Lagace, P. A., "Quadratic stress criterion for initiation of delamination", Journal of composite materials, Vol. 22, No.12 (1988), pp. 1141–1155.

[72] Tsai, S. W. and Wu, E. M, "A general theory of strength for anisotropic

materials" Journal of composite materials, Vol. 5, No. 1 (1971), pp. 58-80.

[73] Drucker, D. C. and Prager, W., "Soil mechanics and plastic analysis or limit design. Quarterly of applied mathematics", Vol. 10, No. 2 (1952), pp. 157-165.

[74] Mahnken, R. and Schlimmer, M., "Simulation of strength difference in elasto-plasticity for adhesive materials, International journal for numerical methods in engineering", Vol. 63, No. 10 (2005), pp. 1461–1477.

[75] Bossler, F. C., Franzblau, M. C., and Rutherford, J. L., "Torsion apparatus for measuring shear properties of adhesive bonded joints", Journal of Physics E: Scientific Instruments, Vol. 1, No. 8 (1968), pp. 829–833.

[76] Liechti, K. M. and Hayashi, T., "On the uniformity of stresses in some adhesive deformation specimens", The Journal of Adhesion, Vol. 29, Nos. 1-4 (1989), pp. 167–191.

[77] Chai, H., "Observation of deformation and damage at the tip of cracks in adhesive bonds loaded in shear and assessment of a criterion for fracture", International Journal of Fracture, Vol. 60, No. 4 (1993), pp. 311–326.

[78] Chai, H., "The effects of bond thickness, rate and temperature on the deformation and fracture of structural adhesives under shear loading, International journal of fracture", Vol. 130, No. 1 (2004), pp. 497–515.

[79] Richardson, D. E., McLennan, M. L., Anderson, G. L., Macon, D. J., and Batista-Rodriguez, A., "Multiaxial, temperature, and time-dependent (matt) failure model", The Journal of Adhesion, Vol. 79, No. 2 (2003), pp. 157–174.

[80] Spaggiari, A., Castagnetti, D., and Dragoni, E., "Mixed-mode strength of thin adhesive films: experimental characterization through a tubular specimen with reduced edge effect", The Journal of Adhesion, Vol. 89, No. 8 (2013), pp. 660–675.

[81] Teutenberg, D., Meschut, G., Schlimmer, M., Kroll, U., and Matzenmiller, A., "Testing, material data and identification of model parameters for toughened structural adhesives", Annual Meeting of the Adhesion Society (2013).

[82] Cognard, J. Y., "Numerical analysis of edge effects in adhesively-bonded assemblies application to the determination of the adhesive behavior", Computers and Structures, Vol. 86, No. 17 (2008), pp. 1704-1717.

[83] Cognard, J. Y., Davies, P., Gineste, B., and Sohier, L., “Development of an improved adhesive test method for composite assembly design”, Composites Science and Technology, Vol. 65, No. 3 (2005), pp. 359-368.

[84] Cognard, J. Y., Davies, P., Sohier, L., and Créac’hcadec, R., “A study of the non-linear behaviour of adhesively-bonded composite assemblies”, Composite Structures, Vol. 76, No. 1 (2006), pp. 34-46.

[85] Imori, M., Tanaka, H., Kimura, M., Shibutani Y. and Liu, Y., “Simple Evaluation Method of Adhesive Failure Criterion in Multiaxial Stress States by Uniaxial Tensile Tests”, Mechanical Engineering Journal, Vol. 5, No. 1 (2018).

[86] Prager, W., “A note on discretized Michell structures”, Computer Methods in Applied Mechanics and Engineering, Vol. 3, No. 3 (1974)., pp. 349-355.

[87] Liu, Y., Matsunaka, D., Shimoda, M., and Shibutani, Y., “Interface shape design of multi-material structures for delamination strength”, Mechanical Engineering Journal, Vol. 3, No. 1 (2016), DOI:10.1299/mej.15-00360.

[88] Shimoda, M., Otani, H. and Shi, J. X., “Design optimization of composite structures composed of dissimilar materials based on a free-form optimization method”, Composite Structures, Vol. 146 (2016), pp. 114-121 DOI:10.1016/j.compstruct.2016.03.012.

[89] 西脇眞二, 泉井一浩，菊池昇, “計算力学レクチャーコーストポロジー最適化”, 丸善出版株式会社, (2013), p. 25.

[90] 飯森 理人, 渋谷 陽二, 田中 展, 劉 陽, “不変量破損則に基づく多軸応力場での接着界面形状最適化”, 日本機械学会論文集, Vol. 85, No. 870 (2019).

[91] Czerwinski, F., “Current Trends in Automotive Lightweighting Strategies and Materials”, Materials. Vol. 14, No.21:6631 (2021). https://doi.org/10.3390/ma14216631

[92] Heggemann, T., Homberg, W. and Sapli, H., “Combined Curing and Forming of Fiber Metal Laminates”, Procedia Manufacturing, Vol. 47 (2020), pp. 36-42.

[93] Heggemann, T. and Homberg, W., “Deep drawing of fiber metal laminates for automotive lightweight structures”, Composite Structures, Vol. 216 (2019), pp. 53-57.

[94] Takiguchi, M., and Yoshida F., “Deformation Characteristics and Delamination Strength of Adhesively Bonded Aluminum Alloy Sheet under Plastic Bending”, Transactions of the JSME (in Japanese), Vol. 67, No. 655(2001), pp. 226-233.

[95] Tokuda, T., Yoshida, T., Uemori T., Takiguchi M., and Yoshida F., “Shear Deformation Behavior of Adhesive Layer in Stretch-bending/unbending of Adhesively Bonded Dissimilar Sheet Metal”, Journal of The Adheshion Society of Japan, Vol. 51, No. 7 (2015), pp. 347-354 (in Japanese).

[96] Takiguchi, M., Yoshida T., Funaki, M., and Yoshida F., “Effects of Thicknesses of Adhered and adhesive layer on Plastic-bending of Adhesively Bonded Sheet Metals”, Journal of The Adheshion Society of Japan, Vol. 48, No. 12 (2012), pp. 430-435 (in Japanese).

[97] Fukui, S., Yoshida, K. and Abe, K., “Test Method for Deep Drawing of Steel Plates, Bulletin of the Japan Institute of Metals”, Vol. 1, No. 5 (1962), pp. 359-364 (in Japanese).

[98] Fukui, S., Yoshida, K. and Abe, K., “Correlation between various formability test values of thin sheets, Journal of Japan Society for Technology of Plasticity”, Vol. 2, No. 10(1961), pp. 665 (in Japanese).

[99] Erichsen cupping test, ISO standard 20482:2013.

[100] Sweden Deep-Drawing test, ISO/IEC 17025.

[101] Arab, N. and Javadimanesh, A., "Theoretical and Experimental Analysis of Deep Drawing Cylindrical Cup," Journal of Minerals and Materials Characterization and Engineering, Vol. 1, No. 6 (2013), pp. 336-342.

[102] Standard Test Method for Ball Punch Deformation of Metallic Sheet Material, ASTM E643-15.

[103] Erichsen, Bore Expanding Test Tool E acc. to Siebel and Pomp (KWI), Technical Description.

[104] Fukui, S. and Yoshida, K., “Thin plate press formability and conical cup test”, Transactions of the JSME, Bulletin of the JSME, Vol. 62, No. 489 (1959), pp. 1579-1582 (in Japanese).

[105] Green, R. J., “A plasticity theory for porous solids”, International Journal of Mechanical Sciences, Vol. 14, No. 4 (1972), pp. 215–224.

[106] da Silva, Lucas F. M., Rodrigues, T. N. S. S., Figueiredo, M. A. V., de Moura, M. F. S. F., and Chousal, J. A. G., “Effect of Adhesive Type and Thickness on the Lap Shear Strength”, The Journal of Adhesion. Vol.82, No11(2006), pp.1091-1115.

[107] Tanaka, H., Kimura, M., Iimori, M., Shibutani, Y. and Liu, Y., “Failure criteria of adhesive joints between aluminum circular pipes under multiaxial stress state”, Key Engineering Materials, Vol. 725 (2017), pp. 383-388.

[108] Azegami, H., “Solution to domain optimization problems”, Transactions of the Japan Society of Mechanical Engineers, SeriesA, Vol.60, No.574 (1994), pp.1479-1486 (in Japanese).

[109] Japanese Industrial Standards, JIS Z 2249, “Method of conical cup testing” (2010).

[110] Shibutani, Y., Kitagawa H., and Nakamura T., “Mechanism on Growth of Interfacial Roughening in Laminated Material”, Journal of the Society of Materials Science, Japan, Vol. 41, No. 466 (1992), pp. 1108-1113 (in Japanese).

[111] Shibutani, Y., Kitagawa H., and Nakamura T., “Fractal Property of Interfacial or Surface In homogeneous Deformation”, Journal of the Society of Materials Science, Japan, Vol 41, No. 470 (1992), pp. 1611-1615 (in Japanese).

[112] Azevedo, N., Farias, J., Bastos, R., Teixeira, P., Davim, J., and Alves de Sousa, R., “Lubrication Aspects during Single Point Incremental Forming for Steel and Aluminum Materials”, International Journal of Precision Engineering and Manufacturing, Vol. 16 (2015), pp. 1-7.

[113] Japanese Industrial Standards, JIS G 3101, “Rolled steels for general structure” (2015).

[114] Rowe, J., “Advanced Materials in Automotive Engineering”, Woodhead Publishing (2012).

[115] 桑原田 聡, 中西 賢二, 牟禮 雄二, 松本 泰道, “モデル材料と金属材料を用いた平面ひずみ据込み加工実験— 金属成形加工実験シミュレーション用モデル材料の開発　第２報 —”, 塑性と加工, Vol 52, No. 501 (2011), pp. 288-292.

[116] 伊達秀文, 鈴木利夫, 長谷川篤志, “温度計測法によるアルミニ

ウムの弾塑性変形機構の検討", 材料, Vol.43, No.487 (1994), pp. 399-394.

[117] 吉田 佳典, "シミュレーションのための材料試験—流動応力同定—", 軽金属, Vol. 68, No. 5 (2018), pp.266-273.

List of contributions

Related papers

- Xue, Y., Tanaka, H. and Shibutani, Y., Shape optimization of adhesives of multi-materials under multiaxial stress failure criteria, The Journal of Adhesion, Vol. 99, No. 4 (2023), pp. 558-583.
- Xue, Y. and Shibutani, Y., Evaluation of plastic formability of layered metal sheets bonded by adhesives using conical cup testing, Mechanical Engineering Journal. (accepted for publishing)

International conferences

- Xue, Y., Yamauchi, Y., Tanaka, H., Shibutani, Y. and Iimori, M., Interface shape optimization of bonded structures using adhesive failure criteria in multiaxial stress states with acrylic and epoxy adhesives, International Conference on Computational Engineering and Science for Safety and Environmental Problems 2020 (COMPSAFE2020), (2020), Kobe, Japan.
- Xue, Y., Tanaka, H. and Shibutani, Y., Shape Optimization of Adhesives of Multi-materials under Multiaxial Stress Failure Criteria, 15th World Congress on Computation Mechanics & 8th Asian Pacific Congress on Computation Mechanics (WCCM-APCOM YOKOHAMA 2022), (2022), Yokohama, Japan.

Domestic conferences

- Xue, Y., Tanaka, H. and Shibutani, Y., Co-Design of Adhesives Structures of Multi-materials with Material and Structural Factors, Mechanics of Materials Conference 2022 (M&M 2022), (2022), Hirosaki, Japan.

Acknowledgments

First and foremost, I extend my deepest gratitude to my supervisor, Professor Dr. Yoji Shibutani. Completing this doctoral dissertation would not have been possible without his meticulous guidance. Over the past six years in Japan, I have been fortunate to be a part of his laboratory, where he not only provided invaluable research instructions, constructive advice, and innovative insights but also imparted qualities and skills essential for my future as a professional researcher. His passion for research and extensive knowledge across diverse areas have set a remarkable example for me as a Ph.D. candidate and a future researcher. The knowledge, skills, and personal qualities he instilled in me are treasures I will carry with me throughout my career.

I want to express my gratefulness to Prof. Takahiro Hayashi, Prof. Nobutomo Nakamura, Department of Mechanical Engineering, and Prof. Katsuyoshi Kondoh, Joining and Welding Research Institute, for their time and efforts during the reviewing process and defense. Great appreciation for the dissertation committee for the valuable and constructive comments on this dissertation.

I also express my sincere gratitude to Professor Dr. Hiro Tanaka, the former vice professor in the laboratory, for his guidance on administrative processes and laboratory access. His suggestions greatly enhanced the efficiency and accuracy of my simulation analyses. His kindness towards all students created a welcoming atmosphere in the laboratory, providing moments of relaxation amid intense research. I am particularly thankful for his assistance in my employment activities, which holds significant meaning for my future.

My appreciation extends to Assistant Professor Dr. Lijun Liu for her assistance with the computer system and valuable comments on my research. Her guidance on tensile testing and the shared Chinese background created a comforting connection in a foreign country.

Special thanks to office Administrator Ms. Atsuko Yamaguchi for her indispensable help with administrative tasks and daily life in the research office. Her support in handling financial matters saved me considerable time, allowing me to focus on my research.

I am grateful to all the students in Shibutani Lab, including former students who shared memorable moments and kindness during our college life. Their inclusivity and willingness to share experiences made me feel at home, never isolated as a foreign student. I extend my special thanks to Dr. Masato Iimori of JSOL Corporation and Dr. Li Li of Huawei Corporation, former Ph.D. students who provided invaluable assistance and shared useful data and experiences.

A heartfelt acknowledgment goes to Mr. Iwasaki of Akoo Mechanical Engineering Co., Ltd, for his guidance in specimen manufacturing. I acknowledge the financial support from JST SPRING, Grant Number JPMJSP2138.

Lastly, immense gratitude to my family and girlfriend for their unwavering mental and financial support throughout my years in Japan. They have been my rock, providing encouragement and allowing me to focus on my studies and research. In moments of exhaustion or disappointment, their support has been the driving force that propelled me through challenges.

I extend my deep appreciation to all those mentioned above and those who may not be listed, for their indispensable support, making the completion of this doctoral dissertation possible.